First named inventor: Gi Youl Kim

Application No.: 10/791,334
Filed: March 1, 2004

Examiner: Turocy, David P.
Art Unit: 1792

Docket No.: 40004551-0025-002
Confirmation No.: 2408

Customer No.: 26263

Commissioner for Patents
P.O. Box 1450
Alexandria, VA 22313-1450

DECLARATION OF STEVEN M. GEORGE

Steven M. George declares:

1. I am a Professor in the Departments of Chemistry (1991-present) and Chemical Engineering (2001-present) at the University of Colorado at Boulder. I hold a B.S. in chemistry from Yale University (1977) and a Ph.D. in chemistry from the University of California at Berkeley (1983) and was a post-doctoral Fellow at the California Institute of Technology (1983-1984). My research focuses on fabrication, design and properties of ultrathin films and nanostructures, and in particular the use of atomic layer deposition (ALD). I am currently directing an internationally recognized research effort focusing on ALD.

2. To date, I have authored more than 250 peer-reviewed publications in the areas of surface science, thin film growth and physical chemistry. I am a Fellow of the American Vacuum Society, and the American Physical Society. I also held a fellowship from the Alfred P. Sloan Foundation. During my career I have recognized for my work through a number of awards including: the Presidential Young Investigator award (1988-1993), American Chemical Society Colorado Section Award (2004), R&D 100 Award for Particle-ALD (2004), and Inventor of the Year, University of Colorado at Boulder (2004). I was the Chairman of the first AVS Topical

Conference on Atomic Layer Deposition (ALD2001) held in Monterey, California,[1] and have been a member of the Conference Committees for all subsequent ALD meetings, including, most recently, ALD2010 in Seoul, Korea. I am a member of the Editorial Board of *Surface Review & Letters* (1998-present) and was an Associate Editor for *Chemical Reviews* (1992-1994). I was Co-Chair of the Gordon Research Conference on "Chemistry of Electronic Materials" (1997) and was Chair of the Optical Society of America Topical Meeting on "Microphysics of Surfaces: Nanoscale Processing" (1995). I was a member of the Defense Science Study Group (1989-1991).

3. I understand that the real party in interest of the subject patent application (Application No.: 10/791,334) is Aixtron, Inc. of Sunnyvale, CA, and I confirm that I have no business affiliation with Aixtron, Inc. I have been compensated for my time in reviewing the file materials of the subject patent application and the preparation of this declaration.

4. I understand that claims 1, 4-5, 8, 9, 11, 15, 17, 18, 40-46 of the subject patent application have been rejected as being anticipated by U.S. Patent Publication 20020160585 by Park et al. (hereafter "Park"), and that claims 1, 4-5, 8, 9, 11, 15, 17, 18, 40-46 have been rejected as being unpatentable over Park in view of Raija Matero et al., "Effect of water dose on the atomic layer deposition rate of oxide thin films", Thin Solid Films 368, pp 1-7 (2000) (hereafter "Matero"). I have reviewed these references in connection with my analysis of the subject patent application.

5. I understand that claim 1 of the subject patent application, as currently amended, reads as follows:

> 1. An enhanced atomic layer deposition (ALD) process for
> achieving a substantially maximum film deposition rate as

[1] Founded in 1953, AVS is a not-for-profit professional society that promotes communication between academia, government laboratories, and industry for the purpose of sharing research and development findings over a broad range of technologically relevant topics. AVS' symposia and journals provide an important forum for the dissemination of information in many areas of science and technology-enabling a critical gateway for the rapid insertion of scientific breakthroughs into manufacturing realities.

determined by film thickness per unit time, said process comprising:

exposing a wafer to a dose of a first chemically reactive precursor, said first chemically reactive precursor having a longer saturation time as compared to a second chemically reactive precursor to follow the first chemically reactive precursor, the dose of the first chemically reactive precursor being an under-saturated dose, and the first chemically reactive precursor being delivered in a manner so as to provide a substantially uniform film deposition on the wafer; and

exposing the wafer to a dose of the second chemically reactive precursor, the combination of respective doses of the first and second chemically reactive precursors selected to cause a saturated deposition rate for the second precursor being less than a maximum possible saturated deposition rate for the second chemically reactive precursor, said saturated deposition rate measured in film thickness per ALD cycle and being substantially invariant over increases in the dose of the second chemically reactive precursor,

wherein said first and second chemically reactive precursors are delivered sequentially in time.

6. In my opinion, the subject matter recited in claim 1 is not taught by Park and is not obvious to one of ordinary skill in the art in view of the combined teachings of Park and Matero. My reasoning in support of these conclusions is set forth below.

7. Claim 1 of the subject patent application recites a process which the subject patent application refers to as Transient Enhanced Atomic Layer Deposition or TE-ALD. As recited in claim 1, important aspects of TE-ALD include the facts that the dose of one of the reactants (or precursors) in the process is an under-saturated dose, and the combination of respective doses of the two reactants (or precursors) is selected to cause a saturated deposition rate for the second reactant (precursor) to be less than a maximum possible saturated deposition rate. Stated

differently, the combination of the doses is *insufficient* to produce the *maximum ALD growth* for those reactants. Maximum ALD growth does not occur because one of the ALD surface reactions is *not* saturated and *not* self-limiting. This process leads to a reduction of the total ALD cycle time over that which might have otherwise been the case, but, surprisingly, still produces films with the usual ALD benefits of high step coverage, and excellent uniformity and quality.

8. I first learned of the TE-ALD concept while attending a presentation by Tom Seidel, one of the inventors of the subject patent application, at the ALD2004 meeting in Helsinki. To my knowledge, no one previously had intentionally used exposure times for one of the ALD reactants that were shorter than the exposures required to obtain self-limiting or saturated behavior. Nor had anyone ever suggested using shorter exposures than the exposures required for self-limiting or saturated behavior for one of the ALD reactants. The prevailing thought at the time was that the ALD process *required* reactant exposure times that displayed self-limiting or saturated behavior. That shorter exposures that were insufficient to produce the maximum ALD growth could be used to obtain higher Al_2O_3 ALD film deposition rates, and that introducing *less* than sufficient saturating exposure for one of the ALD reactants could improve chemical efficiency and shorten deposition times *without* losing the ALD character of the resulting film was not obvious at that time and, in my opinion, represented a departure from conventional thinking.

9. To better appreciate the distinctions between the process recited in claim 1 of the subject patent application and the processes taught by Park and Matero, some background is helpful. A conventional ALD process is defined by a sequence of sequential surface reactions that exhibits self-limiting or saturating reactions. Evidence of self-limiting or saturated reaction conditions is provided by the *lack* of increase in thin film growth with *increasing* reactant exposure. I explained these conditions in my recent article, S.M. George, "Atomic Layer Deposition: An Overview", *Chem. Rev.*, 110, pp. 111-131 (2010), a copy of which is attached hereto as Exhibit 1. The maximum ALD growth for Al_2O_3 ALD is particularly important in the context of the present patent application because both the patent application and Park use Al_2O_3 ALD as examples.

10. Al_2O_3 ALD uses trimethylaluminum (TMA) and H_2O as reactants. The Al_2O_3 ALD system has been studied extensively in the literature and there is consensus that the maximum Al_2O_3 ALD growth rate is 1.1-1.2 Å (0.11-0.12 nm) per ALD cycle over a wide range of temperatures. *See, e.g.,* Matero, *supra.*; J.W. Elam et al., "Viscous Flow Reactor with Quartz Crystal Microbalance for Thin Film Growth by Atomic Layer Deposition", *Rev. Sci. Instrum.,* 73, pp. 2981-2987 (2002), a copy of which is attached hereto as Exhibit 2; A.W. Ott et al., "Al_2O_3 Thin Film Growth on Si(100) Using Binary Reaction Sequence Chemistry", *Thin Solid Films,* 292, pp. 135-144 (1997), a copy of which is attached hereto as Exhibit 3; and M.D. Groner et al., "Low Temperature Al_2O_3 Atomic Layer Deposition", *Chem. Mater.,* 16, pp. 639-645 (2004), a copy of which is attached hereto as Exhibit 4. This maximum growth rate per ALD cycle is obtained under self-limiting or saturated reaction conditions.

11. When one observes *larger* growth rates than 1.1-1.2 Å (0.11-0.12 nm) per ALD cycle for Al_2O_3 ALD, this is usually an indication that there is some chemical vapor deposition (CVD) occurring *in addition* to ALD. CVD occurs when a gas phase reactant from a previous reaction is still present in a reaction chamber when the subsequent reactant is exposed to the surface on which the film is being formed. In such a case, both reactants can react either in the gas phase or on the surface and produce additional film growth. Growth rates larger than the maximum Al_2O_3 ALD growth rate can also occur if one of the ALD reactions is *not* self-limiting. Non-self-limiting conditions are often associated with the instability of the surface species deposited by the surface reactions. For example, if the $AlCH_3$* surface species deposited by TMA are unstable and decompose, then they may allow additional TMA to adsorb on the surface. This decomposition process may occur at temperatures in excess of 300°C, where TMA is known to undergo thermal pyrolysis on the surface.

12. Claim 1 of the present patent application recites a "dose of the first chemically reactive precursor being an under-saturated dose", and "a saturated deposition rate for the second precursor being less than a maximum possible saturated deposition rate for the second chemically reactive precursor". In the context of Al_2O_3 ALD, this must necessarily mean a growth rate less than 1.1-1.2 Å (0.11-0.12 nm) per ALD cycle.

13. Park, on the other hand, describes a growth rate for an Al_2O_3 process that is *greater than* the maximum Al_2O_3 ALD growth rate. This is not surprising because Park's process is one that involves both CVD and ALD growth.

14. Park describes a deposition process with *no purging* between introduction of the gaseous reactants. The patent expresses the opinion that a purging step is necessary to remove residual gases that would ordinarily lead to impurities in the ALD film. There is no acknowledgement, however, of the fact that the purge is necessary to prevent film growth due to CVD from adding to the ALD growth. With no purging between the reactant gases, CVD occurs in addition to ALD because both gaseous reactants are present in the reactor at the same time. This is evidenced by the fact that in [0086] et seq., Park reports a maximum growth of 0.2 nm (2 Å) per cycle for a TMA pulse time of 0.5 sec and a H_2O pulse time of 1 sec, and a maximum growth of 0.4 nm (4 Å) per cycle for a longer TMA pulse time of 2 sec and a H_2O pulse time of 1 sec. These reported maximum growths of 0.2 and 0.4 nm are, respectively, *nearly two and four times* the accepted maximum growth rate for Al_2O_3 ALD of 0.11-0.12 nm and suggest that additional CVD must have contributed to the ALD growth process.[2] Consequently, although Park labels his no-purge process as ALD, in fact his no-purge process must be considered a *combined* ALD and CVD process.[3]

15. Claim 1 of the present patent application recites a distinctly different process from that reported by Park. For example, according to the claim, the wafer is exposed to an under-saturated dose of a so-called first precursor, which is the precursor having the longer saturation time as compared to a second precursor. In a TMA-H_2O process, H_2O is the precursor that has

---

[2] TMA pyrolysis may also be occurring in addition to CVD. TMA pyrolysis is known to occur for TMA at temperatures in excess of 300°C. Pyrolysis would lead to growth that is nearly linear with the TMA pulse time. In addition, pyrolysis would also lead to carbon impurities in the Al_2O_3 film. These carbon impurities are observed and the process described by Park requires the third step of an O_2 exposure (described as a "reducing gas") to remove the carbon impurities. In either case, with or without TMA pyrolysis, Park's is not solely an ALD process.

[3] For sake of completeness, note that another characteristic that differentiates CVD from ALD is the ability of ALD to achieve conformal step coverage. Park reports step coverage of Al_2O_3 in a hole with a diameter of ~0.4 mm and a depth of 2.3 mm. The step coverage for this hole was reported to be "more than 90%". A true ALD process should have obtained a step coverage of >98-99% for this modest aspect ratio. This lack of excellent conformality is additional evidence that the deposition process described by Park is not a true ALD process.

the longer saturation time. Accordingly, in the context of a TMA-H₂O process, claim 1 is describing an under-saturated dose of H₂O. The under-saturated dose of H₂O is clearly defined by the fact that higher H₂O exposures would produce larger ALD growth rates as illustrated in Fig. 8A of the present patent application. Figure 8A also illustrates the effect of larger TMA doses. Larger TMA doses lead to no increase in the ALD growth rate as expected for a true ALD process with no additional CVD. In contrast, Park reports exposure to different doses of TMA for an invariant water dose. Park reports a maximum growth of 0.2 nm (2 Å) per cycle for a TMA pulse time of 0.5 sec and a H₂O pulse time of 1 sec, and a maximum growth of 0.4 nm (4 Å) per cycle for a longer TMA pulse time of 2 sec and a H₂O pulse time of 1 sec. Larger TMA doses lead to an increase in the ALD growth rate. This behavior, and the underlying process, is very different than the behavior shown in Figure 8A and the process recited in claim 1 of the present application. As mentioned in paragraph 14 above, this behavior is consistent with CVD in addition to ALD. Park thus teaches what one may consider the opposite of what is being recited in claim 1. While the claim calls for exposing the wafer to an under-saturated dose of the first precursor (H₂O) having the longer saturation time and then observing an ALD growth rate that does *not increase* for longer exposure times of the second precursor (TMA), Park describes exposing a wafer to longer exposures of TMA and observes ALD growth rates that *increase* with the longer TMA exposure times.

16. Even when one considers Park in combination with Matero, significant differences from claim 1 remain. The paper by Matero is a scientific study of the effect of H₂O and TMA on the Al₂O₃ ALD growth rate. Matero shows that nearly self-limiting growth is obtained with both H₂Oand TMA exposures. The H₂O exposure is not completely self-limiting. This behavior is sometimes referred to as "soft saturation" and is often observed at lower temperatures and is related to extra H₂O or a higher density of hydroxyl groups on the surface after longer H₂O exposures. See, e.g., R.A. Wind and S.M. George, "Quartz Crystal Microbalance Studies of Al₂O₃ Atomic Layer Deposition Using Trimethylaluminum and Water at 125°C", *J. Phys. Chem. A,* 114, pp. 1281-1289 (2010), a copy of which is attached hereto as Exhibit 5.

17. Matero used short exposure times that were insufficient to produce the maximum ALD growth to characterize the Al₂O₃ growth rate versus reactant exposure time. These short times were used to define the self-limiting behavior after longer exposure times. For example,

Matero indicates that while film uniformity was substantially similar for both large and small H_2O doses, the film growth rate was "substantially higher" for large H_2O doses. See Matero, Abstract and Section 3.1, p.3. Combining such teachings with those of Park may, at best, allow one to arrive a process where, like Park, there would be exposures to different doses of TMA and, like Matero, there would also be different doses of H_2O, but is by no means clear what the resulting process would be, other than the process would not be that recited in claim 1 of the present patent application. As we have seen above, Park does not suggest a deposition rate that is substantially invariant over increases in the dose of the second chemically reactive precursor and so such teachings would still be absent from the combined teachings of these references. Furthermore, one of ordinary skill in the art may not even contemplate combining the teachings of these references because they are concerned with fundamentally different things. Park is concerned with the effect of altering the TMA dose, while Matero is discussing the effects of altering the H_2O dose and there is no discussion of using short exposure times for the purpose of maximizing the Al_2O_3 ALD film deposition rate.

I hereby declare that all statements made herein of my own knowledge are true and that all statements made on information and belief are believed to be true, and further that these statements were made with knowledge that willful false statements and the like so made are punishable by fine or imprisonment, or both (18 U.S.C. 1001) and may jeopardize the validity of the subject patent application or any patent issuing thereon.

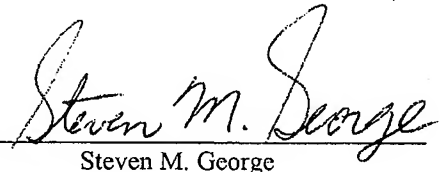Executed on _April 1_, 2010, at _Boulder, CO_ by _Steven M. George_
Steven M. George

EXHIBIT 1

Atomic Layer Deposition: An Overview

Steven M. George*

Department of Chemistry and Biochemistry and Department of Chemical and Biological Engineering, University of Colorado, Boulder, Colorado 80309

Contents

1. Introduction

Atomic layer deposition (ALD) has emerged as an important technique for depositing thin films for a variety of applications. Semiconductor processing has been one of the main motivations for the recent development of ALD. The *International Technology Roadmap for Semiconductors* (ITRS) has included ALD for high dielectric constant gate oxides in the MOSFET structure and for copper diffusion barriers in backend interconnects.[1] In addition, ALD has met

Steven M. George is Professor in the Department of Chemistry and Biochemistry and Department of Chemical and Biological Engineering at the University of Colorado at Boulder. Dr. George received his B.S. in Chemistry from Yale University (1977) and his Ph.D. in Chemistry from the University of California at Berkeley (1983). Prior to his appointments at the University of Colorado at Boulder, Dr. George was a Bantrell Postdoctoral Fellow at Caltech (1983−4) and an Assistant Professor in the Department of Chemistry at Stanford University (1984−1991). Dr. George is a Fellow of the American Vacuum Society (2000) and a Fellow of the American Physical Society (1997). He has also received the American Chemical Society Colorado Section Award (2004), R&D 100 Award for Particle-ALD (2004), NSF Presidential Young Investigator Award (1988−1993), and an Alfred P. Sloan Foundation Fellowship (1988). Dr. George's research interests are in the areas of surface chemistry, thin film growth, and nanostructure engineering. He is currently directing a research effort focusing on atomic layer deposition (ALD) and molecular layer deposition (MLD). This research is examining new surface chemistries for ALD and MLD growth, measuring thin film growth rates, and characterizing the properties of thin films. Dr. George served as Chair of the first American Vacuum Society (AVS) Topical Conference on Atomic Layer Deposition (ALD2001) held in Monterey, California. He also teaches a one-day short course on ALD for the AVS. Dr. George is a cofounder of ALD NanoSolutions, Inc., a startup company that is working to commercialize ALD technology.

challenging requirements in other areas including the deposition of high quality dielectrics to fabricate trench capacitors for DRAM.[2]

Miniaturization in the semiconductor industry has led to the requirement for atomic level control of thin film deposition. Miniaturization has produced very high aspect structures that need to be coated conformally. No other thin film technique can approach the conformality achieved by ALD on high aspect structures. The necessity for continuous and pinhole-free films in semiconductor devices has driven the advancement of ALD. Other applications with similar demanding requirements outside of the semiconductor industry are low electron leakage dielectrics for magnetic read/write heads[3] and diffusion barrier coatings with low gas permeability.[4]

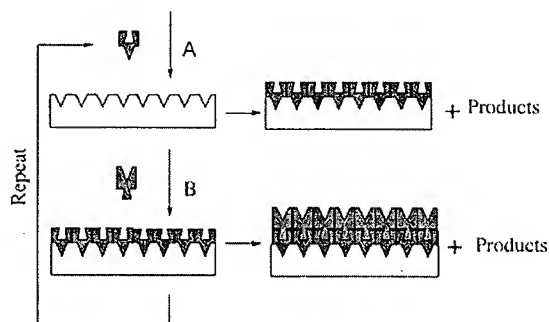* E-mail address: Steven.George@Colorado.Edu.

Figure 1. Schematic representation of ALD using self-limiting surface chemistry and an AB binary reaction sequence. (Reprinted with permission from ref 5. Copyright 1996 American Chemical Society.)

ALD is able to meet the needs for atomic layer control and conformal deposition using sequential, self-limiting surface reactions. A schematic showing the sequential, self-limiting surface reactions during ALD is displayed in Figure 1.[5] Most ALD processes are based on binary reaction sequences where two surface reactions occur and deposit a binary compound film. Because there are only a finite number of surface sites, the reactions can only deposit a finite number of surface species. If each of the two surface reactions is self-limiting, then the two reactions may proceed in a sequential fashion to deposit a thin film with atomic level control.

The advantages of ALD are precise thickness control at the Ångstrom or monolayer level. The self-limiting aspect of ALD leads to excellent step coverage and conformal deposition on high aspect ratio structures. Some surface areas will react before other surface areas because of different precursor gas fluxes. However, the precursors will adsorb and subsequently desorb from the surface areas where the reaction has reached completion. The precursors will then proceed to react with other unreacted surface areas and produce a very conformal deposition.

The self-limiting nature of the surface reactions also produces a nonstatistical deposition because the randomness of the precursor flux is removed as an important factor. As a result, ALD films remain extremely smooth and conformal to the original substrate because the reactions are driven to completion during every reaction cycle.[6] Because no surface sites are left behind during film growth, the films tend to be very continuous and pinhole-free. This factor is extremely important for the deposition of excellent dielectric films.[7]

ALD processing is also extendible to very large substrates and to parallel processing of multiple substrates. The ALD precursors are gas phase molecules, and they fill all space independent of substrate geometry and do not require line-of-sight to the substrate. ALD is only limited by the size of the reaction chamber. The ALD process is also dominated by surface reactions. Because the surface reactions are performed sequentially, the two gas phase reactants are not in contact in the gas phase. This separation of the two reactions limits possible gas phase reactions that can form particles that could deposit on the surface to produce granular films.

The use of the term "ALD" dates back approximately to 2000. Prior to 2000, the term atomic layer epitaxy (ALE) was in common use.[8-13] Other terms have been used to describe ALD, including binary reaction sequence chemistry[14] and molecular layer epitaxy.[15] The transition from ALE

to ALD occurred as a result of the fact that most films grown using sequential, self-limiting surface reactions were not epitaxial to their underlying substrates. Moreover, amorphous films were most preferred for dielectric and diffusion barrier applications. Consequently, the use of ALD grew in preference and now dominates with the practitioners in the field.
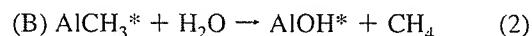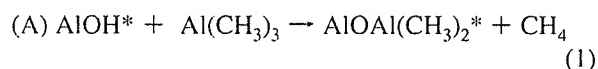
The history of ALE and ALD dates back to the 1970s in Finland. The original pioneer of ALE was Tuomo Suntola, who demonstrated some of the first ALE processes as early as August/September 1974.[16] The first ALE system developed was ZnS.[16] The first ALE patent emerged in 1977.[17] The first literature paper on ALE appeared in 1980 in *Thin Solid Films*.[18] The first application of ALE was electroluminescent displays. The first public display of an ALE device was an electroluminescent display that operated in the Helsinki airport from 1983 to 1998. The first commercial ALE reactor was the F-120 sold by Microchemistry in 1988. The first of a series of ALE meetings was held in 1990 and continued through 1996. The first of a series of yearly ALD meetings was held in 2001 and has continued through the present date.

Many earlier reviews have addressed the basics of ALE or ALD.[5,8,11,12,19-21] Many previous reviews have considered the application of ALE or ALD to microelectronics and nanotechnology.[19,22-27] The intent of this present review is not to duplicate these previous reviews. Instead, this review is focused on an overview of key concepts and new directions in ALD. The semiconductor roadmap is coming to an end in a few years because of the limits of the current electronic materials. For continued progress, the future for electronic materials will embrace as yet undefined paradigms. ALD will almost certainly be part of the new paradigms because of its ability to control deposition on the atomic scale and to deposit conformally on very high aspect ratio structures.

2. Al₂O₃ ALD as a Model ALD System

The ALD of Al_2O_3 has developed as a model ALD system. An earlier extensive review by Puurunen has previously discussed the details of Al_2O_3 ALD.[20] Consequently, this section will only mention the highlights of Al_2O_3 ALD. Al_2O_3 ALD is usually performed using trimethylaluminum (TMA) and H_2O. The first reports of Al_2O_3 ALD using TMA and H_2O date back to the late 1980s and early 1990s.[28,29] More recent work in the semiconductor industry is using TMA and ozone for Al_2O_3 ALD.[30,31] This review will concentrate on Al_2O_3 ALD using TMA and H_2O.

The surface chemistry during Al_2O_3 ALD can be described as[5,14,32]

$$\text{(A) AlOH* + Al(CH}_3)_3 \rightarrow \text{AlOAl(CH}_3)_2\text{* + CH}_4 \qquad (1)$$

$$\text{(B) AlCH}_3\text{* + H}_2\text{O} \rightarrow \text{AlOH* + CH}_4 \qquad (2)$$

where the asterisks denote the surface species. The Al_2O_3 ALD growth occurs during alternating exposures to TMA and H_2O. Al_2O_3 ALD is a model system because the surface reactions are very efficient and self-limiting. The main driver for the efficient reactions is the formation of a very strong $Al-O$ bond. The overall reaction for Al_2O_3 ALD is
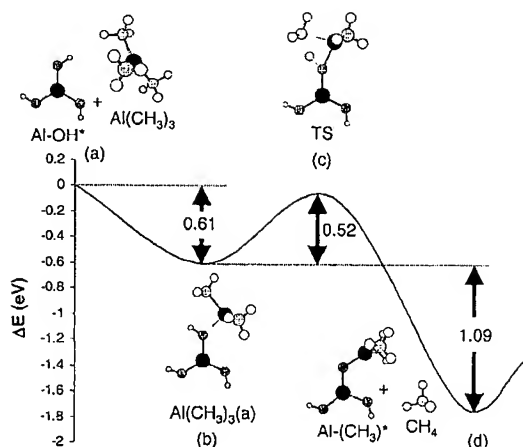
$$2Al(CH_3)_3 + 3H_2O \rightarrow Al_2O_3 + 3CH_4$$
$$\Delta H = -376 \text{ kcal} \qquad (3)$$
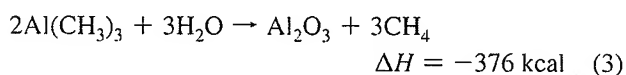
Figure 2. Reaction path and predicted energetics for reactions of $Al(CH_3)_3$ on the Al—OH* surface site calculated using the $Al(OAl(OH)_2)_2$—OH cluster. The structures are shown using the $Al(OH_2)$—OH cluster for clarity. (Reprinted with permission from ref 34. Copyright 2002 American Institute of Physics.)

This reaction has an extremely high reaction enthalpy.[33] This is one of the highest reaction enthalpies encountered for any ALD reaction.

The potential energy surfaces during Al_2O_3 ALD have been modeled using density functional theory (DFT).[34] These calculations show that $Al(CH_3)_3$ exists in a deep precursor well complexed to AlOH* species prior to its surface reaction, as shown in Figure 2.[34] Likewise, the calculations show that H_2O is also in a deep precursor well complexed to $AlCH_3$* species prior to its surface reaction. These complexes result from strong Lewis acid—base interactions on the surface. Although these precursor wells have not been experimentally observed, they may be fairly general for various classes of ALD reactions.

The surface chemistry of Al_2O_3 ALD has been confirmed by in situ FTIR studies.[32,35,36] The FTIR difference spectra clearly show the loss of AlOH* species and concurrent gain of $AlCH_3$* species during the TMA reaction. Likewise, the loss of $AlCH_3$* species and the concurrent gain of AlOH* species is observed during the H_2O reaction. The gas phase reaction products during Al_2O_3 ALD have also been identified using quadrupole mass spectrometry studies.[37,38] Using $Al(CH_3)_3$ and D_2O as the reactants, CH_3D was observed as the main reaction product, as expected from the surface chemistry for Al_2O_3 ALD.[37]

By repeating the surface reactions, Al_2O_3 growth is extremely linear with the number of AB cycles.[14,39] Various techniques, such as spectroscopic ellipsometry and quartz crystal microbalance (QCM) measurements, have characterized the growth per cycle during Al_2O_3 ALD. Typical measured Al_2O_3 ALD growth rates are 1.1—1.2 Å per AB cycle.[14,39] The resulting Al_2O_3 ALD films are smooth and extremely conformal to the underlying substrate. Studies on nanoparticles show excellent conformality of Al_2O_3 ALD films.[35,40,41] Investigations on high aspect ratio trench substrates also reveal superb conformality, as illustrated by the cross-sectional scanning electron microscopy (SEM) image in Figure 3.[42]

One of the hallmarks of ALD is self-limiting surface chemistry. The self-limiting surface reactions during Al_2O_3 ALD have been observed by in situ FTIR[32,35] and QCM[39] investigations as well as by spectroscopic ellipsometry studies.[14] The reactant exposures required for the surface

Figure 3. Cross-sectional SEM image of an Al_2O_3 ALD film with a thickness of 300 nm on a Si wafer with a trench structure. (Reprinted with permission from ref 42. Copyright 1999 John Wiley & Sons.)

reactions to reach completion reveal that the reactive sticking coefficients during Al_2O_3 ALD are much less than unity. Based on required exposure times, the reactive sticking coefficients are in the range of $\sim 10^{-3}$—10^{-4} during Al_2O_3 ALD.[14]

The growth per one ALD cycle is also much smaller than one Al_2O_3 "monolayer". The growth rates of 1.1—1.2 Å per AB cycle can be compared with the thickness of one Al_2O_3 "monolayer". This monolayer thickness is estimated using the density of 3.0 g/cm³ for Al_2O_3 ALD films grown at 177 °C.[43] Based on this density, the number density of "Al_2O_3" units is $\rho = 1.77 \times 10^{22}$ Al_2O_3 units/cm³. The number of Al_2O_3 units per square centimeter is equal to $\rho^{2/3} = 6.8 \times 10^{14}$ cm⁻². Likewise, the monolayer thickness is equal to $\rho^{-1/3} = 3.8$ Å. The growth per AB cycle of 1.1—1.2 Å per AB cycle is much less than this estimate of the monolayer thickness.

The disagreement between growth per AB cycle and the monolayer thickness is not surprising because ALD growth is dependent on surface species and surface chemistry. This surface chemistry is not required to always yield a "monolayer" of growth during every AB cycle. The correlation between ALD growth and surface chemistry is clearly illustrated by the temperature-dependence of Al_2O_3 ALD growth per AB cycle. The growth per AB cycle decreases progressively with temperature between 177 and 300 °C. This decrease results from the progressive loss of AlOH* and $AlCH_3$* surface species at higher temperatures.[14,32]

The continuous and pinhole-free nature of Al_2O_3 ALD films is revealed by their superb electrical properties. Current—voltage curves for various Al_2O_3 ALD film thicknesses on n-Si(100) reveal electrical behavior that is very similar to that of thermal SiO_2 films.[7] The Al_2O_3 ALD films have a dielectric constant of ~ 7 and display very low electron leakage.[7] Increases in the current density versus applied potential occur as a result of Fowler—Nordheim tunneling. This characteristic is consistent with the absence of any defects or pinholes in the Al_2O_3 ALD film. These excellent properties have enabled Al_2O_3 ALD films to serve as gate oxides and to passivate semiconductor surfaces.[44-46]
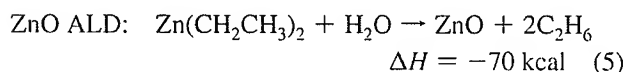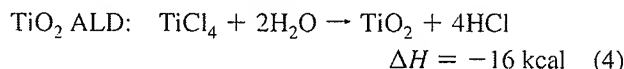
3. Thermal and Plasma or Radical-Enhanced ALD

3.1. Thermal ALD

ALD is closely related to chemical vapor deposition (CVD) based on binary reactions such as A + B → Product.

For CVD using binary reactions, the A and B reactants are present at the same time and form the product film continuously on the substrate. In ALD, the substrate is exposed to the A and B reactants individually and the product film is formed in a stepwise and very digital fashion. A generic recipe for ALD is to find a CVD process based on a binary reaction and then to apply the A and B reactants separately and sequentially in an ABAB... binary reaction sequence.

There are many examples of ALD resulting from binary reaction CVD processes. Examples for TiO_2 and ZnO are based on the following binary CVD reactions and their corresponding reaction enthalpies:[33]

$$TiO_2 \; ALD: \quad TiCl_4 + 2H_2O \rightarrow TiO_2 + 4HCl$$
$$\Delta H = -16 \; kcal \quad (4)$$

$$ZnO \; ALD: \quad Zn(CH_2CH_3)_2 + H_2O \rightarrow ZnO + 2C_2H_6$$
$$\Delta H = -70 \; kcal \quad (5)$$

These ALD systems yield a growth per AB cycle of ~0.4 Å from 150 to 600 °C for TiO_2 ALD[47] and 2.2–2.5 Å from 100 to 160 °C for ZnO ALD.[48,49] These ALD chemistries have negative heats of reaction and are robust ALD reactions. These reactions occur spontaneously at various temperatures and will be referred to as thermal because they can be performed without the aid of plasma or radical assistance.

A survey of developed ALD processes reveals that most thermal ALD systems are binary compounds based on binary reactant CVD.[20,21] The most common thermal ALD systems are binary metal oxides such as Al_2O_3, TiO_2, ZnO, ZrO_2, HfO_2, and Ta_2O_5. Other common thermal ALD systems are binary metal nitrides such as TiN, TaN, and W_2N. Thermal ALD systems also exist for sulfides such as ZnS and CdS and phosphides such as GaP and InP.

3.2. Plasma or Radical-Enhanced ALD

There is also a need for single-element ALD materials, such as metals and semiconductors, that can be deposited using a binary reaction sequence. Except for some notable exceptions discussed in section 5, the single-element films of metals and semiconductors are very difficult to deposit using thermal ALD processes. Fortunately, these single-elements can be deposited using plasma or radical-enhanced ALD.[22] The radicals or other energetic species in the plasma help to induce reactions that are not possible using just thermal energy. Plasma sources can be used to generate hydrogen radicals that reduce the metal or semiconductor precursors. Hydrogen radicals can also be produced using a hot tungsten filament. A scheme for metal ALD using metal reactants and hydrogen radicals is shown in Figure 4.

Hydrogen radical-enhanced ALD was first demonstrated for Ti ALD[50] using a H_2 plasma. Ta ALD is another ALD system that has been studied extensively using hydrogen radicals from H_2 plasmas.[51] The reactants for Ta ALD are $TaCl_5$ and hydrogen radicals.[51] The surface chemistry for Ta ALD can be expressed as

$$(A) \; Ta^* + TaCl_5 \rightarrow TaTaCl_5^* \quad (6)$$

$$(B) \; TaCl_5^* + 5H \cdot \rightarrow Ta^* + 5HCl \quad (7)$$
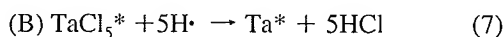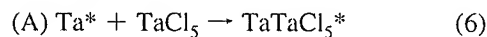
$TaCl_5$ is first exposed to the surface. Subsequently, the hydrogen radicals reduce the Ta atoms and remove the chlorine from the surface. Although the growth per cycle
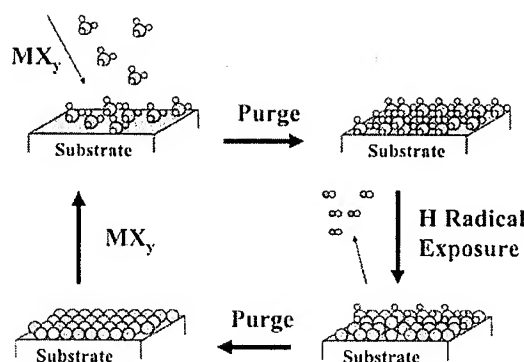

Figure 4. Schematic diagram of hydrogen radical-enhanced ALD using a metal reactant and hydrogen radicals.

during Ta ALD is only 0.08 Å per AB cycle, the Ta ALD films have excellent film resistivities and show good Cu barrier properties.[51] The small growth per cycle is attributed to steric hindrance caused by the large $TaCl_5$ admolecule on the surface. XRD also indicates that the Ta ALD film is β-Ta and has very small nanograins.[51]

The limitations of hydrogen radical-enhanced ALD were also demonstrated by studies using trenched samples.[51] The Ta ALD films were not conformal in trenches with a high aspect ratio of 40:1. When the Ta ALD film had a thickness of 28 nm at the top of the trench, the thickness was only 11 nm at the bottom of the trench. The lower Ta ALD growth at the bottom of the trench is attributed to hydrogen radical recombination on the walls of the trench that attenuates the hydrogen radical flux.[52] Radical recombination will limit the general utility of plasma ALD in high aspect ratio structures.

The ALD of single-element semiconductors such as Si and Ge can also be deposited using hydrogen radical-enhanced ALD. The surface chemistry for Si ALD is based on the desorption kinetics for H_2, HCl, and $SiCl_2$ from silicon surfaces. H_2 desorbs at 535 °C,[53,54] HCl desorbs at 575 °C,[53] and $SiCl_2$ desorbs at 725 °C[53,55] during temperature programmed desorption (TPD) experiments from silicon surfaces. H_2 desorbs at a lower temperature than HCl from silicon surfaces. $SiCl_2$ desorbs at a higher temperature than HCl from silicon surfaces. Consequently, silicon can be deposited using a chlorine-containing silicon precursor such as SiH_2Cl_2.

The surface chemistry for Si ALD using SiH_2Cl_2 and hydrogen radicals can be written as

$$(A) \; Si^* + SiH_2Cl_2 \rightarrow SiSiCl_2^* + H_2 \quad (8)$$

$$(B) \; SiCl_2^* + 2H \rightarrow Si^* + 2HCl \quad (9)$$
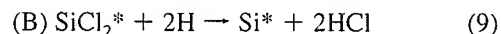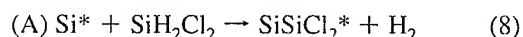
At the appropriate temperature, H_2 and HCl will desorb upon SiH_2Cl_2 adsorption but $SiCl_2$ will not desorb from the silicon surface. The build up of chlorine on the silicon surface will produce a self-limiting adsorption of SiH_2Cl_2. The surface chlorine can then be removed by exposing the surface to hydrogen radicals. The hydrogen radicals add hydrogen atoms to the silicon surface that recombine with surface chlorine to desorb as HCl or with other surface hydrogen atoms to desorb as H_2. The hydrogen radical flux will eventually remove all the surface chlorine species.

Studies of Si ALD using SiH_2Cl_2 and H radicals have demonstrated the self-limiting nature of Si ALD growth versus both SiH_2Cl_2 and hydrogen radical exposures.[56,57] A Si ALD growth per cycle of ~1.6 Å was observed between

550 and 610 °C. At higher temperatures, the Si ALD growth per cycle increased as a result of Si CVD. At lower temperatures, the Si ALD growth per cycle decreased as a result of incomplete surface reactions. A similar strategy was also applied for Ge ALD using GeH_2Cl_2 and hydrogen radicals.[58,59]

Si and Ge ALD were both demonstrated on silicon and germanium surfaces. However, a difficulty with Si and Ge ALD is their nucleation on other types of surfaces. Si and Ge are both very reactive and easily react with oxygen from oxide substrates to form SiO_2 or metals from metallic substrates to form silicides. Consequently, the nucleation of Si and Ge ALD is very difficult. The nucleation problems have limited the surface chemistry for Si and Ge ALD to only silicon and germanium surfaces.

In addition to single-element materials, plasma-enhanced ALD can deposit compound materials. One important advantage is that plasma-enhanced ALD can deposit films at much lower temperatures than thermal ALD. For example, plasma-enhanced Al_2O_3 ALD can be performed using TMA and O_2 plasma at temperatures as low as room temperature.[60] The low temperature deposition is useful for coating thermally fragile substrates such as polymers.[61] The plasma-enhanced Al_2O_3 ALD films also have improved electrical properties compared with thermal Al_2O_3 ALD[62] and lead to excellent passivation of silicon substrates.[63]

Plasma-enhanced ALD has also been useful to deposit metal nitrides, such as TiN and TaN, which generally cannot be grown with high quality using organometallic precursors.[64] TaN ALD has been achieved using organometallic tantalum precursors such as terbutylimidotris(diethylamido)tantalum (TBTDET) and hydrogen radicals.[60,65,66] The plasma-enhanced process can form TaN films that have much lower electrical resistivity and higher density than TaN ALD films grown using thermal TaN ALD with TBTDAT and NH_3.[67,68]

Oxygen radical-enhanced ALD has been employed to grow metal oxides using metal β-diketonate precursors. Metal oxides, such as Y_2O_3, have been grown at low temperatures with minimal carbon contamination.[69] Remote O_2 plasmas have also been utilized for plasma enhanced Pt ALD with (methylcyclopentadienyl)trimethylplatinum as the metal precursor.[70] In addition, plasma-enhanced Ru ALD has been accomplished using bis(ethylcyclopentadienyl)ruthenium and NH_3 plasma.[71] These plasma-enhanced Ru ALD films have potential as adhesion layers for copper interconnects.[65]

4. Reactors for ALD

There are different types of ALD reactors. Many ALD reactor designs were discussed in the original patents by T. Suntola in 1977[17] and 1983.[72] Various ALD reactors and design principles were also described in early reviews of ALE by T. Suntola.[12,13,73] One of the early ALD reactors had a revolving substrate holder that rotated the substrate in and out of the A and B reactant flow streams. Another design was based on gas flow through hot wall CVD tube reactors. Other ALD reactors flowed the reactant in an inert carrier gas through a small channel between the reactor wall and substrate. This design was known as the "traveling-wave" reactor and is represented by the F-120 reactor by Microchemistry Ltd.[11]

To organize the various ALD reactor designs, there are two limiting types of ALD reactors that can be defined by the pumping and use of a carrier gas. In one limit are ALD reactors where the reactants are exposed without using a

carrier gas and sometimes with throttled pumping.[14,15,74] After the exposures, the reactants are removed by opening up completely to the pump and evacuating the reactor. Because of the long residence times in the reactor, these exposures can utilize reactants very efficiently. However, the evacuation times for these ALD reactors can be slow in the absence of a purge gas. At low pressures in molecular flow, the random walk of molecules colliding only with the reactor walls leads to long pumping times.

In another limit are ALD reactors where the reactants are exposed with a carrier gas flowing through the reactor.[12,39,75] The carrier gas is in viscous flow and flows continuously to the pump. If the reactants have sufficient vapor pressure, the reactants can be dosed into the carrier gas stream. Alternatively, the carrier gas can flow over the headspace of a solid or liquid reactant or through the liquid reactant if the reactant has a lower vapor pressure. The carrier gas entrains the reactants and products and defines a short residence time in the reactor. The advantage of the viscous flow reactors is their much shorter ALD cycle times relative to the ALD reactors employing no carrier gas during reactant exposure and purging.

Most ALD reactors operate with an inert carrier gas in viscous flow. The optimum pressure for viscous flow reactors is around ~1 Torr. This optimum pressure is a trade-off between gas interdiffusion and entrainment. For example, the interdiffusion coefficient of O_2 in N_2 is $D_{12} = 132$ cm²/s at 1 Torr and 0 °C. This interdiffusion coefficient is determined knowing that $D_{12} = 0.174$ cm²/s at 1 atm and 0 °C[76] and that gas diffusion is inversely proportional to pressure, $D \sim 1/P$.[76] The mean squared displacement, x^2, resulting from gas diffusion is $x^2 = 6Dt$, where t is time. Therefore, the mean displacement for O_2 in N_2 gas at 1 Torr and 0 °C is $x = 28$ cm in 1 s. This sizable mean displacement indicates that diffusion of reactants in N_2 gas at 1 Torr is sufficient for removal of reactants and products from stagnant gas in the reactor in a reasonable time.

The pressure of 1 Torr is also high enough for the N_2 to be an effective carrier gas. The mean free path, λ, between N_2 molecules at room temperature is $\lambda \sim 5 \times 10^{-3}$ cm/P, where P is in Torr.[77] This approximation reveals that the mean free path of N_2 at 1 Torr is $\lambda \sim 50$ μm. This small mean free path indicates that N_2 gas is in viscous flow at 1 Torr and will effectively entrain reactants. Mean displacements may be too small for effective purging from stagnant gas at pressures higher than 1 Torr. Entrainment will be less effective at pressures lower than 1 Torr when the gas mean free paths are longer. Inert carrier gas pressures around ~1 Torr are a compromise between these two factors.

One ALD reactor that optimizes the residence times during reaction and purging is known as synchronously modulated flow and draw (SMFD).[78] The SMFD design injects the inert flowing gas at the reactor inlet during the purge steps and at the reactor outlet during the reactant exposures. The synchronized modulation of the inert flowing gas between the reactor inlet and the reactor outlet enables high-speed gas flow switching. A schematic illustrating the dose and purge modes during SMFD is shown in Figure 5.[79]

The reactant has a long residence time during dosing and only experiences a slow "draw" from the inert flowing gas entering at the reactor outlet. The reactant can be utilized very efficiently during the dose mode. In contrast, the reactant has a short residence time during the purge mode because inert carrier gas enters at the reactor inlet and flows through
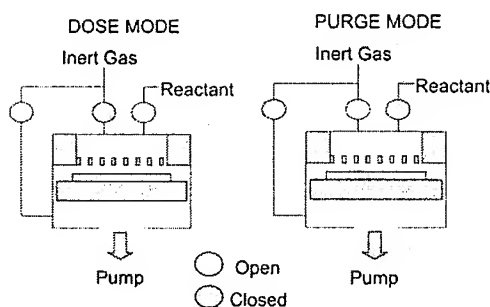
Figure 5. Illustration of purge and dose modes during synchronous modulation of flow and draw. (Adapted from information provided by Sundew Technologies, LLC.)

the reactor. The SMFD design leads to short ALD cycle times of <1 s for ALD systems such as Al_2O_3 ALD.[79]

Single-wafer ALD reactors for semiconductor processing may have different configurations for the gas flow. The "cross-flow" reactors have parallel gas flows across the wafer surface. The "showerhead" reactors bring the gas into the reactor perpendicular to the wafer surface through a distributor plate. The gas then flows radially across the wafer surface. Other distinctions between ALD reactors are between hot and cold wall reactors. In "hot wall" reactors, the walls, gas, and substrates in the reactor are all heated to the temperature of the walls. In "cold wall" reactors, only the substrate is heated and the walls remain at room temperature or are only warmed slightly.

Other ALD reactors can deposit on many samples simultaneously. These reactors are known as "batch" reactors. They can coat multiple samples at the same time and can dramatically shorten the required time to coat one sample. The batch reactors can improve the cost and time effectiveness for commercial ALD processes. Reactant and purging time constants are longer in batch reactors because of larger reactor volumes and lower gas conductance between multiple samples. However, the multiplex advantage can offset the longer time constants.

Plasma reactant sources have also become increasingly important for ALD processing. Inductively coupled plasma (ICP) is a common plasma source during plasma ALD. Plasmas usually operate at pressures of ~100–500 mTorr.
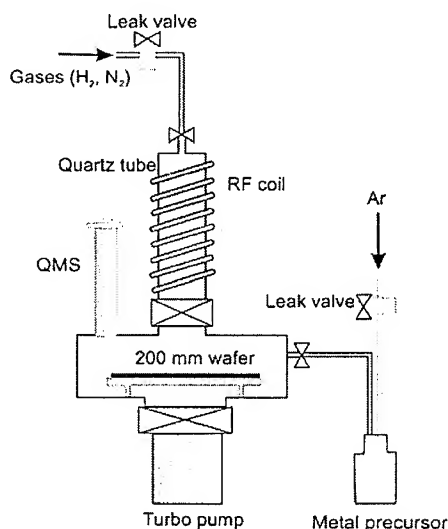

Figure 6. Schematic diagram of a plasma-enhanced ALD system used for Ta ALD and Ti ALD. (Reprinted with permission from ref 51. Copyright 2002 American Institute of Physics.)

Plasma-enhanced ALD is not performed with an inert carrier gas during the plasma reaction cycle. However, the plasma reaction cycle may alternate with a conventional reactant ALD cycle using an inert carrier gas. The plasma ALD reactor used for Ta ALD[51] and Ti ALD[50] is shown in Figure 6. A commercial plasma ALD reactor for 200 mm wafers was also recently described for TiN and HfO_2 ALD.[80]

## 5. Metal ALD Using Thermal Chemistry

Metal ALD can also be accomplished using thermal chemistry without the aid of plasma or radical assistance.[22] Thermal chemistry for metal ALD is very important because thermal chemistry does not have the limitations caused by surface recombination that restrict radical-enhanced ALD in high aspect ratio structures. Metal ALD based on thermal chemistry has been demonstrated for a variety of metals. There are three main types of metal ALD using thermal chemistry that have been successful. These ALD surface chemistries are based on fluorosilane elimination, combustion chemistry, or hydrogen reduction.

5.1. Fluorosilane Elimination Chemistry

Fluorosilane elimination reactions result from the reaction of metal fluorides and silicon precursors such as SiH_4 and Si_2H_6. These reactions were first demonstrated for W ALD.[81] The basis for these reactions is the formation of a very stable Si–F bond that leads to a very exothermic reaction. The overall chemistry for W ALD using WF_6 and Si_2H_6 is[33]
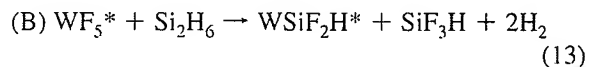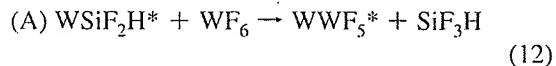
$$WF_6 + Si_2H_6 \rightarrow W + SiF_3H + 2H_2$$
$$\Delta H = -181 \text{ kcal} \quad (10)$$
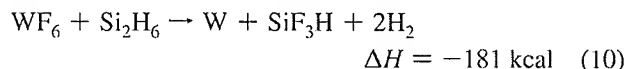
Other metals can also be deposited using fluorosilane elimination reactions such as Mo ALD according to[33]

$$MoF_6 + Si_2H_6 \rightarrow Mo + SiF_3H + 2H_2$$
$$\Delta H = -220 \text{ kcal} \quad (11)$$
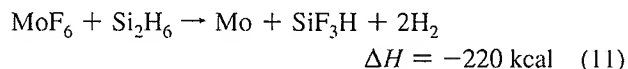
The high reaction enthalpies of $\Delta H = -181$ kcal for W ALD and $\Delta H = -220$ kcal for Mo ALD are comparable to or higher than the reaction enthalpy of $\Delta H = -376$ kcal for Al_2O_3 ALD on a per mole of metal basis.

The surface chemistry during W ALD using WF_6 and Si_2H_6 as the reactants can be simply expressed as[81,82]

$$\text{(A)} \quad WSiF_2H^* + WF_6 \rightarrow WWF_5^* + SiF_3H \quad (12)$$

$$\text{(B)} \quad WF_5^* + Si_2H_6 \rightarrow WSiF_2H^* + SiF_3H + 2H_2 \quad (13)$$

This surface chemistry is supported by in situ FTIR studies of the absorbance from Si–H and W–F stretching vibrations on surface species during the WF_6 and Si_2H_6 exposures.[81] The absorbance from Si–H stretching vibrations decreases and the absorbance from W–F stretching vibrations increases concurrently during WF_6 exposures. The absorbance from W–F stretching vibrations decreases and the absorbance from Si–H stretching vibrations also increases concurrently during Si_2H_6 exposures.

The surface chemistry for W ALD leads to the linear deposition of W ALD films versus AB cycles, as shown in Figure 7.[83] QCM studies have measured W ALD growth per cycle, which varies from 4 to 7 Å versus surface temperatures
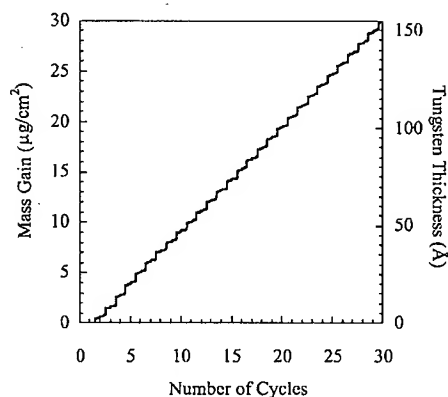
Figure 7. Mass gain monitored by quartz crystal microbalance for 30 cycles during W ALD using WF_6 and Si_2H_6 as the reactants. The corresponding tungsten thickness has been calculated assuming a density of 19.3 g/cm^3. (Reprinted with permission from ref 83. Copyright 2005 Elsevier.)

from 177 to 325 °C and Si_2H_6 reactant exposures from ~10^4 to 10^6 Langmuirs.[83] The dependence on surface temperature and Si_2H_6 exposure is believed to be caused by Si_2H_6 insertion into Si—H bonds.[83,84] This bond insertion mechanism leads to a Si CVD contribution to the W ALD growth. The Si CVD contributions are more pronounced at higher temperatures and larger Si_2H_6 exposures.[84] W ALD is used during semiconductor fabrication as a nucleation layer for tungsten plug fill processes.[85]
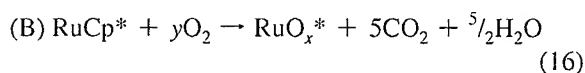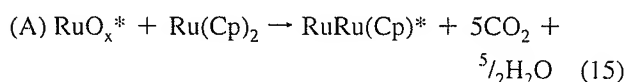
5.2. Combustion Chemistry

Some catalytic metals can be deposited using combustion chemistry. In this process, the organic ligands of the organometallic metal precursors react with oxygen to produce CO_2 and H_2O as combustion products. Ru and Pt were the first metal ALD systems that were deposited using combustion chemistry.[86,87] The Ru precursor was $Ru(C_5H_5)_2$ (bis(cyclopentadienyl)ruthenium), and the Pt precursor was $(CH_3C_5H_4)Pt(CH_3)_3$ ((methylcyclopentadienyl)trimethylplatinum). The oxygen precursor was O_2. Ru ALD was accomplished at temperatures between 275 and 400 °C, and the growth per cycle was 0.4—0.5 Å at 350—400 °C.[86] Pt ALD was initially reported at 300 °C. and the growth per cycle was also 0.4—0.5 Å.[87]

The mechanism of Ru ALD and Pt ALD was explored using quadrupole mass spectrometry (QMS) and QCM studies.[88] The QMS investigations observed H_2O and CO_2 during both the organometallic precursor and O_2 exposures. These classic combustion products suggest an overall reaction for Ru ALD of

$$Ru(Cp)_2 + {}^{25}\!/_2 O_2 \rightarrow Ru + 10CO_2 + 5H_2O$$

$$(14)$$
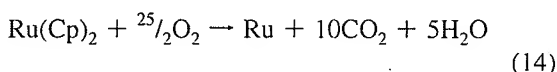
The individual surface chemical reactions for Ru ALD are proposed to be

$$(A)\ RuO_x{}^* + Ru(Cp)_2 \rightarrow RuRu(Cp)^* + 5CO_2 +$$
$$ {}^5\!/_2 H_2O \quad (15)$$

$$(B)\ RuCp^* + yO_2 \rightarrow RuO_x{}^* + 5CO_2 + {}^5\!/_2 H_2O$$
$$(16)$$

The QCM studies are especially interesting because they reveal large mass gains during the O_2 exposures, as displayed
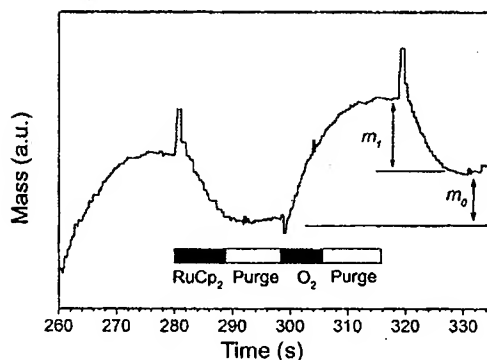

Figure 8. Quartz crystal microbalance data measured during the reaction cycles for Ru ALD using $RuCp_2$ and oxygen as the reactants. (Reprinted with permission from ref 88. Copyright 2003 The Electrochemical Society.)

in Figure 8.[88] The oxidation of surface organic species initially produces a mass loss. A subsequent mass gain is produced when O_2 deposits oxygen to the Ru surface and the subsurface region. This surface oxygen is then available to oxidize some of the incoming organic ligands on the organometallic precursor.

This combustion chemistry is believed to occur most easily for group VIII metals that are known to be heterogeneous catalysts. The ALD of other catalytic metals such as Ir[89] and Rh[90] has also been demonstrated using combustion chemistry. These metal ALD systems are being explored by the semiconductor industry. Ruthenium is under consideration as a seed for Cu electrodeposition for backend interconnects.[91] Ru ALD is a possible seed for Cu deposition in part because of the lattice match between the stable hexagonal plane of Ru(001) and the closed-packed face-centered cubic Cu(111) plane.[92]

5.3. Hydrogen Reduction Chemistry

There have also been attempts to develop metal ALD based on various organometallic precursors and H_2 reduction. The first efforts focused on Cu ALD using CuCl and H_2 as the reactants.[93] Copper films were reported to be grown on tantalum substrates.[93] However, CuCl is problematic as a copper source.[94] Additional studies explored Cu ALD using Cu(II)-2,2,6,6-tetramethyl-3,5-heptanedionate ($Cu(thd)_2$) and H_2 as the reactants.[95] Area-selective ALD was achieved on platinum seeded substrates.[95]

Cu ALD has also been accomplished using another copper β-diketonate, Cu(II) 1,1,1,5,5,5-hexafluoroacetylacetonate ($Cu(hfac)_2$), and various organic reduction agents such as methanol, ethanol, and formalin.[96,97] Very good conformal Cu ALD films were reported on trenched substrates.[96,97] The ALD of other metals has also been demonstrated using organic reducing agents. Pd ALD has been demonstrated using $Pd(hfac)_2$ and formalin.[98] H_2 was also reported to be effective as the reducing agent for Pd ALD after the nucleation of the Pd ALD films using formalin as the reducing agent.[98]

Alternative approaches to metal ALD have focused on depositing a metal oxide and then reducing this metal oxide with H_2 or other reducing agents. This method circumvents the fairly unreactive metal surface following H_2 reduction. During metal oxide ALD, there is an oxide or M—OH species on the surface to react with the organometallic precursor. This approach has been demonstrated for the growth of NiO

films using Ni acetylacetonate (Ni(acac)$_2$) and O$_3$ and the subsequent reduction to Ni films using H$_2$.[99] A similar technique was developed using bis(cyclopentadienyl)nickel and H$_2$O as the reactants for NiO growth and then hydrogen radicals for the reduction to Ni metal.[100] In addition, there are continued efforts to extend the range of metal precursors that will facilitate metal ALD using H$_2$ reduction chemistry. New families of metal precursors have been explored for metal ALD including the metal acetamidinates.[101]

6. Nucleation and Growth during ALD

The nucleation of ALD is extremely important for continuous and pinhole-free ultrathin films. If the ALD precursors do not effectively react with the initial substrate, then the ALD film may not nucleate at all or may nucleate only at particular defect sites on the initial substrate. This lack of uniform nucleation can produce island growth as described by a Volmer−Weber growth mechanism.[102] After multiple ALD cycles, the islands may grow together and form a continuous film. However, in the ultrathin film regime, the ALD films are rough and not conformal to the initial substrate.

6.1. Metal Oxide ALD on H−Si(100)

The lack of nucleation is very serious for the deposition of ultrathin dielectric films such as the high dielectric constant gate oxides in MOSFETs. These gate oxides need to be ultrathin and extremely conformal to ensure uniform electrical performance across the entire gate oxide. The nucleation of the high k gate oxides on the initial hydrogen-passivated Si(100) surfaces has been one of the most challenging nucleation problems for ALD. Many ALD nucleation studies have focused on this important technological problem.

Effective nucleation for ALD requires surface chemical species that will react with the ALD precursors. To obtain a uniform layer-by-layer ALD film growth as described by the Frank van der Merwe mechanism,[102] the ALD precursor needs to react with the initial surface species on the very first ALD cycle. This type of efficient nucleation is observed for metal oxide ALD on oxide substrates and usually for metal nitride ALD on oxide substrates. Oxide surfaces have MOH* hydroxyl groups that are typically reactive with organometallic precursors. The organometallic precursors are also usually reactive with H$_2$O and NH$_3$ that are commonly employed for metal oxide and metal nitride ALD, respectively.

Inefficient ALD nucleation is observed for metal oxide ALD on hydrogen-passivated Si(100) surfaces (H−Si(100)). The nucleation of ZrO$_2$ ALD and HfO$_2$ ALD has been reported on H−Si(100) because of the importance of these high dielectric constant materials as replacements for the thermal SiO$_2$ on Si(100) in MOSFETS.[103] Rutherford backscattering spectroscopy (RBS) was used to measure the ZrO$_2$ thickness on H−Si(100) surfaces as a function of the number of ALD cycles during ZrO$_2$ ALD using ZrCl$_4$ and H$_2$O as the precursors.[103] The RBS measurements indicated that the ZrO$_2$ ALD film did not nucleate and achieve a linear growth per cycle until after 50−60 ALD cycles. Transmission electron microscopy (TEM) analysis also revealed that the ZrO$_2$ ALD films were very granular with distinct islands for nucleation on the H−Si(100) surface.[104] In contrast, the ZrO$_2$ ALD film nucleated efficiently and formed a very smooth and conformal film on an oxidized Si(100) surface.[104]
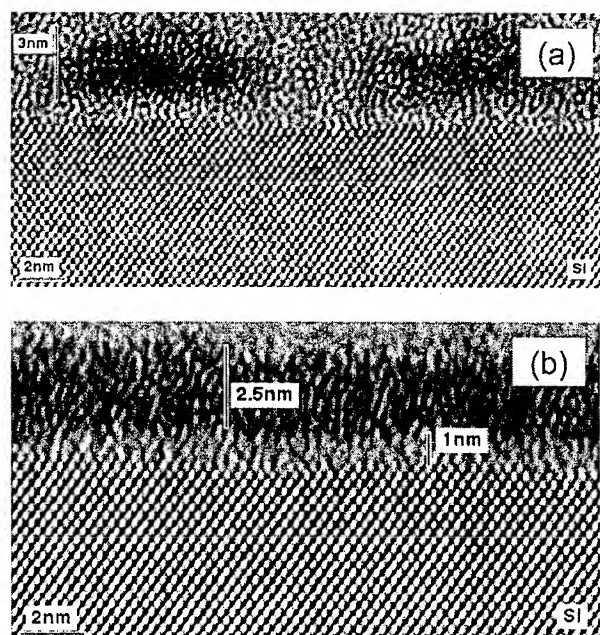

Figure 9. (a) Cross-section TEM image of a HfO$_2$ ALD film deposited on a Si wafer immediately after HF-last surface treatment. (b) Cross-section TEM image of a HfO$_2$ ALD film deposited on a SiO$_2$ layer on a Si wafer. (Reprinted with permission from ref 106. Copyright 2003 Elsevier.)

Similar results were obtained for the nucleation and growth of HfO$_2$ ALD on H−Si(100) surfaces. RBS measurements revealed that the HfO$_2$ ALD did not achieve a linear growth per cycle until after 25−30 ALD cycles using HfCl$_4$ and H$_2$O as the precursors.[105] Alternatively, a variety of oxides on Si(100) produced by chemical treatment or rapid thermal oxidation displayed very rapid nucleation and nearly linear HfO$_2$ ALD growth from the very first ALD cycle.[105] TEM measurements have captured the nonuniform islands of HfO$_2$ ALD on the initial H−Si(100) surface as shown in Figure 9a and the conformal HfO$_2$ ALD film on the oxide on the initial Si(100) surface as displayed in Figure 9b.[106] These studies reveal that a thin oxide coating is required for the efficient nucleation of ZrO$_2$ or HfO$_2$ ALD on Si(100). This SiO$_2$ coating must be kept ultrathin to avoid the effects of the lower SiO$_2$ dielectric constant on the gate stack.

Al$_2$O$_3$ ALD also displayed nucleation difficulties on H−Si(100).[103] Measurements of the Al$_2$O$_3$ ALD film thickness versus number of ALD cycles indicated that 10−15 ALD cycles were required to obtain a linear growth per cycle.[103] These studies were performed using Al(CH$_3$)$_3$ and H$_2$O as the ALD precursors. Additional studies investigated the mechanism of Al$_2$O$_3$ ALD on H−Si(100) using in situ Fourier transform infrared (FTIR) studies.[107,108] H$_2$O did not react with the H−Si(100) surface even after extremely large H$_2$O exposures. There was evidence for some reactivity of Al(CH$_3$)$_3$ or Al(CH$_3$)OH with the H−Si(100) surface. The H$_2$O could then react with AlCH$_3$* surface species and progressively nucleate Al$_2$O$_3$ ALD on the H−Si(100) surface.

6.2. Metal ALD on Oxide Surfaces

Metal ALD on oxide surfaces is another ALD system that displays nucleation difficulties. This nucleation problem is not surprising, since metals do not generally wet oxide surfaces. Many studies in heterogeneous catalysis indicate that metals prefer to form clusters on oxide surfaces. W ALD
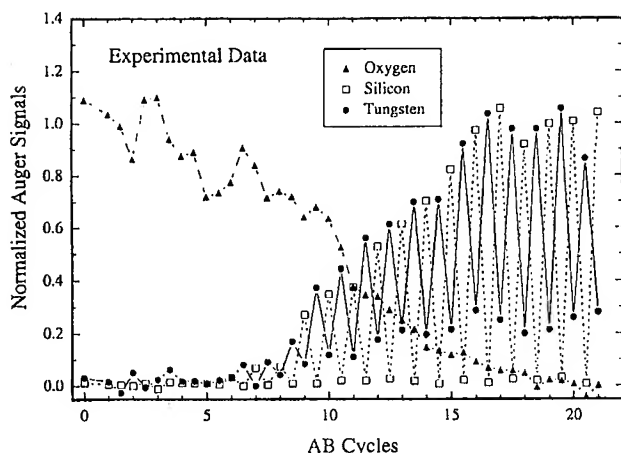
Figure 10. Normalized Auger electron spectroscopy (AES) signals versus AB cycles during W ALD on a SiO$_2$ surface using WF$_6$ and Si$_2$H$_6$ as the reactants. The AES signals at integer AB cycle numbers were recorded after the Si$_2$H$_6$ exposures. (Reprinted with permission from ref 109. Copyright 2001 Elsevier.)

using WF$_6$ and Si$_2$H$_6$ as the reactants has been studied thoroughly to understand the nucleation mechanism on SiO$_2$ and Al$_2$O$_3$ substrates. Auger electron spectroscopy (AES) investigations have shown that W ALD requires approximately 8−9 cycles to nucleate on SiO$_2$ surfaces[109] and approximately 3−4 cycles on Al$_2$O$_3$ surfaces.[110] The AES results for W ALD nucleation on SiO$_2$ surfaces are shown in Figure 10.[109] The nucleation period can be shortened to 4−5 cycles for W ALD on SiO$_2$ by much larger Si$_2$H$_6$ exposures on the first ALD cycle. Likewise, the nucleation is also facilitated by electron beam irradiation of the Al$_2$O$_3$ surface.[109]

The nucleation of W ALD on Al$_2$O$_3$ is important in the growth of precise W/Al$_2$O$_3$ nanolaminates using W ALD and Al$_2$O$_3$ ALD. QCM investigations have observed the nucleation delay for W ALD on Al$_2$O$_3$. The nucleation of W ALD on the Al$_2$O$_3$ ALD surface is observed to require 3−4 cycles using larger Si$_2$H$_6$ exposures, in good agreement with the

AES investigations.[111] In addition, the growth per cycle during the W ALD nucleation provides evidence for an island growth mechanism.[111]

The W ALD growth per cycle is initially very small during the first several W ALD cycles. The W ALD growth per cycle then increases dramatically and reaches a maximum before reducing to a slightly smaller W ALD growth per cycle. This behavior is expected as W ALD islands grow and then grow together and coalesce to form a continuous film.[112,113] More recent studies have also observed that the roughness of the W ALD surface is highest in the region where the islands are initially growing rapidly prior to reaching the maximum W ALD growth per cycle.[114] A correlation between the root-mean-square surface roughness measured by atomic force microscopy (AFM) and the W ALD growth per cycle is shown in Figure 11.[114]

6.3. Al$_2$O$_3$ ALD on Carbon Nanotubes and Graphene Surfaces

Another example of nucleation difficulty for ALD is Al$_2$O$_3$ ALD on carbon nanotubes (CNTs). The surface of the CNT is very inert and does not contain chemical species that allow for the reaction of either Al(CH$_3$)$_3$ or H$_2$O during Al$_2$O$_3$ ALD. As a result, Al$_2$O$_3$ ALD on single-walled and multiwalled CNTs yields only the growth of isolated Al$_2$O$_3$ nanospheres.[115,116] These nanospheres are believed to originate from specific defects on the surface of the CNTs. The nucleation of the Al$_2$O$_3$ ALD can be facilitated by the functionalization of the CNTs with nitroaniline or NO$_2$.[115−117] The NO$_2$ group on the surface of the CNTs provides a chemical site for the adsorption of Al(CH$_3$)$_3$ and yields a very conformal Al$_2$O$_3$ ALD film on the CNTs after multiple Al$_2$O$_3$ ALD cycles.

Nucleation difficulties are also encountered for ALD on graphene surfaces. Like the CNT surface, the graphene surface is inert. Al$_2$O$_3$ ALD and HfO$_2$ ALD have resulted in the growth of nanoribbons only along the step edges of the graphene surface.[118] The step edges are believed to serve as ALD nucleation sites.[118] Ozone has also been employed to create nucleation sites on the basal plane of graphene for Al$_2$O$_3$ ALD.[119] Chemical treatment using perylene tetracarboxylic acid has also been used to functionalize graphene for Al$_2$O$_3$ ALD.[120]

7. Low Temperature ALD

The ability to perform ALD at low temperatures is important to maintain a low thermal budget to prevent the interdiffusion of materials. This problem is particularly severe for nanostructured devices. Low temperature ALD is also needed for ALD on thermally fragile substrates such as polymeric or biological samples. Fortunately, several ALD systems can be performed at low temperatures because of their favorable thermochemistry. A few other special ALD systems can be facilitated to occur at much lower temperatures using a catalyst.

7.1. Al$_2$O$_3$ ALD and Other Metal Oxide ALD

The high exothermicity of the Al$_2$O$_3$ ALD surface reactions enables this ALD system to be performed at temperatures as low as room temperature.[43] QCM investigations have revealed that Al$_2$O$_3$ ALD can be grown over a wide range of temperatures with little change in the growth per cycle.[43] The Al$_2$O$_3$ ALD films do show a small decrease in
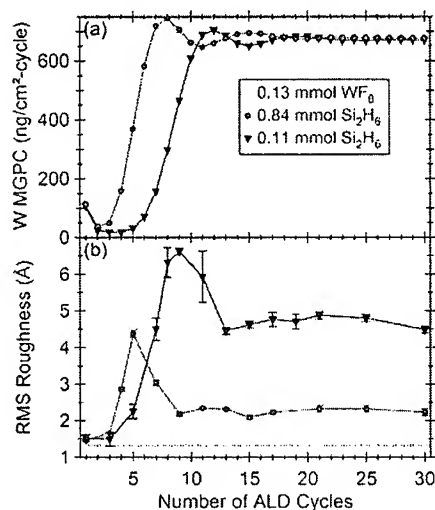

Figure 11. (a) W ALD mass gain per cycle and (b) root-mean-squared (rms) roughness for W ALD on a hydroxylated Al$_2$O$_3$ surface at 122 °C for WF$_6$ reactant exposure of 0.13 mmol and two different Si$_2$H$_6$ exposures of 0.11 and 0.83 mmol. (Reprinted with permission from ref 114. Copyright 2009 American Institute of Physics.)
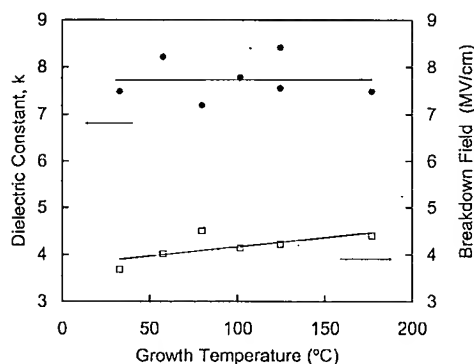
Figure 12. Dielectric constant and breakdown field of low-temperature Al_2O_3 ALD films grown using 300 AB cycles on n-Si(100). (Reprinted with permission from ref 43. Copyright 2004 American Chemical Society.)

density from 3.0 g/cm³ at 177 °C to 2.5 g/cm³ at 33 °C. In addition, the refractive index also decreases slightly, as expected from the reduction of the density. The quality of the Al_2O_3 ALD films is excellent over this entire temperature range.[43] XRR studies of the Al_2O_3 ALD films indicate that the films are very conformal to the initial substrate and display minimal surface roughness even for films deposited at 33 °C.

The major issue for Al_2O_3 ALD at low temperatures is the required purge times to avoid Al_2O_3 CVD. QCM studies have shown that the minimum purge times are 1 and 5 s after the $Al(CH_3)_3$ and H_2O exposures, respectively, at 177 °C.[43] These minimum purge times increased to 20 and 180 s after the $Al(CH_3)_3$ and H_2O exposures, respectively, at 33 °C.[43] The large increase in the purge time after the H_2O exposure results from the high desorption activation energy for H_2O from the surfaces of the ALD reactor. Slow H_2O desorption rates at low temperature lead to much longer required purge times to avoid Al_2O_3 CVD.

Forward recoil spectrometry of the Al_2O_3 ALD films has also revealed that the hydrogen atom % increases in Al_2O_3 ALD films grown at low temperatures.[43] The hydrogen atom % was ~6% for Al_2O_3 ALD films grown at 177 °C. The hydrogen atom % increased to ~22% for Al_2O_3 ALD films grown at 33 °C. Although the hydrogen atom % increased at lower temperatures, some of the electrical properties of the Al_2O_3 ALD films remained largely unchanged over the entire temperature range. The dielectric constant of the Al_2O_3 ALD films was constant at ~7−8, and the breakdown field was ~4 MW/cm from 33−177 °C, as shown in Figure 12.[43] Additional investigation of the Al_2O_3 ALD films is required to evaluate the fixed charge density and its dependence on the hydrogen atom %.

Several other ALD processes besides Al_2O_3 ALD have been demonstrated at low temperatures. These low temperature ALD systems have been reported in a recent review and are important for ALD on organic and biological substrates.[24] Some key ALD systems displaying growth at ≤100 °C are TiO_2 ALD using $TiCl_4$ and H_2O or $Ti(OiPr)_4$ and H_2O as the reactants[121,122] and ZnO ALD using $Zn(Et)_2$ and H_2O as the reactants.[123] These low temperature ALD systems enable ALD on polymers and ALD on organic and biological templates, as discussed in sections 8 and 13.
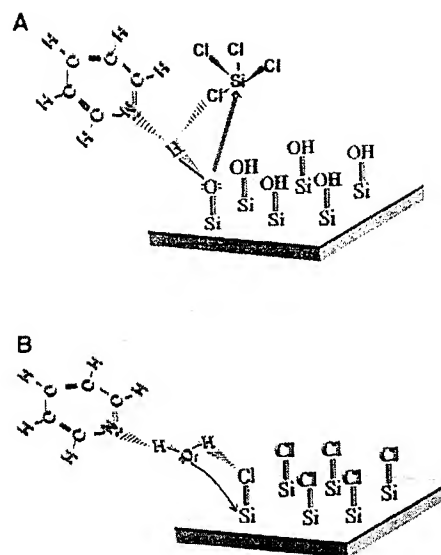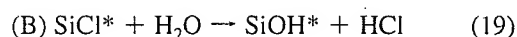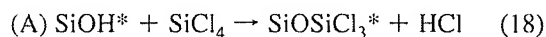

Figure 13. Proposed mechanism for Lewis base catalysis of SiO_2 ALD during (a) the $SiCl_4$ reaction and (b) the H_2O reaction. (Reprinted with permission from ref 127. Copyright 1997 American Association for the Advancement of Science.)

7.2. Catalytic SiO_2 ALD

The use of catalysts for gas phase deposition during ALD or CVD is very unusual. One ALD system that can be catalyzed is SiO_2 ALD using $SiCl_4$ and H_2O as the reactants. SiO_2 ALD is based on the binary reaction

$$SiCl_4 + 2H_2O \rightarrow SiO_2 + 4HCl \qquad \Delta H = -32 \text{ kcal} \qquad (17)$$
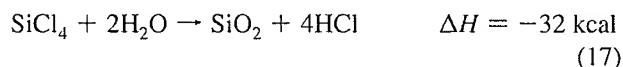
Although this reaction has a reasonable negative reaction enthalpy,[33] the ALD surface reactions are very slow and only occur at high temperature after very large $SiCl_4$ and H_2O exposures.[124] The surface reactions for SiO_2 ALD are[74,124−127]

$$(A) \quad SiOH^* + SiCl_4 \rightarrow SiOSiCl_3^* + HCl \qquad (18)$$

$$(B) \quad SiCl^* + H_2O \rightarrow SiOH^* + HCl \qquad (19)$$

Fortunately, SiO_2 ALD can be catalyzed using other molecules. The catalysts for the SiO_2 ALD surface chemistry are Lewis bases such as pyridine or NH_3 (ammonia).[126,127] The SiO_2 ALD growth is catalyzed only when the Lewis base is present during both the $SiCl_4$ and H_2O surface reactions. Additional studies have shown that Lewis bases can also catalyze SiO_2 ALD using other silicon precursors such as $Si(OCH_2CH_3)$ (tetraethoxysilane (TEOS)).[128]

The mechanism for the catalysis is believed to be the hydrogen bonding between the Lewis base and either the SiOH* surface species during the $SiCl_4$ reaction or the H_2O reactant during the H_2O reaction.[126,127,129,130] A schematic illustrating this mechanism is displayed in Figure 13.[127] The hydrogen bonding between the Lewis base and the SiOH* surface species weakens the SiO−H chemical bond and makes the oxygen a stronger nucleophile. This hydrogen bonding interaction facilitates the nucleophilic attack by the oxygen on the electropositive Si atom in the $SiCl_4$ reactant. Likewise, the hydrogen bonding between the Lewis base and the H_2O reactant makes the oxygen in H_2O a stronger nucleophile for nucleophilic attack on the electropositive Si atom in the SiCl* surface species.

The effect of the Lewis base catalyst is very dramatic. Without pyridine as the Lewis base catalyst, SiO$_2$ ALD using SiCl$_4$ and H$_2$O as the reactants requires reaction temperatures of >325 °C and reactant exposures of ~10^9 Langmuirs (1 Langmuir = 1 × 10^{-6} Torr s).[124] With pyridine as the Lewis base catalyst, SiO$_2$ ALD can occur at temperatures close to room temperature with reactant exposures of only ~10^4 Langmuirs.[127] A variety of techniques such as QCM, XRR, ellipsometry, and profilometry have measured very linear SiO$_2$ ALD at 32 °C in a viscous flow ALD reactor with a growth per cycle of ~1.35 Å.[131] The resulting SiO$_2$ films have reasonable dielectric properties, although they are inferior to thermal SiO$_2$ oxide films.

One of the problems with catalytic SiO$_2$ ALD is the secondary reaction between the pyridine or NH$_3$ Lewis base catalyst and the HCl reaction product to form a salt.[126,127,129,131] These pyridium or ammonium chloride salts have a finite vapor pressure and will desorb from the growing SiO$_2$ ALD film. However, the salts can accumulate on the SiO$_2$ ALD surface and poison the SiO$_2$ ALD growth if there is insufficient time for desorption. SiO$_2$ ALD with TEOS as the silicon precursor was attempted to avoid HCl as a reaction product and to eliminate the salt formation.[128] SiO$_2$ ALD could be accomplished using NH$_3$ as the catalyst. However, the catalyzed SiO$_2$ ALD reaction was much less efficient with TEOS compared with SiCl$_4$ as the silicon reactant.[128]

Another limitation of catalytic SiO$_2$ ALD is the limited temperature range over which the Lewis base can catalyze the SiO$_2$ ALD surface reactions.[126,127,131] The catalysis requires the presence of the Lewis base on the SiO$_2$ ALD surface. FTIR investigations can determine the interaction of the pyridine and NH$_3$ Lewis base catalysts with the SiOH* surface species by monitoring the SiO-H stretching vibration.[129,131] These studies reveal that the Lewis base interaction with SiOH* surface species is progressively removed because of Lewis base desorption at temperatures > 30 °C.[129,131] The desorption temperature can be shifted by the pressure of the Lewis base catalyst. The Lewis base coverage is determined by the steady state established by the Lewis base adsorption and desorption rates.

Other ALD systems should also display similar catalytic effects using Lewis bases. These systems are other metal oxides such as SiO$_2$, where the MOH* surface hydroxyl is acidic and can transfer a proton to liquid water. The Lewis base will hydrogen bond strongly to these acidic hydroxyl groups and make the oxygen more nucleophilic. Good candidates are metal oxides that are known to have their isoelectric points in water at pH < 7.[132] These metal oxides include TiO$_2$, ZrO$_2$, and SnO$_2$.[132] One study has reported the catalysis of TiO$_2$ CVD using TiCl$_4$ and H$_2$O with NH$_3$ as the Lewis base catalyst.[133]

8. ALD on Polymers

Low temperature ALD enables ALD on thermally sensitive materials such as organic polymers. ALD on polymers may be useful to functionalize the polymer surface, to create unique inorganic/organic polymer composites, and to deposit gas diffusion barriers on polymers. ALD on polymers was not performed until recently because polymers decompose at the temperatures required for many ALD systems. In addition, most polymers do not contain the necessary surface chemical species that were believed to be necessary to initiate ALD.
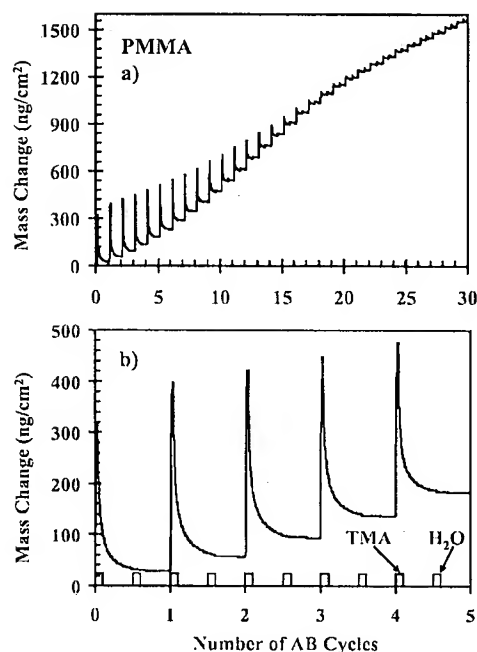

Figure 14. (a) Mass change measured by a quartz crystal microbalance versus the number of AB cycles during Al$_2$O$_3$ ALD on PMMA at 85 °C for 30 AB cycles. (b) Mass change at higher mass resolution for the first five AB cycles shown in part a. (Reprinted with permission from ref 134. Copyright 2005 American Chemical Society.)

In situ FTIR studies revealed the nucleation and growth mechanism for Al$_2$O$_3$ ALD using Al(CH$_3$)$_3$ and H$_2$O as the reactants on polyethylene particles.[36] The H$_2$O reactant was not observed to interact or adsorb into the polyethylene particles. In contrast, the Al(CH$_3$)$_3$ reactant was observed to diffuse into the polyethylene. After the adsorption of Al(CH$_3$)$_3$, the subsequent H$_2$O exposure led to the reaction of H$_2$O with Al(CH$_3$)$_3$ to form AlOH* species. These AlOH* species are believed to be from Al(OH)$_4$ clusters in the near surface region of the polyethylene particles. The FTIR studies also observed the progressive growth of infrared features consistent with bulk Al$_2$O$_3$.[36] Subsequent examination after 40 ALD cycles revealed the presence of a thin Al$_2$O$_3$ film on the polyethylene particles.

Additional QCM studies of Al$_2$O$_3$ ALD on polymer films spin-coated onto QCM sensors further clarified and confirmed the mechanism for ALD on polymers.[134] The QCM investigations observed the nucleation and growth of Al$_2$O$_3$ ALD on polymer films with thicknesses from 2400 to 4000 Å. A variety of polymers were studied, including polymethylmethacrylate (PMMA), polypropylene, polystyrene, polyethylene, and polyvinylchloride. The key observation from the QCM studies was the large mass gain and loss corresponding to the diffusion of Al(CH$_3$)$_3$ into the polymer film during TMA exposure and out of the polymer film after the TMA exposure during the initial ALD cycles.

The diffusion effects were especially pronounced on the PMMA polymer films. QCM results for Al$_2$O$_3$ ALD for the first several ALD cycles on PMMA at 86 °C are shown in Figure 14.[134] Figure 14a shows the QCM results during the first 30 Al$_2$O$_3$ AB cycles. Figure 14b displays the QCM results for the first 5 Al$_2$O$_3$ AB cycles. These results show that the diffusion of TMA in and out of the PMMA polymer film was only observed for the first 10–15 ALD cycles.[134] As the Al$_2$O$_3$ ALD film grows in the near surface region of
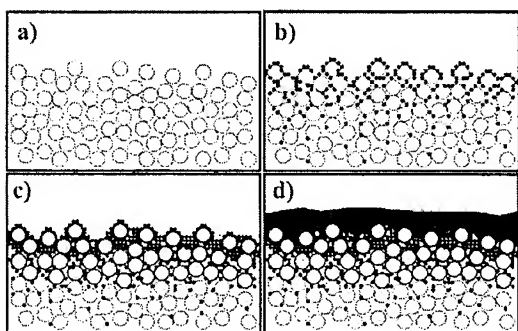
Figure 15. Model for Al_2O_3 ALD on polymer films showing (a) a cross section of the polymer chains at the surface of the polymer film, (b) Al_2O_3 nucleation clusters formed from H_2O reaction with TMA trapped in the near surface region, (c) coalescence of Al_2O_3 clusters and closure of the space between the polymer chains, and (d) formation of a dense Al_2O_3 film that grows on top of the polymer surface. (Reprinted with permission from ref 134. Copyright 2005 American Chemical Society.)

the polymer and begins to form a continuous film, the Al_2O_3 ALD film hinders the TMA diffusion. This Al_2O_3 barrier film then prevents any TMA diffusion and the QCM measurements observe only the linear growth of the Al_2O_3 ALD film after >15 ALD cycles.

These results suggest the following mechanism for ALD on polymers:[134] (1) one of the ALD precursors, such as TMA, diffuses into the near surface region of the polymer; (2) clusters of the ALD material form in the near surface region as a result of the bimolecular reaction between the two ALD precursors; (3) the clusters grow and eventually begin to coalesce; (4) a continuous film is formed that prevents the diffusion of additional precursor into the polymer; and (5) the ALD material grows linearly on the continuous ALD film. This mechanism is illustrated in Figure 15.[134] The open circles represent a cross section of polymer chains.

The QCM results suggest that the Al_2O_3 ALD films using $Al(CH_3)_3$ and H_2O may be effective gas diffusion barriers on polymers. Additional studies have explored the use of Al_2O_3 ALD films as gas diffusion barriers. Investigations of Al_2O_3 ALD on polyethylenenaphthalate (PEN) and Kapton have shown that Al_2O_3 ALD films as thin as 10 nm can reduce the water vapor transmission rate (WVTR) over 3 orders of magnitude to $\leq 1 \times 10^{-3} - 1 \times 10^{-4}$ g/m^2/day depending on the test measurement technique.[135,136] Even lower WVTRs were measured with bilayer or multilayer barriers fabricated using Al_2O_3 ALD and SiN plasma-enhanced CVD,[137] Al_2O_3 ALD and rapid SiO_2 ALD,[138] and Al_2O_3 ALD and ZrO_2 ALD.[139] Other studies using plasma ALD with $Al(CH_3)_3$ and O_2 plasma have also produced very effective Al_2O_3 ALD gas diffusion barriers with WVTR ~ 5×10^{-3} g/m^2/day.[61]

Many of the applications for ALD on polymers have utilized Al_2O_3 ALD. Al_2O_3 ALD has been employed to encapsulate organic light emitting diodes[140,141] and organic solar cells[142] for hermetic sealing to prevent H_2O permeation. Al_2O_3 ALD has also been effective as a capping layer[143] and a gate dielectric[144] for polymer-based transistors. Surface modification of natural fiber and woven fabric materials has utilized Al_2O_3 ALD.[145] Al_2O_3 ALD on electrospun polymer fibers has also been used to fabricate Al_2O_3 microtubes.[146] Polymers have also been protected from erosion by oxygen atoms using Al_2O_3 ALD.[147] In addition to Al_2O_3 ALD, TiO_2 ALD on polystyrene spheres has been employed to fabricate nanobowl arrays,[148] TiO_2 ALD and ZrO_2 ALD on polycar-

bonate membranes has been utilized to form TiO_2 and ZrO_2 nanotubes,[149] and W ALD has been demonstrated to form tungsten metal films on polymers.[150]

9. ALD on High Aspect Ratio Structures

The ability of ALD to deposit on high aspect ratio structures is one of the most desirable characteristics of ALD. The miniaturization of semiconductor devices has led to the increasing need for ALD to coat high aspect ratio structures. The main examples are the deposition of Cu diffusion barriers for backend interconnects[51] and the deposition of dielectric layers to fabricate DRAM capacitors for memory storage.[2] Outside of the semiconductor industry, the ability of ALD to deposit on high aspect ratio structures is also useful for ALD fabrication of the half-gap dielectric on magnetic read/ write heads[3] and ALD on MEMS devices for surface functionization and protection.[151]

ALD on high aspect ratio structures can be understood by model studies of ALD on well-defined structures with high aspect ratios. One such well-defined structure is anodic aluminum oxide (AAO).[152] AAO is defined by linear pores that are aligned approximately parallel to each other. In addition, the pores are arranged with approximately hexagonal symmetry. The preparation of AAO is achieved by electrochemical anodization of aluminum films. This anodization yields AAO films with typical thicknesses of ~50 μm and pore diameters of ~50 nm for an aspect ratio of ~1000.

Studies of Al_2O_3 ALD in AAO using scanning electron microscopy (SEM) analysis have revealed that conformal ALD coating of high aspect ratio structures is dependent on the ALD exposure times.[153] For AAO with a thickness of ~50 μm and pore diameters of ~65 nm that were open to the gas phase ALD reactants on both sides of the AAO film, exposure times of 1 s were insufficient to obtain a conformal ALD coating in the interior of the AAO film. Reactant exposures of ~30 s were required to obtain a nearly conformal coating.[153]

Additional investigations of ZnO ALD on AAO were performed using electron microprobe analysis with energy dispersive spectroscopy (EDS).[153] These EDS studies were able to resolve the ZnO coverage on the AAO pores versus distance into the AAO film. ZnO coverages were observed that decreased versus distance into the AAO film, as shown in Figure 16a.[153] The decrease was much sharper for the shorter ALD exposure times. The ZnO ALD coverage could be integrated to obtain the total amount of ZnO ALD in the AAO film versus exposure time, as displayed in Figure 16b.[153] The integrated ZnO ALD coverage increased with $t^{1/2}$, where t is the exposure time. These results are consistent with gas diffusion limiting the flux of reactants into the pores of AAO.

The $t^{1/2}$ dependence of the integrated ZnO ALD coverage versus exposure time suggested that the ZnO ALD could be understood using kinetic gas theory. Consequently, Monte Carlo modeling was performed assuming that the ZnO ALD was limited by the diffusion of diethylzinc in the pores of AAO.[153] This modeling confirmed the $t^{1/2}$ dependence and obtained nearly quantitative agreement with the integrated ZnO ALD coverage using the known parameters for the system with no fitting parameters. This agreement suggests that ALD in high aspect ratio structures can be understood in terms of gas kinetic theory with ALD reactants in molecular flow.
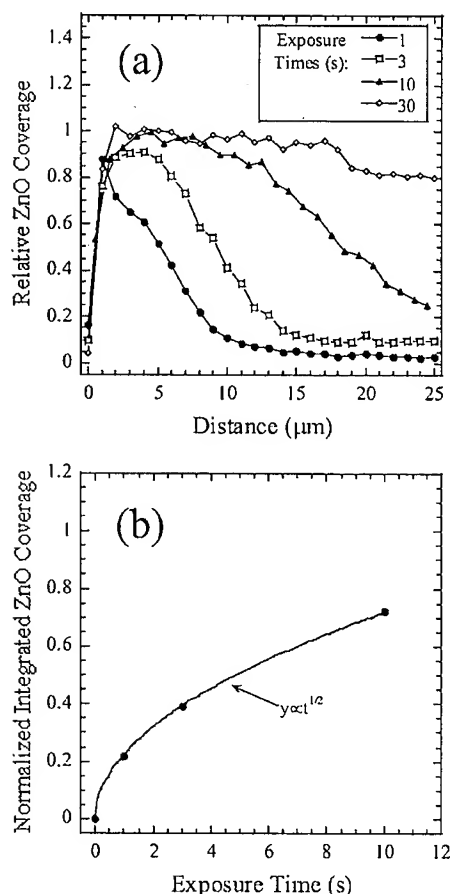
Figure 16. (a) Relative ZnO coverage measured by electron probe microanalysis line scan and (b) normalized integrated ZnO coverage following 64 AB cycles of ZnO ALD using exposure times of 1, 3, 10, and 30 s. (Reprinted with permission from ref 153. Copyright 2003 American Chemical Society.)

The exposure time required to obtain conformal ALD in high aspect ratio structures can be predicted using the results from the Monte Carlo modeling. The results from the simulations for ZnO ALD in high aspect ratio cylinders yield the relationship $T = 1/k^2$, where T is the exposure time required for the normalized integrated coverage, Θ^*, to reach $\Theta^* = 1$. The parameter k is given by[153]
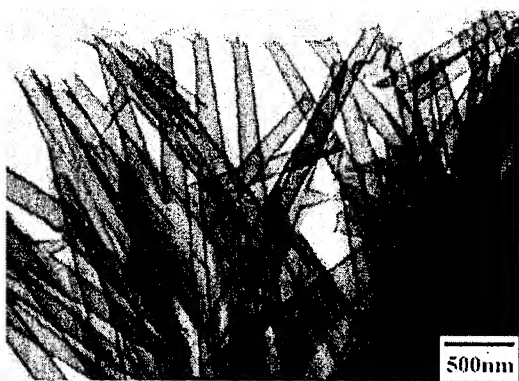

Figure 17. TEM image of ZrO_2 nanotubes fabricated in polycarbonate templates with 200 nm pores. The ZrO_2 nanotubes are 200 nm in diameter. (Reprinted with permission from ref 149. Copyright 2004 John Wiley & Sons.)

$$k\ (s^{-1/2}) = 2.1 \times 10^3\ P^{1/2} m^{-1/4} N^{-1/2} (d/L) \quad (20)$$

In this equation, P is the pressure (Torr), m is the mass (amu) of diethylzinc for ZnO ALD, N (cm^{-2}) is the number of surface sites, and the aspect ratio is L/d, where L and d are the length and diameter of the cylinder.

The relationship $T = 1/k^2$ indicates that the required exposure time for conformal ALD scales as the square of the aspect ratio, i.e. $T \propto (L/d)^2$. As an example of using this relationship, for $P = 5$ Torr, an aspect ratio of $L/d = 5000$, $m = 123$ amu for diethylzinc, and $N = 0.84 \times 10^{15}$ cm^{-2}, the required exposure time for conformal ALD is $T = 11$ s. Although longer times are required for high aspect ratios, the required exposure times are not prohibitively long even for high aspect ratios.

Another treatment has derived the required exposure times for conformal ALD using gas conductance equations.[154] This treatment also predicts that the required exposure for conformal ALD scales as the square of the aspect ratio in the limit of large aspect ratios. Assuming a unity reactive sticking coefficient, the total required exposure is equal to the product of the pressure, P, and the time, t, and is given by[154]

$$(Pt)_{total} = S(2\pi mkT)^{1/2}\{1 + (^{19}/_4)(L/d) + (^3/_2)(L/d)^2\} \quad (21)$$

In this equation, S is the saturated surface density and L/d is the aspect ratio for a cylinder.

$S(2\pi mkT)^{1/2}$ is the exposure required for a flat surface to be reacted to completion assuming a unity reactive sticking coefficient.[154] A reactive sticking coefficient, Γ, less than unity will increase the exposure according to $S(2\pi mkT)^{1/2}/\Gamma$. In the limit of large aspect ratios, the $(L/d)^2$ term dominates in the term $\{1 + (19/4)(L/d) + (^3/_2)(L/d)^2\}$ and the required exposure is proportional to the square of the aspect ratio. The exposure time derived from eq 21 can be shown to agree with the exposure time $T = 1/k^2$, where k is given by eq 20.

There are many examples of ALD on high aspect ratio structures. Outside of the semiconductor arena, ALD on high aspect ratio MEMS devices is important to deposit protective coatings,[151,155] hydrophobic layers,[156] and lubricating films.[157] As mentioned earlier when discussing ALD on polymers, ALD on porous polycarbonate membranes is utilized for nanotube fabrication[149] and ALD on self-assembled polystyrene spheres allows for the formation of nanobowl arrays.[148] Figure 17 shows a TEM image of ZrO_2 ALD nanotubes fabricated in a high aspect ratio polycarbonate membrane with 200 nm pore diameters.[149]

ALD on AAO has been utilized to form Fe_2O_3 nanotube arrays with controlled geometry and tunable magnetism.[158] Ferromagnetic Ni and Co nanotubes have also been grown in AAO using ALD methods.[159] ALD on high aspect ratio self-assembled opal structures has been employed for the fabrication of photonic crystals.[123,160-162] ALD on porous substrates and aerogels has also been a novel avenue for the fabrication of high surface area catalysts.[163-165]

10. ALD on Particles

There are many applications for ALD on particles. The surface chemical properties of particles can be modified by ALD while retaining the bulk properties of the original particles. ALD can also deposit protective and insulating coatings on particles to prevent particle oxidation[166] or
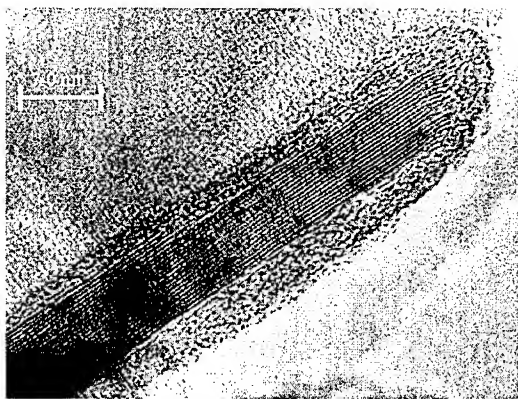
Figure 18. TEM image of HCV grade BN coated with Al_2O_3 ALD in a fluidized bed reactor. (Reprinted with permission from ref 172. Copyright 2004 Elsevier.)

Figure 19. TEM image of ZrO_2 nanoparticles with an average diameter of 62 nm coated with 50 AB cycles of Al_2O_3 ALD. (Reprinted with permission from ref 41. Copyright 2007 American Institute of Physics.)

electrical conduction.[167] ALD coatings on particles can also serve to modify the optical[168] or mechanical[169] properties of the particles. In addition, various composite core/shell structures can be fabricated using ALD on particles that may have a designed chemical reactivity.[170]

ALD on particles depends on the ability of ALD to produce conformal coatings on high aspect ratio structures. A bed of particles will have an effective aspect ratio that is defined by the particle size and shape.[41] A static particle bed will appear to the gas phase ALD reactants like a porous substrate.[41] A bed of fluidized particles will have much higher gas conductance.[171] The moving particles will allow the gas phase ALD reactants to encounter all the accessible particle surface area in a much shorter time. The agitation of the particles will also prevent the individual particles from being "glued together" in the particle bed by the ALD coating.

ALD on particles has been demonstrated in a fluidized particle bed.[172,173] During fluidization, the upward force of the pressure drop across the particle bed equals the downward force of gravity on the particle bed. The equal forces lead to the fluidation of the particles. Although particle aggregates form during fluidization, the aggregates are dynamic and the constant exchange of particles between the aggregates prevents the particles from being "glued together" during ALD. The initial demonstration of ALD on particles in a fluidized bed performed Al_2O_3 ALD on BN particles.[172] Excellent conformal coatings of Al_2O_3 ALD were observed on BN particles with a platelet shape as shown by the TEM image in Figure 18.[172]

ALD on particles has also been demonstrated in a rotary reactor that tumbles the particles in a porous metal cylinder to prevent agglomeration.[41] In contrast to the fluidized bed reactor, the rotary reactor can be operated using static exposures because a constant gas flux is not needed to fluidize the particles. The static exposures allow for much higher precursor utilization for efficient ALD surface reactions. High precursor utilization is especially critical for high surface area nanoparticles. Al_2O_3 ALD on ZrO_2 nanoparticles has been characterized in the rotary reactor.[41,174] A TEM image of a ZrO_2 nanoparticle coated in the rotary reactor with 80 AB cycles of Al_2O_3 ALD is shown in Figure 19.[41]

ALD on nanostructures such as nanotubes and nanowires faces similar issues to ALD on particles. For large quantities of nanotubes or nanowires, the nanostructures will also need to be fluidized or agitated in a rotary reactor to obtain high gas conductance for efficient ALD reactions. For many of
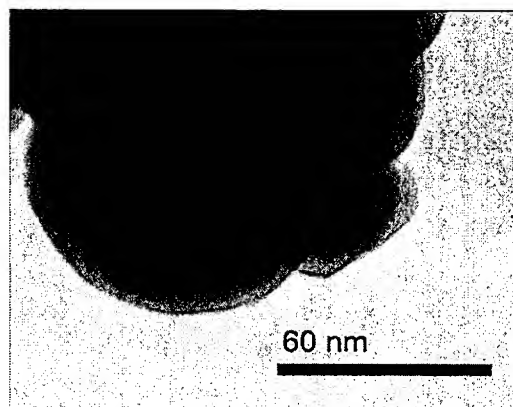
the reported studies of ALD on nanotubes and nanowires, the ALD was performed on individual nanostructures that provided adequate gas conduction without needing fluidization or agitation. Some of the early examples for ALD on nanotubes and nanowires include Al_2O_3 ALD on multiwalled carbon nanotubes (CNTs)[175] and Al_2O_3 ALD on ZnO nanorods.[176] Coaxial $Al_2O_3/W/Al_2O_3$ multilayer coatings were also demonstrated on multiwalled CNTs.[177] As mentioned earlier in section 6, Al_2O_3 ALD has also been demonstrated on single-walled CNTs.[116,117]

11. ALD of Nanolaminates and Alloys

The ALD of nanolaminates and alloys has many applications in semiconductor device fabrication and nanostructure engineering. The first report of nanolaminates fabricated using ALD examined HfO_2/Ta_2O_5 nanolaminates as low leakage dielectric films.[178] The HfO_2/Ta_2O_5 nanolaminates could be tuned to improve the charge storage in dielectric films. Other studies have demonstrated extremely conformal deposition of Al_2O_3/Ta_2O_5 and $Hf_xAl_yO_z$ alloy stacks in trench capacitors for DRAM capacitors.[2] Al_2O_3/TiO_2 nanolaminates with layer thicknesses much smaller than the wavelength of light have also been employed to tune the optical refractive index of the nanolaminate film over a wide range from $n = 2.4$ for TiO_2 to $n = 1.6$ for Al_2O_3.[179]

Nanolaminates can also be fabricated that display novel physical properties because the layer thickness is less than or equal to the length scale that defines the physical property.[180] For example, extremely hard films can be constructed when the layer thickness is less than the slip plane dislocation length. Thermal barrier coatings can be fabricated when the layer thickness is less than the phonon mean free path in the material. Studies of thermal conductivity have revealed that the thermal conductivity in Al_2O_3/W nanolaminates can decrease below the minimum value for yttria-stabilized ZrO_2.[181] The Al_2O_3/W nanolaminate was effective as a thermal barrier coating because of the large frequency difference between phonons in Al_2O_3 and W.[182]

Other studies have explored the use of TiO_2/Al_2O_3,[183] AlP/GaP,[184] and Al_2O_3/W^6 nanolaminates as Bragg mirrors. The 16-bilayer Al_2O_3/W superlattice displayed a reflectivity of $\sim$96% in the hard X-ray region for the Cu Kα line at $\lambda = 1.52$ Å.[6] This reflectivity is the highest reflectivity reported for a first-order Bragg peak in the hard X-ray region. In addition, Bragg peaks from this nanolaminate were observed
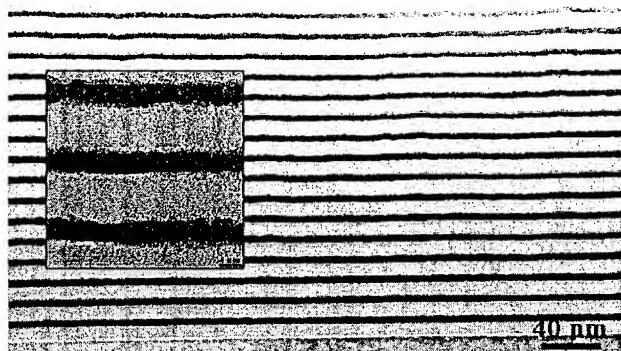
Figure 20. TEM image of a 16-bilayer Al₂O₃/W superlattice optimized for X-ray reflectivity at $\lambda = 1.54$ Å. The inset shows a high resolution TEM image. (Reprinted with permission from ref 6. Copyright 2006 American Institute of Physics.)

at larger angles up to the sixth-order Bragg peak. A TEM of this 16-bilayer Al₂O₃/W superlattice is shown in Figure 20.[6] Additional studies demonstrated high X-ray reflectivity for six-bilayer Al₂O₃/W superlattices deposited on polyethylenenaphthalate (PEN) substrates.[185] The resulting X-ray mirrors were extremely flexible and could be adjusted to obtain a wide range of curvatures.

The precise control over individual surface reactions during ALD also allows for the fabrication of alloys and graded materials. For example, if the temperature for the ALD reactions is similar for two ALD systems forming an alloy, then the alloy can be grown by alternating back-and-forth between the ALD cycles for the first material and the ALD cycles for the second material. The composition of the alloy can be controlled by the relative number of ALD cycles for each material. The relative number of ALD cycles of each material could also change progressively to fabricate a graded material.

An example of an alloy grown using ALD is the Al₂O₃/ZnO alloy. The Al₂O₃/ZnO alloy can be grown by alternating between the TMA and H₂O reaction cycles for Al₂O₃ ALD and the diethylzinc and H₂O reaction cycles for ZnO ALD.[186]
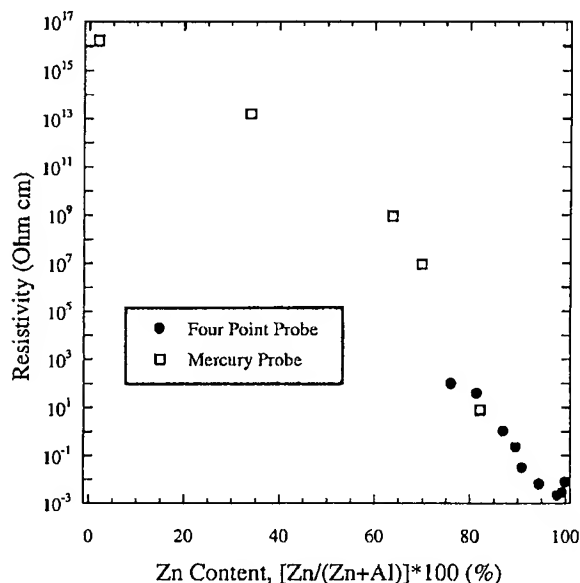

Figure 21. Resistivity of ZnO/Al₂O₃ alloy films measured using a four-point probe and a mercury probe. (Reprinted with permission from ref 187. Copyright 2003 The Electrochemical Society.)
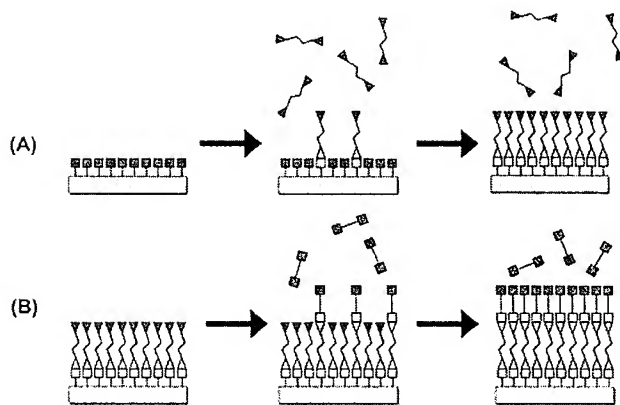

Figure 22. Schematic representation of MLD using self-limiting surface chemistry and an AB binary reaction sequence. (Reprinted with permission from ref 190. Copyright 2007 American Chemical Society.)
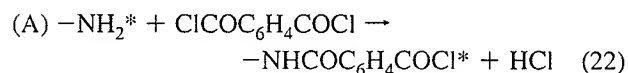
Although there are nucleation issues upon initiating the Al₂O₃ ALD cycles following the ZnO ALD cycles,[186] the relative number of Al₂O₃ ALD and ZnO ALD cycles can be changed to define a wide range of alloy compositions. Since Al₂O₃ ALD films are insulating and ZnO ALD films are conducting, variable resistivity films can be fabricated using Al₂O₃/ZnO alloys.[187] The resistivity of these alloys varies continuously from $\sim 10^{16}$ Ω cm for pure Al₂O₃ ALD to $\sim 10^{-2}$ Ω cm for pure ZnO ALD, as shown in Figure 21.[187] These alloys have been employed to define charge dissipative coatings for RF MEMS switches.[188]
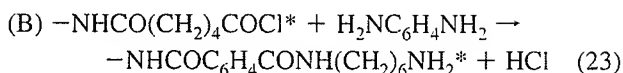
12. Polymer MLD

12.1. Organic Polymers

ALD processes have been developed for a wide range of inorganic materials. Similar self-limiting surface reactions can be employed for the growth of organic polymers. This film growth is described as molecular layer deposition (MLD) because a molecular fragment is deposited during each ALD cycle.[189] A cartoon illustrating the MLD process is shown in Figure 22.[190] MLD was initially developed for the growth of organic polymers such as polyamides[191] and polyimides.[189] The self-limiting surface strategies for MLD have also been called alternating vapor deposition polymerization (AVDP).[191] MLD developed from an earlier gas-phase polymer growth method known as vapor deposition polymerization (VDP).[192]

More recent work has renewed interest in the MLD of organic polymers.[193] The MLD of various polyamides using acyl chlorides and amines as the reactants has been studied using in situ Fourier transform infrared (FTIR) spectroscopy.[190,194] For poly(p-phenylene terephthalamide) (PPTA) MLD, the acyl chloride is terephthaloyl chloride (ClCOC₆H₄COCl) (TC) and the diamine is p-phenylenediamine (NH₂C₆H₄NH₂) (PD). The surface reactions for PPTA MLD are proposed as follows:[194]

$$(A) \; -NH_2{}^* + ClCOC_6H_4COCl \rightarrow$$
$$-NHCOC_6H_4COCl^* + HCl \quad (22)$$

(B) $-NHCO(CH_2)_4COCl^* + H_2NC_6H_4NH_2 \rightarrow$
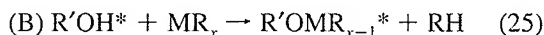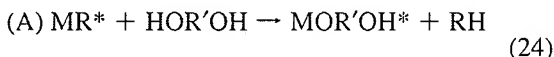
$\qquad -NHCOC_6H_4CONH(CH_2)_6NH_2^* + HCl$ (23)

where the asterisks again designate the surface species. The FTIR measurements observe self-limiting reactions during TC and PD exposures. The PPTA MLD growth is linear but varied between 0.5 and 4.0 Å per AB cycle for individual experiments. This variability was attributed to varying numbers of "double" reactions between the bifunctional reactants and the surface species.[194]

A number of other organic polymers have also been grown using MLD techniques. The MLD of polyurea using 1,4-phenylene diisocyanate and ethylene diamine as the reactants has been investigated using total internal reflection FTIR techniques.[195] Additional studies have also demonstrated the temperature-dependent MLD growth of polyimides using pyromellitic dianhydride (PMDA) and various diamines[196] and the MLD of polyurethane using 1,4-phenylene diisocyanate and 2-butyne-1,4-diol.[197] Other recent investigations have demonstrated the area-selective patterning[198] and orientation control[199] of polyazomethine MLD. Polyazomethine is a conjugated polymer grown using terephthalaldehyde and p-phenylenediamine as the MLD reactants.[199,200]

12.2. Hybrid Organic—Inorganic Polymers

In addition to organic polymers, the MLD of hybrid organic—inorganic polymers has been demonstrated using inorganic precursors from ALD with various organic precursors.[193] One class of hybrid organic—inorganic MLD polymer is the "alucones".[201] These hybrid polymers result from using aluminum alkyl precursors such as trimethylaluminum (TMA) and various organic diols such as ethylene glycol (EG).[201] The surface reactions during alucone MLD can be written as[201]

(A) $MR^* + HOR'OH \rightarrow MOR'OH^* + RH$

$\qquad\qquad\qquad\qquad\qquad\qquad\qquad\qquad$ (24)

(B) $R'OH^* + MR_x \rightarrow R'OMR_{x-1}^* + RH$ (25)

where the metal alkyl molecule is MR_x and the diol is $HOR'OH$. A schematic illustrating the MLD of alucone using TMA and EG is shown in Figure 23.[201]

The MLD of alucones is very robust and yields very efficient and linear growth. Alucone MLD using TMA and EG has been investigated using a quartz crystal microbalance (QCM) and in situ FTIR investigations.[201] The growth rate per cycle was observed to decrease from 4.0 Å per AB cycle at 85 °C to 0.4 Å per AB cycle at 175 °C.[201] In addition to alucone MLD, other studies have explored the growth of hybrid zinc/organic polymers that can be referred to as "zincones".[202,203] Zincone MLD is also very efficient and leads to linear growth.[202,203] A wide range of various hybrid organic—inorganic polymers are possible, as described by a recent patent application.[204]

There are a number of difficulties for MLD relative to ALD.[193] MLD usually has problems with the low vapor pressure of the organic precursors. In addition, organic precursors are also thermally sensitive and will decompose at higher temperatures. The low vapor pressure of the organic precursors cannot always be solved by raising the temperature of the precursor source. The resulting MLD polymer films are also fairly porous. Consequently, the ALD and MLD reactants can diffuse into the MLD films. This
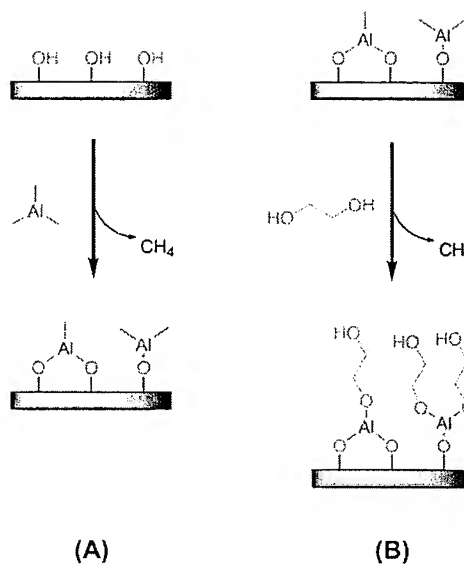

Figure 23. Illustration of surface chemistry for two-step alucone MLD using TMA and EG as reactants. (Reprinted with permission from ref 201. Copyright 2008 American Chemical Society.)

precursor diffusion leads to an additional growth mechanism for MLD films. The MLD films can grow either by self-limiting surface reactions or by a type of CVD reaction between reactants that have diffused into the MLD film. Despite these difficulties, MLD film growth has displayed self-limiting and linear growth that is very similar to ALD.

Another difficulty during MLD is that the homobifunctional organic precursors typically employed during MLD can react more than once with the chemical groups on the surface.[193,194] These "double" reactions lead to a loss of active surface sites and the reduction of the MLD growth per cycle. To avoid these "double" reactions with homobifunctional
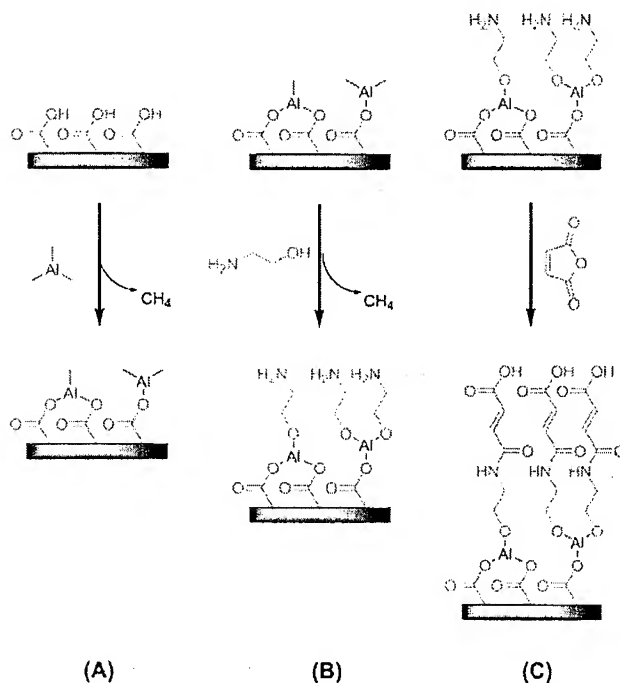

Figure 24. Illustration of surface chemistry for three-step alucone MLD with TMA, EA, and MA as reactants. (Reprinted with permission from ref 193. Copyright 2009 American Chemical Society.)

organic precursors, alternative organic precursors can be employed such as heterobifunctional organic precursors and ring-opening reactions.[193,194] This new strategy is developing and has been demonstrated by the MLD of the ABC alucones using three sequential surface reactions with TMA, ethanolamine (EA), and maleic anhydride (MA) as the reactants, as displayed in Figure 24.[193] Many other combinations of reactants are possible, and the MLD of polymer films is expected to develop rapidly in the coming years.

13. Additional Topics

There are various other topics that could have been included in this overview of ALD. The field of ALD is growing rapidly and expanding into many applications outside of semiconductor processing. This overview has attempted to capture many of the main themes and applications of ALD. Everything could not be included because of space and the need to establish priorities. However, there are several additional topics that should be mentioned which are given below.

13.1. Nonideal ALD Behavior and the ALD Window

The ideal model for ALD displayed by Al_2O_3 ALD may not be achieved by other ALD systems. Some ALD systems are not self-limiting because the surface species may decompose and allow additional adsorption. This decomposition may occur even at the minimum temperatures required for the surface reactions. Other ALD systems may be based on surface reactions that never reach completion. These reactions may proceed to some percentage of completion and then stop. These reactions will display self-limiting growth but with large amounts of impurities remaining in the films.

The processing temperature range for ALD or the so-called "ALD window" is the region of nearly ideal ALD behavior between the nonideal regions as shown in Figure 25.[12] At lower temperatures, the reactants could condense on the surface or the surface reactions may not have enough thermal energy to reach completion. At higher temperature, the surface species could decompose and allow additional reactant adsorption. This behavior is similar to CVD by unimolecular decomposition. The surface species needed for ALD could also desorb from the surface at higher temperatures and be unavailable for additional surface reactions. This desorption would lead to the decrease of the ALD growth per cycle at higher temperatures. This behavior is observed for Al_2O_3 ALD.[14,20,32]

One system that displays dramatic nonideal ALD behavior is TiN ALD using tetradimethylaminotitanium (TDMAT)
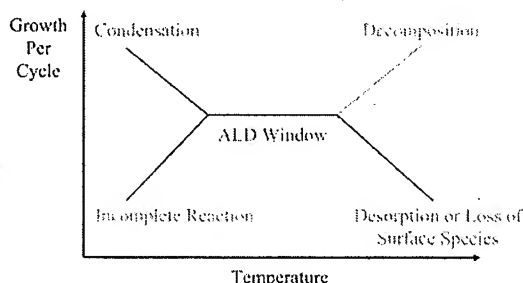

Figure 25. Schematic of possible behavior for the ALD growth per cycle versus temperature showing the "ALD" window. (Adapted from ref 12.)

and NH_3. Although this ALD system was initially presented as a working ALD process,[205,206] additional studies revealed that the surface reactions did not reach completion, impurities were left in the resulting films, and the films had significant porosity that led to their easy oxidation.[64] TiN ALD using TDMAT and NH_3 has no "ALD window" where the ALD process is reasonable. In contrast, TiN ALD using $TiCl_4$ and NH_3 is a well-defined ALD process that occurs at higher temperatures and produces HCl as a reaction product.[207]

13.2. Area-Selective ALD for Spatial Patterning

ALD has exquisite control over the thickness of the deposited thin film. However, lateral patterning of ALD is needed for fabrication of three-dimensional devices. Lateral patterning can be achieved using photoresist and photolithography methods that are similar to conventional semiconductor processing. Self-assembled monolayers can also be used as a masking layer. In addition, direct write methods such as electron beam writing can be used to remove the masking layer and allow for ALD on the selected surface areas.

One example of area-selective ALD is the lateral patterning of HfO_2 ALD on Si(100).[208,209] Area-selective blocking chemistry was observed using siloxane attachment to SiO_2 surfaces. In this demonstration, photolithography was initially used to produce a patterned SiO_2 surface on Si(100). The areas not covered with SiO_2 remained as the hydrogen-passivated H–Si(100) surface. Subsequently, the surface was exposed to octadecyltrichlorosilane (ODTS) and a self-assembled siloxane monolayer formed on the SiO_2 surface. The HfO_2 ALD was then performed and the HfO_2 ALD layer grew only on the H–Si(100) areas of the surface. Scanning Auger analysis revealed the laterally patterned HfO_2 ALD surface.[209]

Area-selective ALD has also been demonstrated for other ALD systems. Lateral patterning of Ru ALD has been achieved using patterned octadecyltrichorosilane monolayers.[210] Spatial selectivity has also been demonstrated for Pt ALD using a monolayer resist of 1-octadecene adsorbed to the hydride-terminated silicon regions of a Si/SiO_2 substrate.[211] In addition, the selective deposition of TiO_2 ALD has been reported using polymer masking layers.[212–214] HfO_2 ALD has also been patterned using the pores of S-layer proteins as a template.[215] As mentioned earlier, area-selective Cu ALD was demonstrated on platinum seeded substrates.[95] The lateral patterning of a polyazomethine MLD film was also achieved by selective MLD on the hydrophilic regions of a hydrophobic/hydrophilic surface.[198]

13.3. Atmospheric Pressure ALD

The cost of ALD is largely tied to the cost of the reactants and the equipment. Most ALD is performed with vacuum pumps that act to move the reactants and products through the reactor and maintain a clean environment in the reactor. These vacuum pumps are not needed if ALD could be performed at pressures greater than atmospheric pressure where the reactant and product gases could be pushed through the reactor. Except for the greater gas usage and the lower gas diffusion rates at higher pressure, atmospheric pressure ALD should be viable and has been demonstrated for ZrO_2 ALD using $ZrCl_4$ and O_2[216] and for HfO_2 ALD using $HfCl_4$ and O_2.[217]
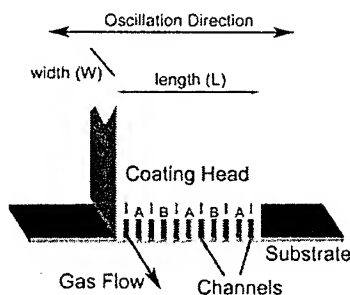
Figure 26. Schematic of an ALD coating head showing the gas channels and gas flow. A is the oxidizing reactant, B is the metal reactant, and I is the inert gas. (Reprinted with permission from ref 218. Copyright 2008 American Institute of Physics.)

A recent design for spatially selective atmospheric ALD has been presented based on a coating head that is positioned next to a substrate.[218] The ALD reactants are delivered through channels in the coating head.[218] The channels are separated by inert gas flow to prevent the gas phase reactions of the precursors. The arrangement of neighboring channels is I/A/I/B..., where I is the inert gas and A and B are the ALD reactants. A schematic illustrating this arrangement of neighboring channels in the coating head over a substrate is shown in Figure 26.[218] Additional pumping channels could also be inserted between the neighboring channels to remove the gases from the region between the coating head and the substrate.

If the coating head is stationary on the substrate, then there is no ALD because each area of the substrate under the coating head is only exposed to one of the two ALD reactants. If the coating head moves relative to the substrate, then the substrate will experience exposure to both ALD reactants. The coating head could either move in a linear fashion or move back and forth to overlap the adjacent surface areas and achieve ALD. This design has been demonstrated for Al_2O_3 ALD and ZnO ALD.[218] Similar saturation behavior was observed for Al_2O_3 ALD compared with conventional Al_2O_3 ALD. The Al_2O_3 ALD films also had excellent insulating properties and have been used to fabricate ZnO thin film transistors.[219]

13.4. ALD on Biological Templates

The complexity of biological structures can be replicated by coating ALD films on biological templates. Low temperature ALD facilitates using the nanostructures of nature as a mold.[24] One of the first demonstrations of ALD on biological templates was TiO_2 ALD and Al_2O_3 ALD on the tobacco mosaic virus (TMV) and ferritin.[122] TiO_2 ALD on the TMV formed extremely small porous structures that replicated the outer protein sheath of the virus. The virus was then decomposed at higher temperatures or removed by a chemical reaction to yield very small nanotubes.[122] Al_2O_3 ALD and TiO_2 ALD on ferritin also demonstrated that ALD can decorate assemblies of biological macromolecules.[122]

Al_2O_3 ALD has also been employed to replicate butterfly wings.[220] SEM images and optical reflectivities revealed that the Al_2O_3 ALD coating was a nearly perfect duplicate of the butterfly wing. This biological duplicate served as a photonic bandgap structure. Additional studies have explored the optical properties of these biological replicas versus TiO_2 ALD thickness.[221] The TiO_2 ALD films acted as Fabry–Perot etalons with reflectivity that was precisely controlled by the TiO_2 ALD film thickness.

13.5. Other Emerging Areas

The main virtues of ALD are its precise thickness control and its extreme conformality on high aspect ratio structures. These virtues have been recognized by additional emerging application areas. A recent review has highlighted the applications of ALD to nanofabrication and emerging nanodevices.[23] One example is ALD for the deposition of conformal coatings with precise thicknesses to form nanowire FETs.[222] ALD may also be useful in fabricating high sensitivity sensors. These sensors can be based on high surface area substrates that are coated with the appropriate sensing film deposited using ALD.[26,223]

ALD may also be useful in the fabrication of nanophotovoltaic (nano-PV) light-harvesting devices. These nano-PV devices are dependent on the close proximity of electron and hole collecting materials. ALD can infiltrate various semiconducting and conducting materials to fabricate efficient structures.[224,225] In addition, biological implants usually require coatings to ensure that they are biocompatible. Some of these implants have high aspect ratios such as coronary artery stents. Various ALD materials such as Al_2O_3 ALD have been explored as biocompatible coatings.[226]

14. Conclusions

Because of continued device miniaturization, control of thin film growth is needed at the atomic level to fabricate semiconductor and other nanoscale devices. To meet these demands, atomic layer deposition (ALD) techniques have been developed for the growth of ultrathin and conformal films. ALD is a gas phase method based on sequential, self-limiting surface reactions. ALD can deposit very conformal and ultrathin films on substrates with very high aspect ratios. This overview has presented a brief introduction to ALD and its history. Subsequently, Al_2O_3 ALD was introduced as a model ALD system. The overview then described other examples of thermal ALD and radical-enhanced ALD for the deposition of single-element metals and semiconductors. Following a brief review of ALD reactor design, the thermal chemistry for metal ALD was also reviewed using fluorosilane elimination chemistry with metal fluorides, combustion chemistry with organometallic precursors, or hydrogen reduction chemistry.

The overview then considered the topic of nucleation and growth during ALD that is extremely important for the ALD of high-k gate oxides on H–Si(100). Many topics were then reviewed, including low temperature ALD using Al_2O_3 ALD or catalytic SiO_2 ALD. The overview considered ALD on polymers and the mechanism for ALD on polymers. Molecular layer deposition (MLD) of polymers was also discussed as an analogous process to ALD that can deposit organic and hybrid organic–inorganic polymers. The overview then considered ALD on particles and ALD on nanotubes and nanorods. ALD on high aspect ratio structures was then considered including an examination of the times required for conformal growth on high aspect ratio structures. The ALD of nanolaminates and nanocomposites was discussed, including applications of the nanolaminates as thermal barrier coatings and Bragg X-ray mirrors. The overview then concluded with some additional topics such as area-selective ALD and atmospheric pressure ALD.

The future prospects for ALD are very promising. Various materials can be deposited using ALD techniques. The availability of many commercial ALD reactors continues to

make ALD accessible for many workers outside of the thin film growth community. ALD is firmly established on the *International Technology Roadmap for Semiconductors*. ALD should also play an integral role in new paradigms for electronic materials. The number of applications for ALD also continues to grow outside of the semiconductor arena. The future should see ALD continue to expand into new areas and find additional applications that benefit from its precise thickness control and conformality.

15. Acknowledgments

This overview of ALD is based in part on a one-day short course that SMG teaches for the AVS. The author thanks the AVS for the opportunity to develop and teach this course. In addition, the author acknowledges the students who have taken the course for their feedback and interests in various applications of ALD. SMG also thanks the National Science Foundation and the Air Force Office of Scientific Research for their research support on various aspects of ALD. This review would also not have been possible without the work of the many researchers in the ALD field. The author also thanks the past and former members of his research group for their contributions to ALD.

16. References

(1) *International Technology Roadmap for Semiconductors*, 2007 Edition, http://www.itrs.net/.
(2) Sneh, O.; Clark-Phelps, R. B.; Londergan, A. R.; Winkler, J.; Seidel, T. E. *Thin Solid Films* 2002, 402, 248.
(3) Paranjpe, A.; Gopinath, S.; Omstead, T.; Bubber, R. *J. Electrochem. Soc.* 2001, 148, G465.
(4) Chatham, H. *Surf. Coat. Technol.* 1996, 78, 1.
(5) George, S. M.; Ott, A. W.; Klaus, J. W. *J. Phys. Chem.* 1996, 100, 13121.
(6) Fabreguette, F. H.; Wind, R. A.; George, S. M. *Appl. Phys. Lett.* 2006, 88, 013116.
(7) Groner, M. D.; Elam, J. W.; Fabreguette, F. H.; George, S. M. *Thin Solid Films* 2002, 413, 186.
(8) Goodman, C. H. L.; Pessa, M. V. *J. Appl. Phys.* 1986, 60, R65.
(9) Niinisto, L. *Curr. Opin. Solid State Mater. Sci.* 1998, 3, 147.
(10) Niinisto, L.; Leskela, M. *Thin Solid Films* 1993, 225, 130.
(11) Suntola, T. *Thin Solid Films* 1992, 216, 84.
(12) Suntola, T. Atomic Layer Epitaxy. In *Handbook of Crystal Growth, Vol. 3. Part B: Growth Mechanisms and Dynamics*; Hurle, D. T. J., Ed.; Elsevier: Amsterdam, 1994; Chapter 14.
(13) Suntola, T.; Hyvarinen, J. *Annu. Rev. Mater. Sci.* 1985, 15, 177.
(14) Ott, A. W.; Klaus, J. W.; Johnson, J. M.; George, S. M. *Thin Solid Films* 1997, 292, 135.
(15) Nishizawa, J.; Abe, H.; Kurabayashi, T. *J. Electrochem. Soc.* 1985, 132, 1197.
(16) Suntola, T. Thirty Years of ALD. An Invited Talk at *AVS Topical Conference on Atomic Layer Deposition (ALD2004)*; University of Helsinki: Helsinki, Finland, August 16. 2004.
(17) Suntola, T.; Antson, J. Method for Producing Compound Thin Films. U.S. Patent #4,058,430. Issued Nov. 25, 1977.
(18) Ahonen, M.; Pessa, M.; Suntola, T. *Thin Solid Films* 1980, 65, 301.
(19) Leskela, M.; Ritala, M. *Thin Solid Films* 2002, 409, 138.
(20) Puurunen, R. L. *J. Appl. Phys.* 2005, 97, 121301.
(21) Ritala, M.; Leskela, M. Atomic Layer Deposition. *Handbook of Thin Film Materials*; San Diego, CA. 2001.
(22) Kim, H. *J. Vac. Sci. Technol. B* 2003, 21, 2231.
(23) Kim, H.; Lee, H. B. R.; Maeng, W. J. *Thin Solid Films* 2009, 517, 2563.
(24) Knez, M.; Niesch, K.; Niinisto, L. *Adv. Mater.* 2007, 19, 3425.
(25) Leskela, M.; Ritala, M. *Angew. Chem., Int. Ed.* 2003, 42, 5548.
(26) Niinisto, L.; Paivasaari, J.; Niinisto, J.; Putkonen, M.; Nieminen, M. *Phys. Status Solidi A* 2004, 201, 1443.
(27) Ritala, M.; Leskela, M. *Nanotechnology* 1999, 10, 19.
(28) Higashi, G. S.; Fleming, C. G. *Appl. Phys. Lett.* 1989, 55, 1963.
(29) Soto, C.; Tysoe, W. T. *J. Vac. Sci. Technol. A* 1991, 9, 2686.
(30) Goldstein, D. N.; McCormick, J. A.; George, S. M. *J. Phys. Chem. C* 2008, 112, 19530.
(31) Kim, J. B.; Kwon, D. R.; Chakrabarti, K.; Lee, C.; Oh, K. Y.; Lee, J. H. *J. Appl. Phys.* 2002, 92, 6739.

(32) Dillon, A. C.; Ott, A. W.; Way, J. D.; George, S. M. *Surf. Sci.* 1995, 322, 230.
(33) *HSC Chemistry*, 5.11 edition: Outokumpu Research Oy: Pori, Finland. Values are given at 0 °C.
(34) Widjaja, Y.; Musgrave, C. B. *Appl. Phys. Lett.* 2002, 80, 3304.
(35) Ferguson, J. D.; Weimer, A. W.; George, S. M. *Thin Solid Films* 2000, 371, 95.
(36) Ferguson, J. D.; Weimer, A. W.; George, S. M. *Chem. Mater.* 2004, 16, 5602.
(37) Juppo, M.; Rahtu, A.; Ritala, M.; Leskela. M. *Langmuir* 2000, 16, 4034.
(38) Rahtu, A.; Alaranta, T.; Ritala, M. *Langmuir* 2001, 17, 6506.
(39) Elam, J. W.; Groner, M. D.; George, S. M. *Rev. Sci. Instrum.* 2002, 73, 2981.
(40) Hakim, L. F.; Blackson, J.; George, S. M.; Weimer, A. W. *Chem. Vap. Deposition* 2005, 11, 420.
(41) McCormick, J. A.; Cloutier, B. L.; Weimer, A. W.; George, S. M. *J. Vac. Sci. Technol. A* 2007, 25, 67.
(42) Ritala, M.; Leskela, M.; Dekker, J. P.; Mutsaers, C.; Soininen, P. J.; Skarp, J. *Chem. Vap. Deposition* 1999, 5, 7.
(43) Groner, M. D.; Fabreguette, F. H.; Elam, J. W.; George, S. M. *Chem. Mater.* 2004, 16, 639.
(44) Huang, M. L.; Chang, Y. C.; Chang, C. H.; Lee, Y. J.; Chang, P.; Kwo, J.; Wu, T. B.; Hong, M. *Appl. Phys. Lett.* 2005, 87, 252104.
(45) Xuan, Y.; Lin, H. C.; Ye, P. D.; Wilk, G. D. *Appl. Phys. Lett.* 2006, 88, 263518.
(46) Ye, P. D.; Wilk, G. D.; Kwo, J.; Yang, B.; Gossmann, H. J. L.; Frei, M.; Chu, S. N. G.; Mannaerts, J. P.; Sergent, M.; Hong, M.; Ng, K. K.; Bude, J. *IEEE Electron Device Lett.* 2003, 24, 209.
(47) Ritala, M.; Leskela, M.; Nykanen, E.; Soininen, P.; Niinisto, L. *Thin Solid Films* 1993, 225, 288.
(48) Yamada, A.; Sang, B. S.; Konagai, M. *Appl. Surf. Sci.* 1997, 112, 216.
(49) Yousfi, E. B.; Fouache, J.; Lincot, D. *Appl. Surf. Sci.* 2000, 153, 223.
(50) Rossnagel, S. M.; Sherman, A.; Turner, F. *J. Vac. Sci. Technol. B* 2000, 18, 2016.
(51) Kim, H.; Cabral, C.; Lavoie, C.; Rossnagel, S. M. *J. Vac. Sci. Technol. B* 2002, 20, 1321.
(52) Grubbs, R. K.; George, S. M. *J. Vac. Sci. Technol. A* 2006, 24, 486.
(53) Coon, P. A.; Gupta, P.; Wise, M. L.; George, S. M. *J. Vac. Sci. Technol. A* 1992, 10, 324.
(54) Koehler, B. G.; Mak, C. H.; Arthur, D. A.; Coon, P. A.; George, S. M. *J. Chem. Phys.* 1988, 89, 1709.
(55) Gupta, P.; Coon, P. A.; Koehler, B. G.; George, S. M. *Surf. Sci.* 1991, 249, 92.
(56) Hasunuma, E.; Sugahara, S.; Hoshino, S.; Imai, S.; Ikeda, K.; Matsumura, M. *J. Vac. Sci. Technol. A* 1998, 16, 679.
(57) Imai, S.; Iizuka, T.; Sugiura, O.; Matsumura, M. *Thin Solid Films* 1993, 225, 168.
(58) Sugahara, S.; Kadoshima, M.; Kitamura, T.; Imai, S.; Matsumura, M. *Appl. Surf. Sci.* 1995, 90, 349.
(59) Sugahara, S.; Uchida, Y.; Kitamura, T.; Nagai, T.; Matsuyama, M.; Hattori, T.; Matsumura, M. *Jpn. J. Appl. Phys. Part 1* 1997, 36, 1609.
(60) Heil, S. B. S.; Kudlacek, P.; Langereis, E.; Engeln, R.; van de Sanden, M. C. M.; Kessels, W. M. M. *Appl. Phys. Lett.* 2006, 89, 131505.
(61) Langereis, E.; Creatore, M.; Heil, S. B. S.; Van de Sanden, M. C. M.; Kessels, W. M. M. *Appl. Phys. Lett.* 2006. 89, 081915.
(62) Lim, J. W.; Yun, S. J. *Electrochem. Solid-State Lett.* 2004, 7, F45.
(63) Hoex, B.; Heil, S. B. S.; Langereis, E.; van de Sanden, M. C. M.; Kessels, W. M. M. *Appl. Phys. Lett.* 2006, 89, 042112.
(64) Elam, J. W.; Schuisky, M.; Ferguson, J. D.; George, S. M. *Thin Solid Films* 2003, 436, 145.
(65) Kwon, O. K.; Kwon, S. H.; Park, H. S.; Kang, S. W. *J. Electrochem. Soc.* 2004, 151, C753.
(66) Rayner, G. B.; George, S. M. *J. Vac. Sci. Technol. A* 2009, 27, 716.
(67) Park, J. S.; Lee, M. J.; Lee, C. S.; Kang, S. W. *Electrochem. Solid-State Lett.* 2001, 4, C17.
(68) Park, J. S.; Park, H. S.; Kang, S. W. *J. Electrochem. Soc.* 2002, 149, C28.
(69) Van, T. T.; Chang, J. P. *Surf. Sci.* 2005, 596, 1.
(70) Knoops, H. C. M.; Mackus, A. J. M.; Donders, M. E.; van de Sanden, M. C. M.; Notten, P. H. L.; Kessels, W. M. M. *Electrochem. Solid-State Lett.* 2009, 12, G34.
(71) Kwon, O. K.; Kwon, S. H.; Park, H. S.; Kang, S. W. *Electrochem. Solid-State Lett.* 2004, 7, C46.
(72) Suntola, T.; Paakala, A. J.; Lindfors, S. G. *"Apparatus for Performing Growth of Compound Thin Films"*, U.S. Patent #4,389,973. Issued Jun. 28, 1983.
(73) Suntola, T. *Thin Solid Films* 1993, 225, 96.
(74) Sneh, O.; Wise, M. L.; Ott, A. W.; Okada, L. A.; George, S. M. *Surf. Sci.* 1995, 334, 135.

(75) Skarp, J. I.; Soininen, P. J.; Soininen, P. T. *Appl. Surf. Sci.* **1997**, *112*, 251.

(76) Dushman, S. *Scientific Foundations of Vacuum Technique*, 2nd ed.; Revised by Lafferty, J. M., Editor; John Wiley & Sons: New York, 1962.

(77) Roth, A. *Vacuum Technology*, 2nd. Revised Edition; North-Holland: Amsterdam, 1986.

(78) Sneh, O. ALD Apparatus and Method. U.S. Patent #6,911,092, Issued June 28, 2005.

(79) Sneh, O. Unpublished Information from Sundew Technologies, LLC, Broomfield, CO.

(80) Heil, S. B. S.; van Hemmen, J. L.; Hodson, C. J.; Singh, N.; Klootwijk, J. H.; Roozeboom, F.; de Sanden, M.; Kessels, W. M. M. *J. Vac. Sci. Technol. A* **2007**, *25*, 1357.

(81) Klaus, J. W.; Ferro, S. J.; George, S. M. *Thin Solid Films* **2000**, *360*, 145.

(82) Grubbs, R. K.; Steinmetz, N. J.; George, S. M. *J. Vac. Sci. Technol. B* **2004**, *22*, 1811.

(83) Fabreguette, F. H.; Sechrist, Z. A.; Elam, J. W.; George, S. M. *Thin Solid Films* **2005**, *488*, 103.

(84) Elam, J. W.; Nelson, C. E.; Grubbs, R. K.; George, S. M. *Surf. Sci.* **2001**, *479*, 121.

(85) Luoh, T.; Su, C. T.; Yang, T. H.; Chen, K. C.; Lu, C. Y. *Microelectron. Eng.* **2008**, *85*, 1739.

(86) Aaltonen, T.; Alen, P.; Ritala, M.; Leskela, M. *Chem. Vap. Deposition* **2003**, *9*, 45.

(87) Aaltonen, T.; Ritala, M.; Sajavaara, T.; Keinonen, J.; Leskela, M. *Chem. Mater.* **2003**, *15*, 1924.

(88) Aaltonen, T.; Rahtu, A.; Ritala, M.; Leskela, M. *Electrochem. Solid-State Lett.* **2003**, *6*, C130.

(89) Aaltonen, T.; Ritala, M.; Sammelselg, V.; Leskela, M. *J. Electrochem. Soc.* **2004**, *151*, G489.

(90) Aaltonen, T.; Ritala, M.; Leskela, M. *Electrochem. Solid-State Lett.* **2005**, *8*, C99.

(91) Kim, H.; Shimogaki, Y. *J. Electrochem. Soc.* **2007**, *154*, G13.

(92) Kim, H.; Kojima, Y.; Sato, H.; Yoshii, N.; Hosaka, S.; Shimogaki, Y. *Jpn. J. Appl. Phys. Part 2* **2006**, *45*, L233.

(93) Martensson, P.; Carlsson, J. O. *Chem. Vap. Deposition* **1997**, *3*, 45.

(94) Lampeonnerud, C.; Jansson, U.; Harsta, A.; Carlsson, J. O. *J. Cryst. Growth* **1992**, *121*, 223.

(95) Martensson, P.; Carlsson, J. O. *J. Electrochem. Soc.* **1998**, *145*, 2926.

(96) Huo, J. S.; Solanki, R.; McAndrew, J. *J. Mater. Res.* **2002**, *17*, 2394.

(97) Solanki, R.; Pathangey, B. *Electrochem. Solid-State Lett.* **2000**, *3*, 479.

(98) Elam, J. W.; Zinovev, A.; Han, C. Y.; Wang, H. H.; Welp, U.; Hryn, J. N.; Pellin, M. J. *Thin Solid Films* **2006**, *515*, 1664.

(99) Utriainen, M.; Kroger-Laukkanen, M.; Johansson, L. S.; Niinisto, L. *Appl. Surf. Sci.* **2000**, *157*, 151.

(100) Chae, J.; Park, H. S.; Kang, S. W. *Electrochem. Solid-State Lett.* **2002**, *5*, C64.

(101) Lim, B. S.; Rahtu, A.; Gordon, R. G. *Nat. Mater.* **2003**, *2*, 749.

(102) Argile, C.; Rhead, G. E. *Surf. Sci. Rep.* **1989**, *10*, 277.

(103) Besling, W. F. A.; Young, E.; Conard, T.; Zhao, C.; Carter, R.; Vandervorst, W.; Caymax, M.; De Gendt, S.; Heyns, M.; Maes, J.; Tuominen, M.; Haukka, S. *J. Non-Cryst. Solids* **2002**, *303*, 123.

(104) Copel, M.; Gribelyuk, M.; Gusev, E. *Appl. Phys. Lett.* **2000**, *76*, 436.

(105) Green, M. L.; Ho, M. Y.; Busch, B.; Wilk, G. D.; Sorsch, T.; Conard, T.; Brijs, B.; Vandervorst, W.; Raisanen, P. I.; Muller, D.; Bude, M.; Grazul, J. *J. Appl. Phys.* **2002**, *92*, 7168.

(106) Gusev, E. P.; Cabral, C.; Copel, M.; D'Emic, C.; Gribelyuk, M. *Microelectron. Eng.* **2003**, *69*, 145.

(107) Frank, M. M.; Chabal, Y. J.; Wilk, G. D. *Appl. Phys. Lett.* **2003**, *82*, 4758.

(108) Halls, M. D.; Raghavachari, K.; Frank, M. M.; Chabal, Y. J. *Phys. Rev. B* **2003**, *68*, 161302.

(109) Elam, J. W.; Nelson, C. E.; Grubbs, R. K.; George, S. M. *Thin Solid Films* **2001**, *386*, 41.

(110) Grubbs, R. K.; Nelson, C. E.; Steinmetz, N. J.; George, S. M. *Thin Solid Films* **2004**, *467*, 16.

(111) Sechrist, Z. A.; Fabreguette, F. H.; Heintz, O.; Phung, T. M.; Johnson, D. C.; George, S. M. *Chem. Mater.* **2005**, *17*, 3475.

(112) Nilsen, O.; Karlsen, O. B.; Kjekshus, A.; Fjellvag, H. *Thin Solid Films* **2007**, *515*, 4527.

(113) Nilsen, O.; Mohn, C. E.; Kjekshus, A.; Fjellvag, H. *J. Appl. Phys.* **2007**, *102*, 024906.

(114) Wind, R. A.; Fabreguette, F. H.; Sechrist, Z. A.; George, S. M. *J. Appl. Phys.* **2009**, *105*, 074309.

(115) Cavanagh, A. S.; Wilson, C. A.; Weimer, A. W.; George, S. M. *Nanotechnology* **2009**, *20*, 255602.

(116) Farmer, D. B.; Gordon, R. G. *Electrochem. Solid-State Lett.* **2005**, *8*, G89.

(117) Farmer, D. B.; Gordon, R. G. *Nano Lett.* **2006**, *6*, 699.

(118) Xuan, Y.; Wu, Y. Q.; Shen, T.; Qi, M.; Capano, M. A.; Cooper, J. A.; Ye, P. D. *Appl. Phys. Lett.* **2008**, *92*, 013101.

(119) Lee, B. K.; Park, S. Y.; Kim, H. C.; Cho, K.; Vogel, E. M.; Kim, M. J.; Wallace, R. M.; Kim, J. Y. *Appl. Phys. Lett.* **2008**, *92*, 203102.

(120) Wang, X. R.; Tabakman, S. M.; Dai, H. J. *J. Am. Chem. Soc.* **2008**, *130*, 8152.

(121) King, J. S.; Graugnard, E.; Roche, O. M.; Sharp, D. N.; Scrimgeour, J.; Denning, R. G.; Turberfield, A. J.; Summers, C. J. *Adv. Mater.* **2006**, *18*, 1561.

(122) Knez, M.; Kadri, A.; Wege, C.; Gosele, U.; Jeske, H.; Nielsch, K. *Nano Lett.* **2006**, *6*, 1172.

(123) Scharrer, M.; Wu, X.; Yamilov, A.; Cao, H.; Chang, R. P. H. *Appl. Phys. Lett.* **2005**, *86*.

(124) Klaus, J. W.; Ott, A. W.; Johnson, J. M.; George, S. M. *Appl. Phys. Lett.* **1997**, *70*, 1092.

(125) Kang, J. K.; Musgrave, C. B. *J. Appl. Phys.* **2002**, *91*, 3408.

(126) Klaus, J. W.; George, S. M. *Surf. Sci.* **2000**, *447*, 81.

(127) Klaus, J. W.; Sneh, O.; George, S. M. *Science* **1997**, *278*, 1934.

(128) Ferguson, J. D.; Smith, E. R.; Weimer, A. W.; George, S. M. *J. Electrochem. Soc.* **2004**, *151*, G528.

(129) Du, Y.; Du, X.; George, S. M. *J. Phys. Chem. C* **2007**, *111*, 219.

(130) Okamoto, Y. *J. Phys. Chem. B* **1999**, *103*, 11074.

(131) Du, Y.; Du, X.; George, S. M. *Thin Solid Films* **2005**, *491*, 43.

(132) Parks, G. A. *Chem. Rev.* **1965**, *65*, 177.

(133) Jung, S. H.; Kang, S. W. *Jpn. J. Appl. Phys. Part 1* **2001**, *40*, 3147.

(134) Wilson, C. A.; Grubbs, R. K.; George, S. M. *Chem. Mater.* **2005**, *17*, 5625.

(135) Carcia, P. F.; McLean, R. S.; Reilly, M. H.; Groner, M. D.; George, S. M. *Appl. Phys. Lett.* **2006**, *89*, 031915.

(136) Groner, M. D.; George, S. M.; McLean, R. S.; Carcia, P. F. *Appl. Phys. Lett.* **2006**, *88*, 051907.

(137) Carcia, P. F.; McLean, R. S.; Groner, M. D.; Dameron, A. A.; George, S. M. *J. Appl. Phys.* **2009**, *106*, 023533.

(138) Dameron, A. A.; Davidson, S. D.; Burton, B. B.; Carcia, P. F.; McLean, R. S.; George, S. M. *J. Phys. Chem. C* **2008**, *112*, 4573.

(139) Meyer, J.; Gorrn, P.; Bertram, F.; Hamwi, S.; Winkler, T.; Johannes, H. H.; Weimann, T.; Hinze, P.; Riedl, T.; Kowalsky, W. *Adv. Mater.* **2009**, *21*, 1845.

(140) Ghosh, A. P.; Gerenser, L. J.; Jarman, C. M.; Fornalik, J. E. *Appl. Phys. Lett.* **2005**, *86*, 223503.

(141) Park, S. H. K.; Oh, J.; Hwang, C. S.; Lee, J. I.; Yang, Y. S.; Chu, H. Y. *Electrochem. Solid-State Lett.* **2005**, *8*, H21.

(142) Potscavage, W. J.; Yoo, S.; Domercq, B.; Kippelen, B. *Appl. Phys. Lett.* **2007**, *90*, 253511.

(143) Ferrari, S.; Perissinotti, F.; Peron, E.; Fumagalli, L.; Natali, D.; Sampietro, M. *Org. Electron.* **2007**, *8*, 407.

(144) Fumagalli, L.; Natali, D.; Sampietro, M.; Peron, E.; Perissinotti, F.; Tallarida, G.; Ferrari, S. *Org. Electron.* **2008**, *9*, 198.

(145) Hyde, G. K.; Park, K. J.; Stewart, S. M.; Hinestroza, J. P.; Parsons, G. N. *Langmuir* **2007**, *23*, 9844.

(146) Peng, Q.; Sun, X. Y.; Spagnola, J. C.; Hyde, G. K.; Spontak, R. J.; Parsons, G. N. *Nano Lett.* **2007**, *7*, 719.

(147) Cooper, R.; Upadhyaya, H. P.; Minton, T. K.; Berman, M. R.; Du, X. H.; George, S. M. *Thin Solid Films* **2008**, *516*, 4036.

(148) Wang, X. D.; Graugnard, E.; King, J. S.; Zhong, L. W.; Summers, C. J. *Nano Lett.* **2004**, *4*, 2223.

(149) Shin, H. J.; Jeong, D. K.; Lee, J. G.; Sung, M. M.; Kim, J. Y. *Adv. Mater.* **2004**, *16*, 1197.

(150) Wilson, C. A.; McCormick, J. A.; Cavanagh, A. S.; Goldstein, D. N.; Weimer, A. W.; George, S. M. *Thin Solid Films* **2008**, *516*, 6175.

(151) Mayer, T. M.; Elam, J. W.; George, S. M.; Kotula, P. G.; Goeke, R. S. *Appl. Phys. Lett.* **2003**, *82*, 2883.

(152) Jessensky, O.; Muller, F.; Gosele, U. *Appl. Phys. Lett.* **1998**, *72*, 1173.

(153) Elam, J. W.; Routkevitch, D.; Mardilovich, P. P.; George, S. M. *Chem. Mater.* **2003**, *15*, 3507.

(154) Gordon, R. G.; Hausmann, D.; Kim, E.; Shepard, J. *Chem. Vap. Deposition* **2003**, *9*, 73.

(155) Hoivik, N. D.; Elam, J. W.; Linderman, R. J.; Bright, V. M.; George, S. M.; Lee, Y. C. *Sens. Actuators A* **2003**, *103*, 100.

(156) Herrmann, C. F.; Delrio, F. W.; Bright, V. M.; George, S. M. *J. Micromech. Microeng.* **2005**, *15*, 984.

(157) Scharf, T. W.; Prasad, S. V.; Dugger, M. T.; Kotula, P. G.; Goeke, R. S.; Grubbs, R. K. *Acta Mater.* **2006**, *54*, 4731.

(158) Bachmann, J.; Jing, J.; Knez, M.; Barth, S.; Shen, H.; Mathur, S.; Gosele, U.; Nielsch, K. *J. Am. Chem. Soc.* **2007**, *129*, 9554.

(159) Daub, M.; Knez, M.; Goesele, U.; Nielsch, K. *J. Appl. Phys.* **2007**, *101*, 09J111.

(160) King, J. S.; Neff, C. W.; Summers, C. J.; Park, W.; Blomquist, S.; Forsythe, E.; Morton, D. *Appl. Phys. Lett.* **2003**, *83*, 2566.

(161) Rugge, A.; Park, J. S.; Gordon, R. G.; Tolbert, S. H. *J. Phys. Chem. B* **2005**, *109*, 3764.

(162) Sechrist, Z. A.; Schwartz, B. T.; Lee, J. H.; McCormick, J. A.; Piestun, R.; Park, W.; George, S. M. *Chem. Mater.* **2006**, *18*, 3562.

(163) Biener, J.; Baumann, T. F.; Wang, Y. M.; Nelson, E. J.; Kucheyev, S. O.; Hamza, A. V.; Kemell, M.; Ritala, M.; Leskela, M. *Nanotechnology* **2007**, *18*, 055303.
(164) Elam, J. W.; Libera, J. A.; Pellin, M. J.; Zinovev, A. V.; Greene, J. P.; Nolen, J. A. *Appl. Phys. Lett.* **2006**, *89*, 053124.
(165) Pellin, M. J.; Stair, P. C.; Xiong, G.; Elam, J. W.; Birrell, J.; Curtiss, L.; George, S. M.; Han, C. Y.; Iton, L.; Kung, H.; Kung, M.; Wang, H. H. *Catal. Lett.* **2005**, *102*, 127.
(166) Hakim, L. F.; Vaughn, C. L.; Dunsheath, H. J.; Carney, C. S.; Liang, X.; Li, P.; Weimer, A. W. *Nanotechnology* **2007**, *18*, 345603.
(167) Weimer, M. A.; Hakim, L. F.; King, D. M.; Liang, X.; Weimer, A. W.; George, S. M.; Li, P.; Groner, M. D. *Appl. Phys. Lett.* **2008**, *92*, 164101.
(168) King, D. M.; Liang, X. H.; Carney, C. S.; Hakim, L. F.; Li, P.; Weimer, A. W. *Adv. Funct. Mater.* **2008**, *18*, 607.
(169) Hakim, L. F.; King, D. M.; Zhou, Y.; Gump, C. J.; George, S. M.; Weimer, A. W. *Adv. Funct. Mater.* **2007**, *17*, 3175.
(170) Ferguson, J. D.; Buechler, K. J.; Weimer, A. W.; George, S. M. *Powder Technol.* **2005**, *156*, 154.
(171) Wank, J. R.; George, S. M.; Weimer, A. W. *Powder Technol.* **2001**, *121*, 195.
(172) Wank, J. R.; George, S. M.; Weimer, A. W. *Powder Technol.* **2004**, *142*, 59.
(173) Wank, J. R.; George, S. M.; Weimer, A. W. *J. Am. Ceram. Soc.* **2004**, *87*, 762.
(174) McCormick, J. A.; Rice, K. P.; Paul, D. F.; Weimer, A. W.; George, S. M. *Chem. Vap. Deposition* **2007**, *13*, 491.
(175) Lee, J. S.; Min, B.; Cho, K.; Kim, S.; Park, J.; Lee, Y. T.; Kim, N. S.; Lee, M. S.; Park, S. O.; Moon, J. T. *J. Cryst. Growth* **2003**, *254*, 443.
(176) Min, B.; Lee, J. S.; Hwang, J. W.; Keem, K. H.; Kang, M. I.; Cho, K.; Sung, M. Y.; Kim, S.; Lee, M. S.; Park, S. O.; Moon, J. T. *J. Cryst. Growth* **2003**, *252*, 565.
(177) Herrmann, C. F.; Fabreguette, F. H.; Finch, D. S.; Geiss, R.; George, S. M. *Appl. Phys. Lett.* **2005**, *87*, 123110.
(178) Kukli, K.; Ihanus, J.; Ritala, M.; Leskela, M. *J. Electrochem. Soc.* **1997**, *144*, 300.
(179) Zaitsu, S.; Jitsuno, T.; Nakatsuka, M.; Yamanaka, T.; Motokoshi, S. *Appl. Phys. Lett.* **2002**, *80*, 2442.
(180) El-Sayed, M. A. *Acc. Chem. Res.* **2001**, *34*, 257.
(181) Costescu, R. M.; Cahill, D. G.; Fabreguette, F. H.; Sechrist, Z. A.; George, S. M. *Science* **2004**, *303*, 989.
(182) Swartz, E. T.; Pohl, R. O. *Rev. Mod. Phys.* **1989**, *61*, 605.
(183) Kumagai, H.; Toyoda, K.; Kobayashi, K.; Obara, M.; Iimura, Y. *Appl. Phys. Lett.* **1997**, *70*, 2338.
(184) Ishii, M.; Iwai, S.; Kawata, H.; Ueki, T.; Aoyagi, Y. *J. Cryst. Growth* **1997**, *180*, 15.
(185) Fabreguette, F. H.; George, S. M. *Thin Solid Films* **2007**, *515*, 7177.
(186) Elam, J. W.; George, S. M. *Chem. Mater.* **2003**, *15*, 1020.
(187) Elam, J. W.; Routkevitch, D.; George, S. M. *J. Electrochem. Soc.* **2003**, *150*, G339.
(188) Herrmann, C. F.; DelRio, F. W.; Miller, D. C.; George, S. M.; Bright, V. M.; Ebel, J. L.; Strawser, R. E.; Cortez, R.; Leedy, K. D. *Sens. Actuators A* **2007**, *135*, 262.
(189) Yoshimura, T.; Tatsuura, S.; Sotoyama, W. *Appl. Phys. Lett.* **1991**, *59*, 482.
(190) Du, Y.; George, S. M. *J. Phys. Chem. C* **2007**, *111*, 8509.
(191) Shao, H. I.; Umemoto, S.; Kikutani, T.; Okui, N. *Polymer* **1997**, *38*, 459.
(192) Kubono, A.; Okui, N. *Prog. Polym. Sci.* **1994**, *19*, 389.
(193) George, S. M.; Yoon, B.; Dameron, A. A. *Acc. Chem. Res.* **2009**, *42*, 498.
(194) Adamcyzk, N. M.; Dameron, A. A.; George, S. M. *Langmuir* **2008**, *24*, 2081.
(195) Kim, A.; Filler, M. A.; Kim, S.; Bent, S. F. *J. Am. Chem. Soc.* **2005**, *127*, 6123.

(196) Putkonen, M.; Harjuoja, J.; Sajavaara, T.; Niinisto, L. *J. Mater. Chem.* **2006**, *17*, 664.
(197) Lee, J. S.; Lee, Y. J.; Tae, E. L.; Park, Y. S.; Yoon, K. B. *Science* **2003**, *301*, 818.
(198) Yoshimura, T.; Terasawa, N.; Kazama, H.; Naito, Y.; Suzuki, Y.; Asama, K. *Thin Solid Films* **2006**, *497*, 182.
(199) Yoshimura, T.; Ito, S.; Nakayama, T.; Matsumoto, K. *Appl. Phys. Lett.* **2007**, *91*, 033103.
(200) Yoshimura, T.; Tatsuura, S.; Sotoyama, W.; Matsuura, A.; Hayano, T. *Appl. Phys. Lett.* **1992**, *60*, 268.
(201) Dameron, A. A.; Saghete, D.; Burton, B. B.; Davidson, S. D.; Cavanagh, A. S.; Bertand, J. A.; George, S. M. *Chem. Mater.* **2008**, *20*, 3315.
(202) Peng, Q.; Gong, B.; VanGundy, R. M.; Parsons, G. N. *Chem. Mater.* **2009**, *21*, 820.
(203) Yoon, B.; O'Patchen, J. L.; Seghete, D.; Cavanagh, A. S.; George, S. M. *Chem. Vap. Deposition* **2009**, *15*, 112.
(204) Nilsen, O.; Fjellvag, H. Thin Films Prepared with Gas Phase Deposition Technique. Patent Cooperation Treaty (PCT). World Intellectual Property Organization, Publication Number WO 2006/071126 A1, Publication Date July 6, 2006.
(205) Lim, J. W.; Park, H. S.; Kang, S. W. *J. Electrochem. Soc.* **2001**, *148*, C403.
(206) Min, J. S.; Son, Y. W.; Kang, W. G.; Chun, S. S.; Kang, S. W. *Jpn. J. Appl. Phys. Part 1* **1998**, *37*, 4999.
(207) Ritala, M.; Leskela, M.; Rauhala, E.; Haussalo, P. *J. Electrochem. Soc.* **1995**, *142*, 2731.
(208) Chen, R.; Kim, H.; McIntyre, P. C.; Bent, S. F. *Chem. Mater.* **2005**, *17*, 536.
(209) Chen, R.; Kim, H.; McIntyre, P. C.; Porter, D. W.; Bent, S. F. *Appl. Phys. Lett.* **2005**, *86*, 191910.
(210) Park, K. J.; Doub, J. M.; Gougousi, T.; Parsons, G. N. *Appl. Phys. Lett.* **2005**, *86*, 051903.
(211) Chen, R.; Bent, S. F. *Adv. Mater.* **2006**, *18*, 1086.
(212) Park, K. S.; Seo, E. K.; Do, Y. R.; Kim, K.; Sung, M. M. *J. Am. Chem. Soc.* **2006**, *128*, 858.
(213) Sinha, A.; Hess, D. W.; Henderson, C. L. *J. Vac. Sci. Technol. B* **2006**, *24*, 2523.
(214) Sinha, A.; Hess, D. W.; Henderson, C. L. *J. Electrochem. Soc.* **2006**, *153*, G465.
(215) Liu, J. R.; Mao, Y. B.; Lan, E.; Banatao, D. R.; Forse, G. J.; Lu, J.; Blom, H. O.; Yeates, T. O.; Dunn, B.; Chang, J. P. *J. Am. Chem. Soc.* **2008**, *130*, 16908.
(216) Takahashi, N.; Yoshii, N.; Nonobe, S.; Nakamura, T.; Yoshioka, M. *J. Electron. Mater.* **2003**, *32*, 1107.
(217) Takahashi, N.; Nonobe, S.; Nakamura, T. *J. Solid State Chem.* **2004**, *177*, 3944.
(218) Levy, D. H.; Freeman, D.; Nelson, S. F.; Cowdery-Corvan, P. J.; Irving, L. M. *Appl. Phys. Lett.* **2008**, *92*, 192101.
(219) Sun, J.; Mourey, D. A.; Zhao, D. L.; Park, S. K.; Nelson, S. F.; Levy, D. H.; Freeman, D.; Cowdery-Corvan, P.; Tutt, L.; Jackson, T. N. *IEEE Electron Device Lett.* **2008**, *29*, 721.
(220) Huang, J. Y.; Wang, X. D.; Wang, Z. L. *Nano Lett.* **2006**, *6*, 2325.
(221) Gaillot, D. P.; Deparis, O.; Welch, V.; Wagner, B. K.; Vigneron, J. P.; Summers, C. J. *Phys. Rev. E* **2008**, *78*, 031922.
(222) Javey, A.; Kim, H.; Brink, M.; Wang, Q.; Ural, A.; Guo, J.; McIntyre, P.; McEuen, P.; Lundstrom, M.; Dai, H. J. *Nat. Mater.* **2002**, *1*, 241.
(223) Du, X.; George, S. M. *Sens. Actuators A* **2008**, *135*, 152.
(224) Martinson, A. B. F.; Elam, J. W.; Liu, J.; Pellin, M. J.; Marks, T. J.; Hupp, J. T. *Nano Lett.* **2008**, *8*, 2862.
(225) Nanu, M.; Schoonman, J.; Goossens, A. *Adv. Mater.* **2004**, *16*, 453.
(226) Finch, D. S.; Oreskovic, T.; Ramadurai, K.; Herrmann, C. F.; George, S. M.; Mahajan, R. L. *J. Biomed. Mater. Res. Part A* **2008**, *87A*, 100.

EXHIBIT 2

Viscous flow reactor with quartz crystal microbalance for thin film growth by atomic layer deposition

J. W. Elam,[a] M. D. Groner,[a] and S. M. George[a),b]
University of Colorado, Boulder, Colorado 80309-0215

A chemical reactor was constructed for growing thin films using atomic layer deposition (ALD) techniques. This reactor utilizes a viscous flow of inert carrier gas to transport the reactants to the sample substrates and to sweep the unused reactants and reaction products out of the reaction zone. A gas pulse switching method is employed for introducing the reactants. An *in situ* quartz crystal microbalance (QCM) in the reaction zone is used for monitoring the ALD film growth. By modifying a commercially available QCM housing and using polished QCM sensors, quantitative thickness measurements of the thin films grown by ALD are obtained in real time. The QCM is employed to characterize the performance of the viscous flow reactor during Al_2O_3 ALD. © *2002 American Institute of Physics.* [DOI: 10.1063/1.1490410]

I. INTRODUCTION

Atomic layer deposition (ALD) is a technique for depositing thin films with atomic layer control.[1,2] ALD utilizes a pair of sequential, self-limiting surface reactions applied in an ABAB... binary sequence to grow the thin film. The ALD process typically results in pinhole free and nearly atomically smooth films. Because ALD utilizes gas phase species as the reactants for the self-limiting surface reactions, ALD is able to coat conformally high aspect ratio structures such as deep trenches[3] or porous material.[4,5]

The successful application of the ALD technique requires separate exposures to the two sequential reactants. Inadvertent mixing of two reactants will result in uncontrolled growth yielding rough films with poor conformality. One method for preventing this mixing is to separate the two reactant exposures with periods of high vacuum during which the unreacted precursor and reaction products are pumped away under molecular flow conditions.[6-9] One benefit of performing ALD under high vacuum conditions is that this environment allows the application of a wide range of surface science techniques including low energy electron diffraction,[10] Auger electron spectroscopy,[11] x-ray photoelectron spectroscopy,[12] and laser induced thermal desorption.[13] These techniques permit a detailed investigation of the ALD growth process.

Separating the two sequential reactant exposures using molecular flow conditions is slow. Consequently, high vacuum reactors are not convenient for the rapid deposition of ALD films for production purposes. An alternative approach is to separate the reactant exposures using periods of inert gas purging. If the inert gas pressure is sufficiently high ($\gtrsim 100$ mTorr), then the gas will be in viscous flow. The two reactant exposures will then be separated by a gas window that acts as a diffusion barrier and allows the exposures to be spaced more closely together in time.[1,14,15] Viscous flow reactors allow ALD films to be deposited much more rapidly than molecular flow reactors.

Most of the previous ALD research utilizing viscous flow reactors has been conducted on commercially available equipment.[16,17] Only a few reports have been published concerning the details of ALD viscous flow reactors.[18-22] In particular, very little detail is typically presented regarding the gas switching valves or quantitative monitoring of ALD growth in a viscous flow reactor. This article describes the design and construction of a viscous flow ALD reactor. This reactor uses a gas pulse switching method that allows introduction of gaseous and high vapor pressure liquid precursors into the reactor.

The quartz crystal microbalance (QCM) has emerged as a powerful technique for measuring relative mass changes in real time during ALD.[18,23,24] A disadvantage of most of the previous QCM studies is the lack of mass calibration. Most QCM sensors are calibrated to measure thin films grown during physical vapor deposition with line-of-site deposition only on the front face. The difficulties of mass calibration arise because ALD occurs on the front and back surfaces of the quartz sensor. Deposition on the back surface of the QCM sensor also prohibits mass measurements during the growth of conducting materials that cause electrical shorts and stop the crystal oscillation.

One method for preventing deposition on the back of the QCM sensor is to use a custom crystal holder.[24] Alternatively, deposition on the back side can be prevented by introducing a gas purge to the crystal holder of a commercial QCM that interfaces easily with the viscous flow ALD reactor. These modifications prevent deposition on the back of the QCM sensor and yield calibrated mass results. This *in situ* QCM is then used to evaluate the performance of the viscous flow reactor during Al_2O_3 ALD.

---

[a]Department of Chemistry and Biochemistry.
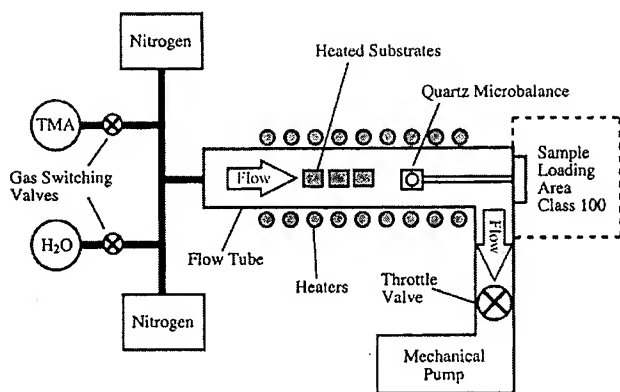[b]Department of Chemical Engineering.

FIG. 1. Schematic view of viscous flow reactor for ALD.

II. DESCRIPTION OF VISCOUS FLOW ALD REACTOR

A. Overview

Figure 1 shows a schematic of the viscous flow ALD reactor. The reactor is constructed from stainless steel components. The heated reactor flow tube has a 3.5 cm inside diameter and is approximately 60 cm long. The reactor flow tube is resistively heated externally to the desired deposition temperature. Samples loaded inside of the flow tube are heated by radiation and convection from the hot walls. This heating arrangement allows the simultaneous deposition on multiple samples with different geometries. For connections, the flow tube employs 2.75 in. Conflat flanges.

Ultrahigh purity nitrogen is supplied to mass flow controllers with a maximum throughput of 500 sccm on the trimethylaluminum (TMA) and H_2O reactant lines for Al_2O_3 ALD.[7,9,25,26] The nitrogen carrier gas is purified by an Aeronex Gate Keeper inert gas filter. This filter reduces particulate, oxygen, water, and hydrocarbon impurities to sub-ppb levels. Nitrogen flows from the reactant lines, through the flow tube, and into the exhaust mechanical pump. The exhaust mechanical pump is an Alcatel 2010 with a pumping speed of 3.2 l/s.

The pressure in the flow tube can be manually controlled by varying the conductance through the throttle valve located above the exhaust mechanical pump. The flow tube pressure is monitored by a 10 Torr Baratron capacitance manometer. Typically, the reactor is operated at a pressure of ~1 Torr with a total nitrogen carrier gas flow of 200 sccm. These conditions yield a flow velocity of ~2.5 m/s.

The sample loading and unloading area is enclosed within a class 100 clean room environment. This environment is provided by a Terra Universal Inc. universal filter/blower module equipped with a HEPA filter. The clean room environment reduces particulate contamination of the samples. This particulate reduction is critical for optimal electrical behavior of dielectric films.[27] The final HF etch and rinse of the Si(100) samples is performed within the class 100 environment prior to loading the samples into the ALD reactor.

Pulses of the TMA and H_2O reactant vapors for Al_2O_3 ALD can be alternately injected into the nitrogen carrier gas stream. The gas pulse switching is depicted by a single valve

in Fig. 1. However, the actual gas pulse switching is accomplished by an arrangement of three valves that is described in Sec. II C. The reagents used are Akzo Nobel semiconductor grade (99.9999%) trimethylaluminum and Fisher Optima purity deionized water. A quartz crystal microbalance (QCM) is located downstream of the sample substrates. The *in situ* QCM monitors the ALD film growth and is described in Sec. II D.

All of the mechanical pumps are equipped with stainless steel wool traps to prevent oil backstreaming. Care is taken to ensure that the exhaust pump oil trap is always purged with nitrogen in laminar flow to prevent oil backstreaming into the flow tube. In addition, the purge solenoid valves described in Sec. II C are kept closed when not in use to prevent contamination of the reactant dosing lines by backstreaming mechanical pump oil.

A Pentium IV based personal computer equipped with analog and digital input/output boards is used for controlling the reactor. This computer employs Labview. The computer is used for pulsing the solenoid valves, monitoring and controlling the temperature, and monitoring the reactor pressure. In addition, the computer interfaces with the quartz crystal microbalance and records the mass changes during film growth.

B. Flow tube and sample heating

The flow tube heaters are powered by a 1 kW, 40 V programmable dc power supply. The temperature of the reactor is monitored with a chromel–alumel thermocouple attached to the outside of the flow tube. Temperature regulation is provided by a proportional, integral, differential (PID) temperature controller operated by Labview running on the personal computer. The reactor temperature can be maintained in the temperature range of 50–425 °C. At 177 °C, the temperature is stable to ±0.03 °C over >14 h.

A calibration experiment was performed to evaluate the temperature difference between the reactor tube walls and the samples within the flow tube. A second chromel-alumel thermocouple was attached to a 1 in.×1 in. Si(100) sample. This Si sample was placed in the center of the flow tube and the temperatures of the sample and the outside of the flow tube were recorded for a number of different temperatures. Over the temperature range 50–325 °C, these two temperatures agreed to within ±1 °C.

A temperature gradient does exist between the center of the flow tube and the ends of the flow tube. At 325 °C, the ends of the flow tube are ~40 °C colder than the center. Because the ALD growth rate may depend on temperature, the sample substrates are always placed in the middle third of the flow tube to avoid temperature gradients. *Ex situ* ellipsometric measurements of multiple Al_2O_3 samples prepared simultaneously in the middle third of the flow reactor revealed thickness nonuniformity of only <±0.5%.

C. Reactant gas pulse switching

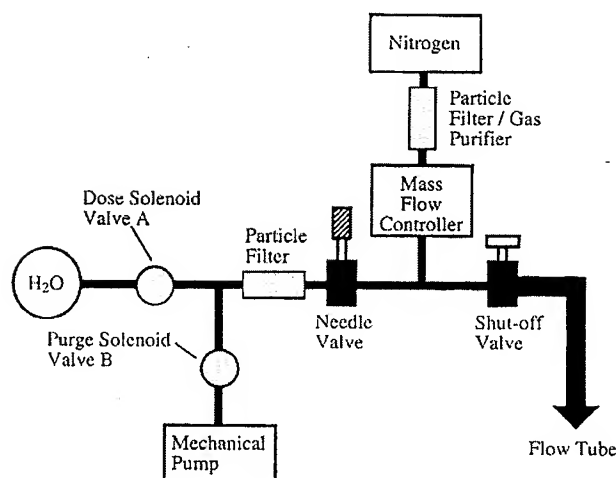Figure 2 shows the arrangement of valves used for performing the H_2O reactant gas pulse switching. An identical

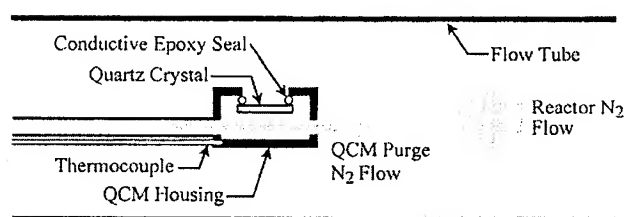FIG. 2. Arrangement of valves for reactant gas pulse switching.

FIG. 3. Schematic view of *in situ* QCM with N_2 purge on the back side of quartz crystal.

established through the needle valve. The H_2O enters the N_2 carrier gas flow and is transported into the flow tube. The sonic flow ensures consistent H_2O ALD exposures regardless of fluctuations in the flow tube pressure.

D. Quartz crystal microbalance

The QCM is usually intended to measure line-of-site deposition on the front face of the quartz crystal. Furthermore, the QCM is designed to operate at room temperature. These constraints introduce two challenges for operating a QCM in a viscous flow ALD reactor. First, the reactant gases will deposit a film on both faces of the quartz crystal and prevent calibrated mass measurements. Second, the QCM must be operated at the film deposition temperatures of $\sim 100-400\,^{\circ}C$. At these elevated temperatures, small fluctuations in the QCM sensor temperature produce large apparent mass fluctuations.

To overcome these challenges, modifications were performed to allow a nitrogen purge over the back side of the quartz crystal. In addition, polished crystals were utilized to minimize the effect of surface roughness of the detector surface. Extremely stable temperature control was also achieved using active feedback control of the heaters. These modifications provided accurate, calibrated mass measurements in the ALD flow reactor.

A schematic view of the modified quartz crystal microbalance is shown in Fig. 3. The QCM sensor is mounted in a Maxtek BSH-150 bakeable sensor housing attached to a 2.75 in. Conflat flange. The sensor housing was altered to provide a slow nitrogen purge of ~ 20 sccm to the sensor housing. In addition, Epotek P1011 high temperature conductive epoxy is used to form a gas tight, conductive seal between the front surface of the QCM sensor and the housing. This nitrogen purge and epoxy seal prevent reactant gases from entering the housing and depositing material on the back side of the QCM sensor.

The nitrogen purge flow is controlled by a Nupro M-series metering valve. To introduce the N_2 flow into the housing, a ~ 2-mm-diam hole was drilled from the inside of the housing into the water cooling line connected to the housing. The nitrogen flows through the water cooling line, through the ~ 2-mm-diam hole, and out an opening on the front of the QCM housing. The nitrogen purge over the back surface of the QCM sensor also allows mass measurements during the deposition of conducting films. When the ALD film is allowed to deposit on both the front and back surfaces of the quartz crystal,[18,23] the growth of a conducting film will

arrangement is used for the TMA reactant channel. The gas pulse switching portion of the reactor uses 1/4 in. VCR connections. The section of the gas pulse switching line downstream of the shut-off valve uses 1/2 in. VCR connections.

By constructing the gas pulse switching portion of the reactor using components employing VCR connections, the gas introduction arrangement is modular. This design allows easy reconfiguration of the components to create different arrangements. For example, adding additional reactant channels to the reactor or reconfiguring the gas switching valves to accommodate a bubbler is very straightforward.

A pair of General Valve Series 99 solenoid valves is used for switching the H_2O pulse on and off. These valves are powered by a General Valve Series II valve driver that is interfaced to the computer. Following the solenoid valve, the reactant vapor pulse passes through a particle filter and then through a needle valve. The Millipore Waferguard II filter is used to trap particulates generated by the solenoid valve A. The needle valve is a Nupro BM-series regulating valve and is used for manually controlling the magnitude of the H_2O pulse. The shut-off valve allows the H_2O channel to be isolated from the rest of the flow reactor. This shut-off valve also facilitates nitrogen purging of the H_2O channel following refilling of the H_2O reservoir.

With valve A closed and valve B open, the water pulse is turned off and the H_2O channel is in the "purge" mode. Nitrogen flows from the mass flow controller, through the needle valve, through solenoid valve B, and into the Alcatel 2004 mechanical pump. This nitrogen flow creates a gas diffusion barrier that prevents residual H_2O vapor from entering the flow tube reactor. In the purge mode, the H_2O reactant channel is immune to small H_2O leaks through solenoid valve A.

When valve B is closed and valve A is opened, the H_2O reactant channel is switched to the "exposure" mode. The pressure on the left-hand side of the needle valve rapidly reaches the vapor pressure of H_2O at room temperature, i.e., ~ 20 Torr. The pressure on the flow tube side of the needle valve is approximately equal to the pressure in the reactor tube, i.e., ~ 1 Torr. Consequently, a sonic flow of H_2O is
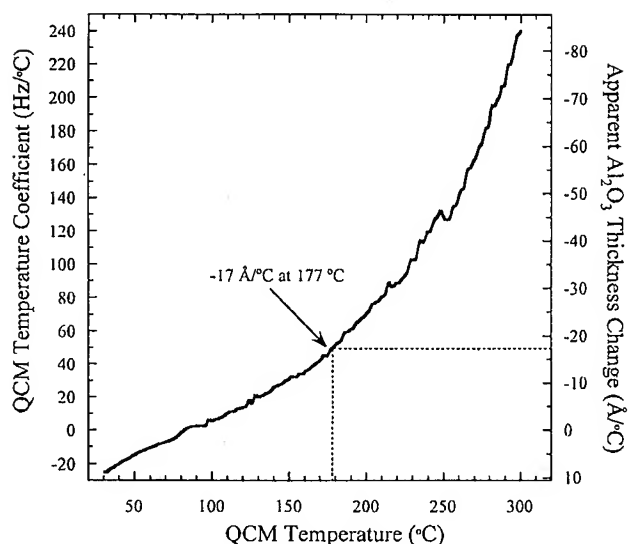
FIG. 4. QCM temperature coefficient and corresponding apparent Al_2O_3 thickness change vs QCM temperature.

cause an electrical short between the electrodes on the front and back surfaces of the quartz sensor. A thermocouple attached to the bottom of the QCM housing is also employed to monitor the QCM temperature during deposition.

Conventional QCM sensors have an intentionally roughened front surface to promote adhesion of the deposited film. Atomic force microscope (AFM) analysis of the Maxtek SC-101 unpolished QCM sensors supplied with the instrument revealed a surface area that is ~16% higher than the geometric surface area. For line-of-site deposition, this enhanced surface area does not affect the calibrated mass measurement. However, the conformal growth of the ALD film will cause the mass measurements to be ~16% higher than expectations. To avoid this problem, QCM sensors with a polished front surface were obtained from Colorado Crystal Corporation (Part No. CCAT1BK-1007-000). AFM analysis of the polished sensors indicated that their true surface area was equal to their geometric surface area within 1%.

The frequency of the QCM is monitored using a Maxtek TM400 thin film deposition monitor. The deposition monitor converts the QCM frequency to a mass per unit area. The TM400 has a mass resolution of 0.375 ng/cm^2. Assuming a density for Al_2O_3 ALD films of 3.5 g/cm^3,[9] this mass resolution equates to a thickness resolution for Al_2O_3 ALD films of 0.01 Å. The deposition monitor is interfaced to the computer via an RS232 connection and allows measurement of the film mass every 0.1 s.

Figure 4 illustrates the effect of temperature on the QCM measurements. The QCM temperature and frequency were recorded as the reactor temperature was raised slowly from 30–300 °C. The slope of the frequency versus temperature data is the QCM temperature coefficient plotted on the left axis in Fig. 4. The QCM temperature coefficient can be converted to an apparent Al_2O_3 ALD film thickness change by multiplying by 0.351 Å/Hz. The right axis of Fig. 4 shows that a +1 degree temperature increase at 177 °C will appear as an Al_2O_3 thickness change of −17 Å.

To minimize the effect of temperature on the QCM mea-

surements, a constant temperature of the viscous flow ALD reactor is maintained using a PID temperature controller. This controller is interfaced with the computer using Labview. The PID temperature controller regulates the flow tube heaters and can maintain the flow tube temperature at 177 ±0.03 °C over 14 h. This control equates to a stability of the Al_2O_3 ALD film thickness of ±0.5 Å.

III. IMPLEMENTATION OF VISCOUS FLOW REACTOR FOR Al_2O_3 ALD

### A. Selection of flow reactor conditions

Al_2O_3 ALD using TMA and H_2O has been well characterized.[7,9,25,26,28,29] This ALD system was chosen to evaluate the viscous flow ALD reactor. Previous studies have shown that the TMA and H_2O reactions require saturation exposures of ~10^4 L at the maximum Al_2O_3 growth temperature of 177 °C.[9] This exposure is equivalent to 10^{-2} Torr s. To achieve subsecond exposure times in the viscous flow ALD reactor, a reactant pressure of 0.1 Torr was selected to allow completion of the TMA and H_2O reactions in 0.1 s.

The pressure P of the N_2 carrier gas in the flow tube must be large enough to ensure viscous flow conditions. For viscous flow in the reactor, the Knudsen number, $Kn = \lambda/D$ <0.01, where λ is the mean free path and $D = 3.5$ cm is the flow tube diameter. The mean free path is obtained from $\lambda = kT/(2^{1/2}\sigma P)$. In this equation, k is the Boltzmann constant, T is temperature, and σ is the collisional cross section. For N_2 at 177 °C, $P > 0.23$ Torr ensures viscous flow.

The flow tube pressure must also be small enough to allow introduction of the reactive gas pulses into the N_2 carrier gas. The maximum reactant flow through the needle valve in Fig. 2 is obtained in sonic flow conditions when $P_2 < 0.53$ VP. P_2 is the pressure downstream of the needle valve and VP is the vapor pressure of the reactant. Neglecting the finite conductance of the gas handling line, the flow tube pressure is $P \sim P_2 < 0.53$ VP. At room temperature, TMA has a vapor pressure of VP=11 Torr and H_2O has a vapor pressure of VP~20 Torr. Consequently $P < 5.8$ Torr is sufficient to allow sonic flow of both the TMA and H_2O through the needle valves. To maintain both viscous flow and sonic flow for the reactants for Al_2O_3 ALD, the flow tube pressure should be in the range 0.23 Torr$< P < 5.8$ Torr.

Another consideration is to ensure that the pressure increases caused by the reactant gas introductions are a small perturbation to the overall flow tube reactor pressure. A small pressure transient will minimize the transport of particulate contaminants to the sample surface. The reactant pressure pulses were selected to be 0.1 Torr. A flow tube pressure of 1 Torr was then employed to be 10× larger than the reactant pressure pulses.

The N_2 mass flow rate Q can be determined after the flow tube pressure is selected at $P = 1$ Torr. Q and P are related by $Q = SP$, where S is the system pumping speed. For a given pressure, the mass flow rate will affect the flow tube velocity v according to $v = Q/(PA)$ where A is the cross sectional area of the flow tube. To minimize the purge
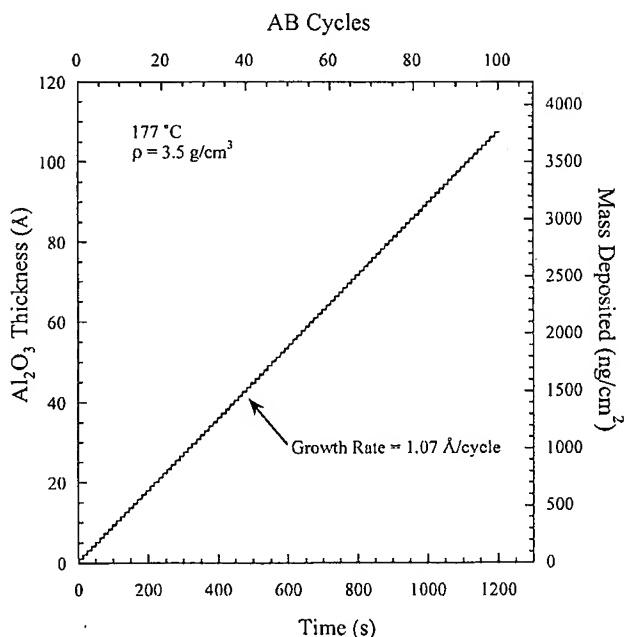
FIG. 5. QCM measurements of Al_2O_3 thickness during Al_2O_3 ALD.

times, v should be maximized to minimize diffusional broadening of the reactant pulses.

The largest flow tube velocities occur at the highest pumping speeds. S can be maximized by opening the exhaust throttle valve shown in Fig. 1. With the throttle valve fully open, S approximately equals the pumping speed of the mechanical pump. Q was selected by fully opening the throttle valve and then increasing the mass flow rate to achieve the desired flow tube pressure of $P = 1$ Torr. At a flow tube pressure of $P = 1$ Torr, the N_2 mass flow rate was $Q = 200$ sccm.

B. Quartz microbalance measurements of Al_2O_3 ALD

The QCM was used to evaluate the performance of the viscous flow ALD reactor. For these experiments, the flow tube reactor temperature was maintained at 177 °C. Alternating pulses of TMA and H_2O were injected into the N_2 carrier gas in the flow tube and the mass increase caused by Al_2O_3 growth was recorded using the QCM. The pressure increases during the TMA and H_2O reactant pulses were ~0.1 Torr. The reactant dosing lines and exhaust lines were maintained at ~80 °C to shorten surface residence times and obtain rapid ALD cycle times.

Figure 5 shows QCM measurements acquired during Al_2O_3 ALD. This data was recorded during 100 TMA/H_2O ALD cycles using reactant exposures of 1 s and nitrogen purges of 5 s between exposures. The right axis shows the mass deposited in ng/cm^2. The left axis shows the Al_2O_3 thickness deposited assuming a density of 3.5 g/cm^3. The QCM results indicate that the Al_2O_3 ALD growth rate is 1.07 Å/cycle. In addition, the QCM measurements show that the Al_2O_3 ALD growth is extremely linear and occurs in discrete steps.

Figure 6 shows the QCM step shape obtained by averaging the step shapes of the 100 ALD cycles shown in Fig. 5.
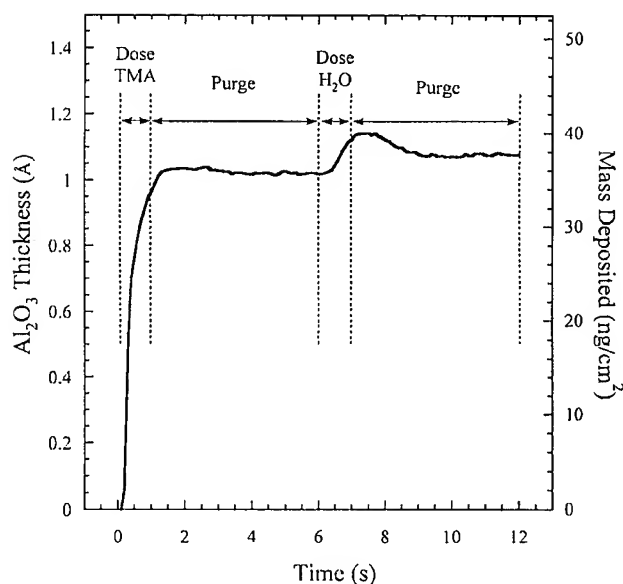
FIG. 6. Average step shape during one Al_2O_3 ALD reaction cycle using TMA and H_2O.

The dosing and purging portions of the ALD cycle are indicated in Fig. 6. The QCM pulse shape for the Al_2O_3 ALD shown in Fig. 6 agrees with previously reported QCM measurements.[29] A majority of the mass increase occurs during the TMA exposure portion of the ALD cycle. A slight net increase in mass also occurs following the H_2O exposure. The slight decrease in mass following the end of the H_2O exposure may result from the recombinative desorption of surface hydroxyl groups or the desorption of molecular water.

The QCM was used to evaluate the performance of the viscous flow ALD reactor. The results of varying the TMA and H_2O exposure times are shown in Fig. 7. Each of the data points in Fig. 7 results from measuring the average Al_2O_3 growth rate from 5–10 QCM steps at the indicated
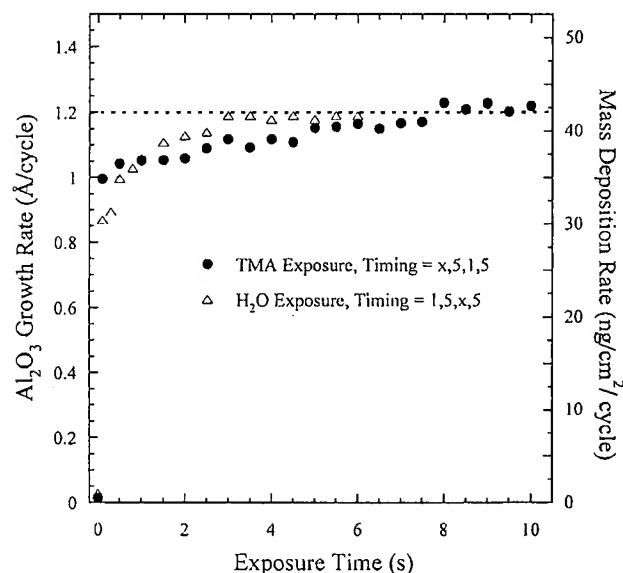
FIG. 7. Al_2O_3 ALD growth rate vs TMA and H_2O exposure times.

timing sequence. The timing sequence is t_1, t_2, t_3, t_4 where t_1 is the TMA exposure time, t_2 is the TMA purge time, t_3 is the H_2O exposure time, and t_4 is the H_2O purge time. For the experiments shown in Fig. 7, the reactant purge times were kept constant at 5 s. The TMA and H_2O exposure times were independently varied while keeping the other reactant exposure time fixed at 1 s.

The solid circles in Fig. 7 show the Al_2O_3 growth rate versus TMA exposure. The Al_2O_3 growth rate initially increases fairly rapidly, and then increases more gradually until saturating at ~1.2 Å/cycle for TMA exposures exceeding 8 s. The Al_2O_3 growth rate versus H_2O exposure displayed by the open triangles in Fig. 7 behaves in a similar manner. The Al_2O_3 growth rate saturates at ~1.2 Å/cycle for H_2O exposures greater than 3 s.

Figure 7 shows that the Al_2O_3 growth rate is ~83% of the maximum for TMA exposure times of 0.1 s and ~71% of the maximum for H_2O exposure times of 0.1 s. For exposure times of 0.1 s and reactant pressures of 0.1 Torr the reactant exposure is 10^{-2} Torr s, or 10^4 L. Previous studies of Al_2O_3 ALD determined that the Al_2O_3 growth rate saturates following ~10^4 L reactant exposures.[9] The results in Fig. 7 are in approximate agreement with these earlier investigations.

The 1.2 Å/cycle Al_2O_3 growth rate shown in Fig. 7 following saturation reactant exposures also agrees with previous measurements.[9,28] Earlier ellipsometric investigations measured an Al_2O_3 growth rate of 1.1 Å/cycle under molecular flow conditions.[9] Additional studies obtained a growth rate of ~1.2 Å/cycle from optical reflectivity measurements under viscous flow conditions using 3.5 s H_2O exposures.[28] In addition, the saturation growth rate of 1.2 Å/cycle agrees well with the 1.29 Å/cycle growth rate measured using *ex situ* ellipsometry and stylus profilometry for Al_2O_3 films deposited in the ALD flow reactor using the timing sequence 1,5,1,5.[30]

Previous studies have not determined the dependence of the Al_2O_3 ALD growth rate on the TMA exposure in detail. Other reports show an approximate leveling off at TMA exposure times of 3–4 s.[29] However, these previous studies did not measure the TMA exposure curves in great detail or at long TMA exposure times. The gradual increase in Al_2O_3 ALD growth rate versus TMA exposure shown in Fig. 7 may result from two kinetic regimes for TMA reactivity on the hydroxylated Al_2O_3 surface. Alternatively, the gradual increase in growth rate versus TMA exposure might be caused by the reaction of TMA with residual H_2O in the flow tube.

Figure 8 shows the Al_2O_3 growth rate versus purge time. During these experiments, the reactant exposures were maintained at 1 s while the TMA and H_2O purge times were independently varied from 0.1 to 3 s. The solid circles in Fig. 8 demonstrate that the Al_2O_3 growth rate remains constant at 1.07 Å/cycle for TMA purge times ≥ 0.5 s. For TMA purge times ≤ 0.5 s, the purge time is insufficient and the Al_2O_3 growth rate increases with decreasing purge time. This increase is attributed to the mixing of the TMA and H_2O reactants and subsequent Al_2O_3 chemical vapor deposition (CVD). Similarly, the open triangles in Fig. 8 reveal that H_2O purge times ≥ 1.5 s are sufficient to prevent mixing of
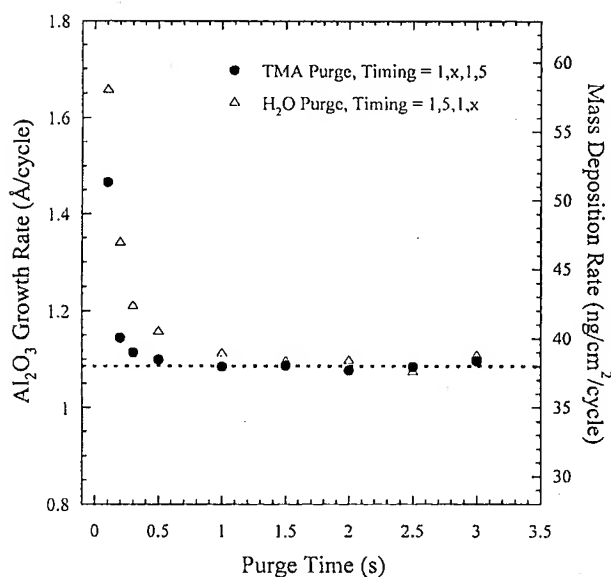

FIG. 8. Al_2O_3 ALD growth rate vs TMA and H_2O purge times.

the TMA and H_2O reactants. Al_2O_3 CVD occurs when the H_2O purge times are ≤ 1.0 s.

The reactant dosing lines were heated to ~80 °C and the flow tube was heated to 177 °C during the QCM experiments shown in Fig. 8. In a separate experiment, Al_2O_3 ALD was performed in a cold wall reactor with the dosing lines and flow tube at room temperature. Al_2O_3 was deposited on Si(100) substrates that were resistively heated to 177 °C. The thickness of the resulting Al_2O_3 ALD films were determined using *ex situ* ellipsometry. Al_2O_3 films were deposited by varying the TMA and H_2O purge times from 3–30 s. The minimum purge times were >15 s with the dosing lines and flow tube at room temperature. This long minimum purge time results from the greatly increased residence time and slower outgassing rate of H_2O on the dosing lines and reactor walls at room temperature. These results emphasize the importance of the hot wall reactor for rapid thin film growth using ALD techniques.

ACKNOWLEDGMENTS

[1] T. Suntola and J. Hyvarinen, Annu. Rev. Mater. Sci. **15**, 177 (1985).
[2] S. M. George, A. W. Ott, and J. W. Klaus, J. Phys. Chem. **100**, 13 121 (1996).
[3] M. Ritala, M. Leskela, J. Dekker, C. Mutsaers, P. J. Soininen, and J. Skarp, Chem. Vap. Deposition **5**, 7 (1999).
[4] A. W. Ott, J. W. Klaus, J. M. Johnson, S. M. George, K. C. McCarley, and J. D. Way, Chem. Mater. **9**, 707 (1997).
[5] B. S. Berland, I. P. Gartland, A. W. Ott, and S. M. George, Chem. Mater. **10**, 3941 (1998).
[6] C. H. L. Goodman and M. V. Pessa, J. Appl. Phys. **60**, R65 (1986).
[7] G. S. Higashi and C. G. Fleming, Appl. Phys. Lett. **55**, 1963 (1989).
[8] H. Kumangai and K. Toyoda, Appl. Surf. Sci. **82/83**, 481 (1994).
[9] A. W. Ott, J. W. Klaus, J. M. Johnson, and S. M. George, Thin Solid Films **292**, 135 (1997).

[10] M. Pessa, O. Jylha, P. Huttunen, and M. A. Herman, J. Vac. Sci. Technol. A **2**, 418 (1983).

[11] J. W. Elam, C. E. Nelson, R. K. Grubbs, and S. M. George, Thin Solid Films **386**, 41 (2001).

[12] Y. Yamamoto, T. Matsuura, and J. Murota, Surf. Sci. **408**, 190 (1998).

[13] O. Sneh, M. L. Wise, A. W. Ott, L. A. Okada, and S. M. George, Surf. Sci. **334**, 135 (1995).

[14] T. S. Suntola, A. J. Pakkala, and S. G. Lindfors, Apparatus for Performing Growth of Compound Thin Films, U.S. Patent No. 4389973, 1983.

[15] M. Ylilammi, J. Electrochem. Soc. **142**, 2474 (1995).

[16] T. S. Suntola, Thin Solid Films **216**, 84 (1992).

[17] J. I. Skarp, P. J. Soininen, and P. T. Soininen, Appl. Surf. Sci. **112**, 251 (1997).

[18] J. Aarik, A. Aidla, and K. Kukli, Appl. Surf. Sci. **75**, 180 (1994).

[19] A. Koukitu, N. Takahashi, and H. Seki, J. Cryst. Growth **146**, 467 (1995).

[20] B. Sang and M. Konagai, Jpn. J. Appl. Phys., Part 2 **35**, L602 (1996).

[21] J.-S. Min, Y.-W. Son, W.-G. Kang, S.-S. Chun, and S.-W. Kang, Jpn. J. Appl. Phys., Part 1 **37**, 4999 (1998).

[22] A. W. Ott and R. P. H. Chang, Mater. Chem. Phys. **58**, 132 (1999).

[23] J. Aarik, A. Aidla, H. Mandar, and T. Uustare, Appl. Surf. Sci. **172**, 148 (2001).

[24] E. B. Yousfi, J. Fouache, and D. Lincot, Appl. Phys. Lett. **153**, 223 (2000).

[25] A. C. Dillon, A. W. Ott, J. D. Way, and S. M. George, Surf. Sci. **322**, 230 (1995).

[26] A. W. Ott, K. C. McCarley, J. W. Klaus, J. D. Way, and S. M. George, Appl. Surf. Sci. **107**, 128 (1996).

[27] M. D. Groner, J. W. Elam, F. H. Fabreguette, and S. M. George, Thin Solid Films (in press).

[28] R. Matero, A. Rahtu, M. Ritala, M. Leskela, and T. Sajavaara, Thin Solid Films **368**, 1 (2000).

[29] A. Rahtu, T. Alaranta, and M. Ritala, Langmuir **17**, 6506 (2001).

[30] J. Elam and S. M. George, Thin Solid Films (in press).

EXHIBIT 3

# Al₃O₃ thin film growth on Si(100) using binary reaction sequence chemistry

A.W. Ott, J.W. Klaus, J.M. Johnson, S.M. George

Department of Chemistry and Biochemistry, University of Colorado, Boulder, CO 80309, USA

Abstract

Al₂O₃ films with precisely controlled thicknesses and excellent conformality were grown on Si(100) at low temperatures of 350–650 K using sequential surface chemical reactions. This controlled deposition was achieved by separating a binary reaction for Al₂O₃ chemical vapor deposition ($2Al(CH_3)_3 + 3H_2O \rightarrow Al_2O_3 + 6CH_4$) into two half-reactions:

(A) $AlOH^* + Al(CH_3)_3 \rightarrow AlOAl(CH_3)_2^* + CH_4$

(B) $AlCH_3^* + H_2O \rightarrow AlOH^* + CH_4$
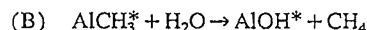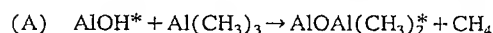
In the above reactions, the trimethylaluminum [Al(CH₃)₃] (TMA) and H₂O reactants were employed alternately in an ABAB... binary reaction sequence where the asterisks designate the surface species. At the optimal reaction conditions, a growth rate of 1.1 Å per AB cycle was measured on the Si (100) substrate using ellipsometry. These Al₂O₃ films had an index of refraction of $n = 1.65$ and a corresponding density of $\rho = 3.50$ g cm⁻³. Additional ellipsometric measurements revealed that the Al₂O₃ deposition rate per AB cycle decreased at substrate temperatures > 450 K. The decrease in the growth rate closely matched the thermal stability of the AlOH* and AlCH₃* surface species previously measured with FTIR spectroscopy. This correlation supports a reaction mechanism based on self-limiting surface chemistry. Atomic force microscope images revealed that the deposited Al₂O₃ films were exceptionally flat with a surface roughness of only ±3 Å (rms) after 500 AB cycles and the deposition of a film thickness of ~560 Å. The power spectra of the surface topography measured by AFM also demonstrated that the surface roughness was nearly identical for the initial Si(100) substrate and the deposited Al₂O₃ films after 20–500 AB reaction cycles.

Keywords: Aluminium oxide; Atomic force microscopy; Chemical vapour deposition; Ellipsometry

1. Introduction

Future developments in the microelectronics industry will be critically dependent on progress in ultrathin film deposition technology [1–3]. In particular, the ability to grow thin oxide films for use as dielectrics and insulators is central to silicon processing. Future technology will require the deposition of gate oxide films as thin as 50 Å [2]. In addition to exquisite thickness control, the ability to deposit conformal films on three-dimensional structures with high aspect ratios will play an important role in future dynamic random access memory (DRAM) technology [4,5]. The ultimate limit of thin film processing is the deposition of only one monolayer to control precisely the film thickness and simultaneously maintain conformal deposition on three-dimensional structures.

Atomic layer controlled deposition provides the means to achieve conformality and precise thickness control. The development of atomic layer controlled growth has been a major focus of recent research [6,7]. For atomic layer epitaxy (ALE) or atomic layer processing (ALP) of two-component films from elemental sources, the adsorption of each element can be self-regulating and up to a full monolayer can be deposited every adsorption cycle [6,7]. Self-terminating surface reactions may also be employed for the ALE or ALP of two-component films from molecular precursors [8–15]. This ABAB... binary reaction sequence strategy is not limited by the elemental vapor pressures and was first demonstrated by Suntola et al. for the controlled growth of ZnS films [16].

Self-limiting atomic layer controlled growth is possible through the use of two self-terminating surface reactions [6,7]. Each surface reaction occurs between a gas phase reactant and a surface functional group. The products of the first (A) surface reaction are a new deposited element, a new surface functional group and a volatile product molecule that

desorbs from the surface. The surface reaction is self-limiting because the new functional group does not react with the reactant molecule. Subsequently, the first reactant is pumped away prior to the introduction of the second reactant. The second (B) reaction occurs with a similar mechanism, deposits the other element and leaves the surface with the initial functional group. The (A) and (B) reactions can then be repeated and this procedure defines the ABAB... binary reaction sequence chemistry.

One advantage of the ABAB... binary reaction sequence approach is that the surface reaction kinetics should not affect the film growth rate. The only requirements for ALE or ALP are that the surface temperature and reactant exposure are sufficient for a complete reaction everywhere on the substrate. Small changes in surface temperature, reactant pressure and reaction times should not alter the deposition rate per AB reaction cycle provided that the reaction goes to completion. Another benefit of self-limiting surface reactions is that controlled and conformal films can be deposited on substrates with very high aspect ratio features. For deposition on structures such as a pore or trench, regular chemical vapor deposition (CVD) cannot obtain conformal deposition because the growth rate is proportional to the flux onto the surface and more material is deposited at the opening of the high aspect ratio structure.

Although ALE and ALP offer distinct advantages, several issues need to be addressed before these deposition techniques will replace conventional methods. The first obstacle is that very little is known about the surface species and surface reactions. Growth rates from 0.33 ML per cycle [11] to ~3 ML per cycle [17] have been reported under atomic layer controlled growth conditions. The factors that define and limit these growth rates reflect the underlying surface reactions. This surface chemistry must be understood to use atomic layer controlled growth effectively and to achieve the most ideal growth rates. Another question concerns the topography of films deposited with ALE or ALP deposition methods. Resultant film structure is currently reported with little explanation of the factors that govern the film structure.

Controlled deposition of Al_2O_3 has many important technological applications. Al_2O_3 ultrathin films may be useful for the formation of higher dielectric films ($\epsilon \sim 9.8$) than can be achieved with SiO_2 ($\epsilon \sim 4$) [18]. Al_2O_3 films can also provide a high-temperature, corrosion-resistant coating for metals because aluminum oxide is refractory and a fairly chemically resistant, ceramic material [19]. In addition, atomic layer controlled Al_2O_3 deposition on porous membranes could reduce the pore diameters to molecular dimensions where gas separations could be accomplished via molecular sieving mechanisms [20].

Al_2O_3 chemical vapor deposition has been previously performed using the reaction of various aluminum chloride precursors, such as $AlCl_3$, with carbon dioxide and hydrogen [21–24] and H_2O [25]. Alumina films have also been grown employing aluminum alkyl precursors, such as trimethylaluminum [$Al(CH_3)_3$] (TMA) and N_2O [26]. Various alu-

minum alkoxides have also been employed for Al_2O_3 film growth at reduced temperatures [27–30].

The binary reaction sequence chemistry for Al_2O_3 deposition has been previously reported using a number of reactant systems [12,15,17,18,31–36]. Many of these studies have concentrated on the following binary reaction [12,15,18,32,36]:

$$2Al(CH_3)_3 + 3H_2O \rightarrow Al_2O_3 + 6CH_4$$
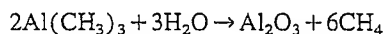
To define the ABAB... binary reaction sequence, the trimethylaluminum [$Al(CH_3)_3$] (TMA) and H_2O reactants in the binary reaction are exposed to the substrate in two separate half-reactions:

(A) $AlOH^* + Al(CH_3)_3 \rightarrow AlOAl(CH_3)_2^* + CH_4$

(B) $AlCH_3^* + H_2O \rightarrow AlOH^* + CH_4$
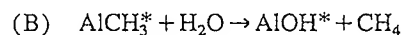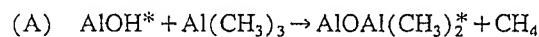
where the asterisks indicate the surface species. The growth of Al_2O_3 thin films by the sequential deposition of TMA and H_2O has been reported on both alumina [12,32,36] and silicon surfaces [18,36].

Transmission FTIR studies have also been employed to monitor both half-reactions in the binary reaction sequence versus reactant exposure and substrate temperature [12,15]. These FTIR studies showed that each half-reaction was self-terminating and both half-reactions reached completion at 500 K. In addition, the measured reaction kinetics were consistent with the reaction mechanism expressed by the above (A) and (B) half-reactions [12]. The thermal stability studies also revealed that the $AlOH^*$ and $AlCH_3^*$ surface coverages decreased approximately linearly versus substrate temperature between 300–900 K [12].

In this study, the sequential deposition of TMA and H_2O was used to deposit ultrathin Al_2O_3 films on Si(100) substrates. These investigations were performed to demonstrate the growth of atomic layer controlled and conformal Al_2O_3 films on a technologically important substrate. The Al_2O_3 film thickness deposited on Si(100) was determined using ellipsometry measurements. These experiments established the necessary reaction conditions for atomic layer controlled growth at a particular substrate temperature.

Additional ellipsometric measurements investigated the Al_2O_3 deposition rate per AB reaction cycle versus substrate temperature. These deposition rates were compared with the stability of the $AlOH^*$ and $AlCH_3^*$ surface species to establish a connection between the Al_2O_3 growth rate and the underlying surface chemistry. After determining the optimum substrate temperature, the Al_2O_3 film thickness was carefully measured versus number of AB reaction cycles to determine the Al_2O_3 deposition rate per AB reaction cycle. The surface topography of the Al_2O_3 films was also examined using atomic force microscopy (AFM). The power spectra of the surface roughness versus number of AB reaction cycles characterized the conformality and flatness of the deposited Al_2O_3 films relative to the initial Si(100) surface.

2. Experimental

A new deposition apparatus was used to grow the Al_2O_3 films using binary reaction sequence chemistry. As displayed in Fig. 1, the apparatus consists of a sample load lock chamber, a central deposition chamber, and a high vacuum surface analysis chamber. These chambers are separated by gate valves and a magnetically-coupled sample transfer arm (Surface Interface) moves the samples between the three chambers. The samples are mounted on a transfer puck that can be docked on water-cooled pedestals in either the central deposition or the surface analysis chamber. The docking stations also are equipped with current and thermocouple feedthroughs that allow the samples to be heated and temperature-regulated between 300 and 1300 K.

The central deposition chamber is capable of alternately dosing two molecular reactants under a wide variety of conditions. A cross-sectional view of the deposition chamber is shown in Fig. 2. The arrows designate the direction of gas flow through the chamber. This chamber is pumped with either a 125 1 s^{-1} diffusion pump equipped with a liquid N_2 trap or two separate liquid N_2 traps backed by mechanical pumps. The pressure is measured by a Baratron capacitance manometer with a range of 0.13 Pa to 1600 Pa. Gases are introduced via two computer-controlled valves (Series 9, General Valve) with line-of-sight to the sample.

For low pressure exposures, the reactant gases are introduced while pumping with the diffusion pump. During these short reactant exposures of $\sim$0.05–0.66 s, the peak pressure was typically 0.4–4 Pa. Much higher reactant pressures of $\sim$5–15 000 Pa can be achieved by closing off the diffusion pump and pumping the deposition chamber with two separate liquid N_2 traps backed by mechanical pumps. The TMA and H_2O were pumped separately to avoid reaction in the pumps. Following initial pumping with the liquid N_2 traps backed by mechanical pumps, lower pressures of <1.3 mPa were obtained using the 125 1 s^{-1} diffusion pump equipped with the liquid N_2 trap.

A Nicolet 740 Fourier Transform Infrared (FTIR) spectrometer and an MCT-B infrared detector were employed for the in-situ vibrational spectroscopic studies. The infrared beam passed through a pair of 13 mm thick CsI windows
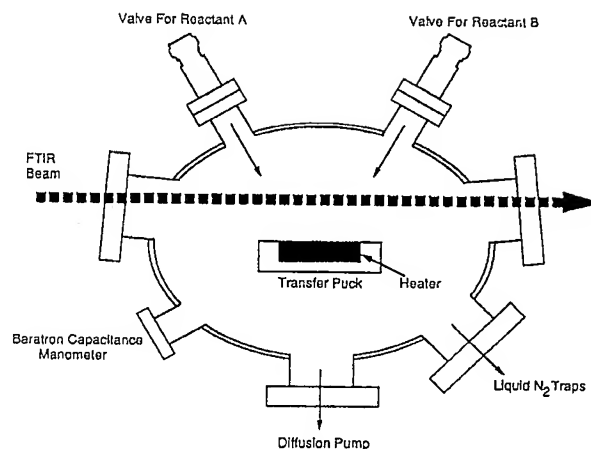

Fig. 2. Cross-sectional view of the central deposition chamber. The samples are attached to the heater on the transfer puck.

tilted 5° from vertical on the central deposition chamber as shown in Fig. 2. This geometry allows for either transmission or surface reflection infrared absorption measurements. The CsI windows could be isolated from the chamber using gate valves to prevent species from being deposited inadvertently on the windows. Sensitivity requirements limit transmission FTIR studies to high surface area materials. Either porous alumina membranes or porous silicon [12,37] provided surface areas sufficient for the transmission FTIR studies.

The surface analysis chamber is equipped with a UTI-100C quadrupole mass spectrometer and is pumped by a 210 1 s^{-1} turbomolecular pump to obtain a base pressure of <1×10^{-6} Pa. The transfer puck can be docked in this high vacuum analysis chamber to perform temperature programmed desorption (TPD) or laser-induced thermal desorption (LITD) experiments. Mass spectrometric analysis of the gases in the central deposition chamber can also be performed using a controlled leak to the surface analysis chamber.

The transfer puck contains a 5 cm diameter heater (SpectraMat). The single-crystal Si(100) samples with dimensions of 10 mm×11 mm were attached to the heater using Elgiloy™ pins. The temperature was monitored using two K-type thermocouples. One thermocouple was spot-welded directly to the molybdenum surface of the heater. The other thermocouple was attached with ceramic glue (Aremco-716) to one Si(100) sample that was mounted identically to the other samples. Up to four Si(100) wafers could be mounted on the heater at one time.

An enclosed Cu cylinder could also be mounted on the 5 cm diameter heater. An illustration of the Cu cylinder is shown in Fig. 3. Inside the cylinder, a cassette is capable of holding up to 20 horizontally stacked samples or 6 horizontally stacked and vertically mounted samples. These samples can be uniformly heated at gas pressures above 66 Pa. The top of the cylinder contains several holes to allow gases to pass in and out efficiently. On each side of the cylinder there is a 1.2 cm diameter circular opening to allow an IR beam to pass through the vertically mounted sample as illustrated in
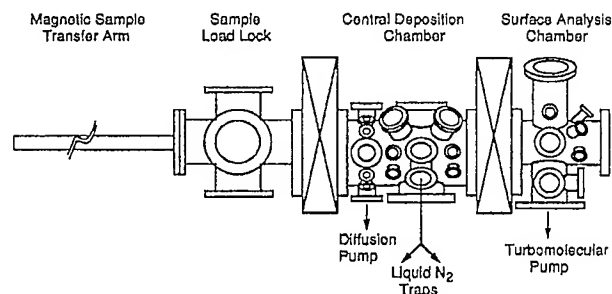

Fig. 1. Side view of the deposition apparatus showing the magnetic sample transfer arm, sample load lock, central deposition chamber and surface analysis chamber.
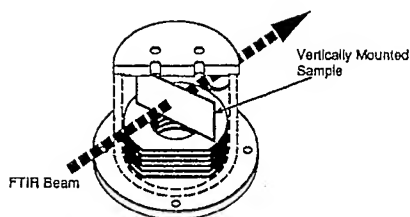
Fig. 3. Illustration of the copper cylinder that can mount to the heater on the transfer puck. Half of the copper cylinder is cut away to show the sample casette holder and the FTIR beam passing through a vertically mounted sample.

Fig. 3. In this study, the vertically mounted sample was a high surface area porous alumina membrane that was employed only initially to verify the surface reaction chemistry.

Atomic layer controlled growth of Al_2O_3 was performed on single-crystal Si(100) wafers obtained from Virginia Semiconductor. These samples were p-type, boron-doped with a resistivity of $\rho = 0.1–0.4 \ \Omega$ cm. The silicon substrates were first cleaned in 48% HF/ethanol to remove the native oxide. The samples were then rinsed with ethanol and blown free of particles before mounting. Subsequently, the silicon samples were mounted on the 5 cm diameter heater of the sample transfer puck.

After sample introduction in the deposition chamber, the surface of the Si(100) samples was cleaned with a 27 Pa, 2 min H_2O plasma at 300 K ~. This H_2O plasma also oxidizes the Si(100) sample and leaves the SiO_2 surface completely hydroxylated [38]. After pumping the H_2O using the liquid N_2 cold trap, the deposition chamber was pumped by the turbomolecular pump on the surface analysis chamber to a pressure of < 1 mPa. The Si(100) samples were then linearly ramped to the reaction temperature.

After closing the gate valve to the surface analysis chamber, TMA was flowed through the central deposition chamber. Initially, the TMA is converted to CH_4 because of reactions with $AlOH^*$ on all the chamber surfaces. Eventually, the parent TMA mass spectrometric peak at mass 72 is observed in the controlled leak from the deposition chamber to the surface analysis chamber. After this TMA exposure, the Si(100) samples were alternately exposed to TMA or H_2O at various pressures and exposure times. The time that the computer-controlled valve is open defines the exposure time. Between the exposures, the deposition chamber was evacuated to approximately 2.5–5 mPa. A typical dose sequence is shown in Fig. 4. This figure shows the pressure bursts inside the chamber measured by the capacitance manometer along with the position of each valve.

After the AB reaction cycles were completed, the Al_2O_3 film thickness on Si(100) was measured using an Rudolph Research Auto EL ellipsometer. Measurements were made in air using a HeNe laser incident at 70° relative to the surface normal. For the underlying Si(100) substrate, these ellipsometric measurements utilized the measured real and imaginary components of the index of refraction $(n + ik)$ of an
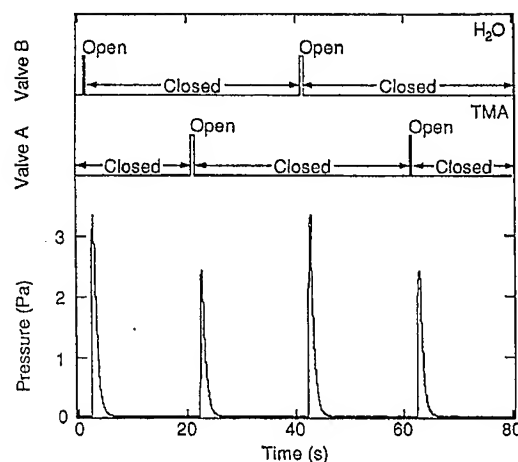

Fig. 4. Typical dosing procedure defining the binary reaction sequence showing the position of each valve and the pressure in the deposition chamber versus time.

HF-etched Si(100) wafer. These components were experimentally determined to be $n = 3.880$ and $k = 0.110$.

The surface topography of the samples was also measured using atomic force microscopy (AFM) in tapping mode on a NanoScope III from Digital Instruments. To prevent the imaging of particles on the surface, the AFM images were obtained less than 1 h after the samples had been removed from the chamber. Scan lengths of 250 nm–1.2 μm were performed using a 1.2 μm scanning head. All the images were conditioned to remove the AFM artifacts using software provided by Digital Instruments before acquiring surface roughness measurements.

The power spectral density (PSD) function was used to characterize the surface roughness. The power spectral density function is the square of the fast Fourier transform of the surface topography. The PSD function expresses the surface topography in terms of spatial frequencies and identifies the periodic surface features that define the surface structure. Alternatively, the root mean square (rms) roughness is a less precise definition of the surface topography. The rms roughness integrates over the entire PSD curve and generates a single number to characterize the surface roughness.

The Al_2O_3 films were also characterized using Sputtered Neutral Mass Spectrometry (SNMS) at AT&T Bell Laboratories. A full description of this method is given elsewhere [39–41]. Briefly, the films are sputtered using Xe ions and the sputtered neutrals are ionized by ultrahigh intensity laser pulses. For these measurements, the sputtered species were ionized with a 1 mJ, 100 fs laser pulse from a Ti:sapphire laser ~3 μs after the start of the sputter pulse. With this SNMS method, ionization efficiencies of 100% can very often be achieved within the irradiation volume. The ionized species are then separated by a magnetic sector mass spectrometer before detection. Both singly and multiply charged ions are monitored with this technique.
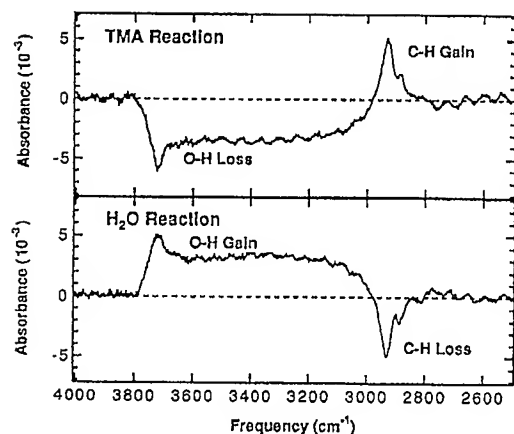
Fig. 5. (Top) FTIR spectrum of the alumina membrane in the O–H and C–H vibrational stretching region after a saturation TMA exposure at 500 K referenceD to the previously hydroxylated membrane. (Bottom) FTIR spectrum after a saturation H$_2$O exposure at 500 K referenced to the previously methylated membrane.

3. Results

Transmission FTIR spectroscopic studies were utilized to monitor the surface species on high surface area alumina membranes during the ABAB... binary reaction sequence. These membranes were mounted in the enclosed Cu cylinder in the vertical position to intersect the IR beam as shown in Fig. 3. Fig. 5(a) shows the infrared spectrum in the O–H vibrational stretching region at 3000–3800 cm^{-1} and the C–H vibrational stretching region at 2800–3000 cm^{-1}. This spectrum was recorded following a TMA exposure of 66 Pa for 1 min at 500 K. Compared with the Si(100) substrate, much higher exposures are required for the. half-reactions to reach completion because of the severe conductance limitations of the porous membranes. The FTIR spectrum is referenced to the spectrum of a fully hydroxylated alumina membrane recorded after the previous H$_2$O saturation exposure.

Fig. 5(b) displays the infrared spectrum recorded following a H$_2$O exposure of 66 Pa for 1 min at 500 K. This FTIR spectrum is referenced to the spectrum of a fully methylated alumina membrane recorded after the previous TMA saturation exposure. Fig. 5(a) shows the correspondence between the loss of AlOH* surface species and the gain of AlCH$_3^*$ surface species as expected for the (A) half-reaction. Likewise, Fig. 5(b) shows the correspondence between the gain of AlOH* surface species and the loss of AlCH$_3^*$ surface species as expected for the (B) half-reaction. For both reactions, increasing the exposure time resulted in no additional changes in the FTIR spectra.

The key characteristic of atomic layer controlled growth is self-limiting surface reactions. If the exposure time is sufficient, the surface reaction will saturate and additional reactant exposure will not produce additional film growth. Fig. 6 shows the Al$_2$O$_3$ film thicknesses on Si(100) after 250 AB cycles at 450 K versus the reactant exposure time. These AB cycles were performed using the following sequence: dose
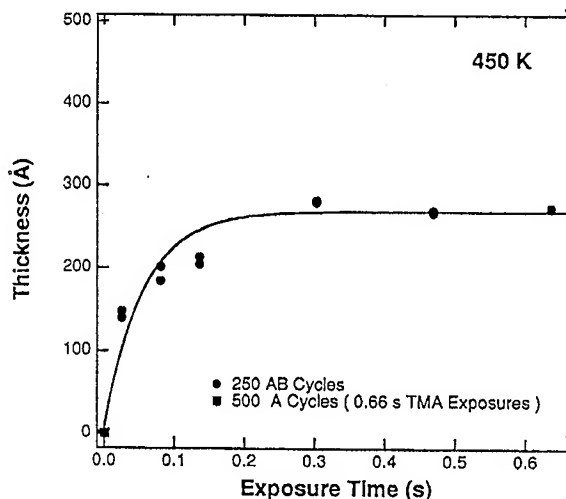

Fig. 6. Thickness of deposited Al$_2$O$_3$ films on Si(100) versus reactant exposure time after 250 AB cycles at 450 K. The thicknesses were measured using ellipsometry.

A/evacuate (<5 mPa)/dose B/evacuate (<5 mPa). The thickness variation measured by ellipsometry on a single Al$_2$O$_3$ film was never more than ±3 Å. The solid line in Fig. 6 is intended only to guide the eye.

For exposure times <0.33 s, the Al$_2$O$_3$ film thickness increases rapidly with reactant exposure time. In this regime, the reactions are not saturating on the surface and the growth rate is very sensitive to the reactant exposure. For exposure times >0.33 s, the growth rate after 250 AB cycles is independent of the reactant exposure. This behavior indicates that both half-reactions in the binary reaction sequence are saturating after 0.33 s exposures. The measured growth rate is very consistent provided that the chamber is pumped to <5 mPa between exposures. If the pressure rises above this pressure, thicker Al$_2$O$_3$ films are grown as the two reactants coexist in the chamber and conventional CVD occurs on the surface.

The residual gas in the chamber after an H$_2$O dose and subsequent pumping to <5 mPa was analyzed using the mass spectrometer. This analysis revealed that the partial H$_2$O pressure comprised ~10% of the total pressure. The remainder of the total pressure was CH$_4$. Consequently, we estimate that partial pressures of reactants <0.5 mPa are necessary to avoid cross contamination and the resulting conventional CVD processing on the surface. The large amount of CH$_4$ in the deposition chamber is consistent with the half-reactions occurring on the chamber walls. In corroboration, visible films have grown on the deposition chamber during the course of this work.

Residual H$_2$O vapor might lead to Al$_2$O$_3$ deposition during the TMA exposure by the conventional CVD reaction $2Al(CH_3)_3 + 3H_2O \rightarrow Al_2O_3 + 6CH_4$. To test this possibility, one sample was subjected to 500 TMA reaction cycles using an exposure time of 0.66 s at 450 K. No H$_2$O was introduced during its normal time in the ABAB... binary reaction sequence. During the 500 TMA cycles, the residual H$_2$O
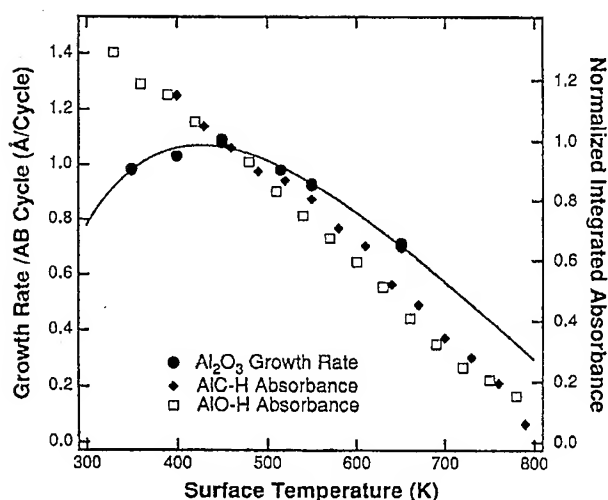
Fig. 7. Growth rate per AB reaction cycle for Al_2O_3 deposition on Si(100) versus surface temperature. These growth rates were measured using 250 AB cycles with 0.5 s exposure times. The integrated infrared absorbances for the $AlCH_3^*$ and $AlOH^*$ surface species on alumina membranes versus surface temperature are shown for comparison.

Fig. 8. Thickness of deposited Al_2O_3 films on Si(100) versus number of AB cycles at 450 K with 0.5 s exposure times.

vapor pressure was < 1 mPa. After this experiment, no Al_2O_3 film growth was observed by the ellipsometric measurements. This measurement point is included at the origin in Fig. 6.

Under conditions where the surface half-reactions are saturating, the effect of surface temperature on the Al_2O_3 growth rate can be determined by measuring the Al_2O_3 film thickness after 250 AB cycles. These AB cycles were performed using the following sequence: A (0.5 s)/evacuate (20 s)/B (0.5 s)/evacuate (20 s). The peak pressure was 2.0–2.4 Pa during the 0.5 s TMA exposures and 2.6–3.7 Pa during the 0.5 s H_2O exposures. The dose profile shown in Fig. 4 is representative of this dose sequence. The residual pressure at the end of each evacuation cycle was 3–5 mPa. The exposure time of 0.5 s was sufficient to reach saturation at all temperatures from 350–650 K.

Fig. 7 shows the Al_2O_3 growth rate as measured by ellipsometry for surface temperatures from 350 to 650 K. The Al_2O_3 growth rate is highest at 450 K. The growth rate per AB cycle decreases progressively for temperatures > 450 K. The thermal stabilities of $AlCH_3^*$ and $AlOH^*$ functional groups on a porous alumina substrate are also displayed in Fig. 7. These stabilities were measured previously using transmission FTIR spectroscopy and are normalized to the surface coverage at 450 K [12]. The decrease in the growth rate at temperatures > 450 K is interpreted in terms of the coverage of the surface species as discussed in Section 4.

The optimum Al_2O_3 growth rate per AB cycle is obtained at 450 K. Fig. 8 shows the Al_2O_3 film thickness as a function of AB cycles at 450 K. These AB cycles were performed using the following sequence: A (0.5 s)/evacuate (20 s)/B (0.5 s)/evacuate (20 s). The growth rate is clearly constant versus number of AB cycles. A growth rate of 1.1 Å per AB cycle is obtained from these ellipsometric results. The real index of refraction of these Al_2O_3 films was also measured
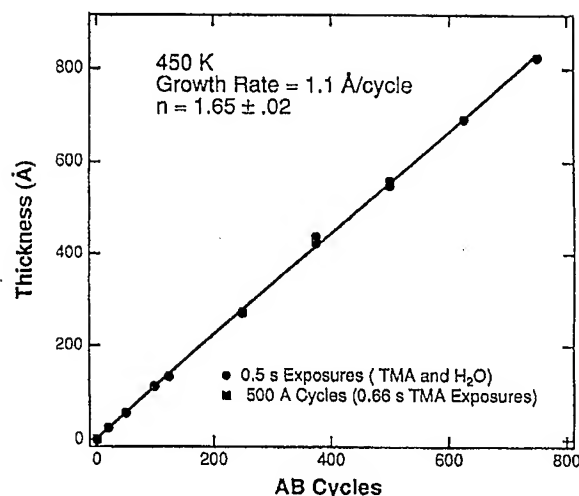
to be $n = 1.65 \pm 0.02$ assuming that absorption is negligible ($k = 0$).

Atomic force microscopy (AFM) images were recorded for many of the Al_2O_3 films deposited during the growth rate experiments at 450 K. The AFM scan lengths were 250 nm and 1.2 μm. The AFM images obtained using a 250 nm scan length from Al_2O_3 films deposited after 20, 100, and 500 AB cycles are shown in Fig. 9. A Si(100) wafer that had been treated identically to the other samples prior to the H_2O plasma is also shown for comparison. The gray scale in Fig. 9 spans less than 10 Å dark-to-light. These images reveal that the Al_2O_3 films are extremely flat and uniform. Each film has a roughness of < ±3 Å (rms). Results were similar using a 1.2 μm scan length. Fig. 10 shows the power spectral density obtained from the AFM images shown in Fig. 9 using an algorithm provided by Digital Instruments. In each case, the topography of the deposited Al_2O_3 film resembles the topography of the initial Si(100) substrate.

Depth profiling experiments performed at AT&T Bell Laboratories were also used to characterize the deposited Al_2O_3 film and the Al_2O_3/Si interface. Fig. 11 shows a sputtered neutral mass spectrometer (SNMS) depth profile of a Al_2O_3 film on Si(100) that was measured to be 560 Å thick by ellipsometry. The signals have been corrected for the relative sputter rates of the Al_2O_3 film and Si(100) substrate. Fig. 11 indicates that the deposited Al_2O_3 film contains only aluminum, oxygen, and a small amount of carbon similar to the amount in the Si substrate. Given the ~50 Å spatial resolution for the SNMS depth profile technique, an abrupt interface is observed as expected for atomic layer controlled growth. Although the Al_2O_3 film appears to be nearly carbon free, there is clearly more carbon at the Al_2O_3/Si interface.

4. Discussion

Previous transmission FTIR experiments examined the two half-reactions for the atomic layer controlled deposition of Al_2O_3 [12]:
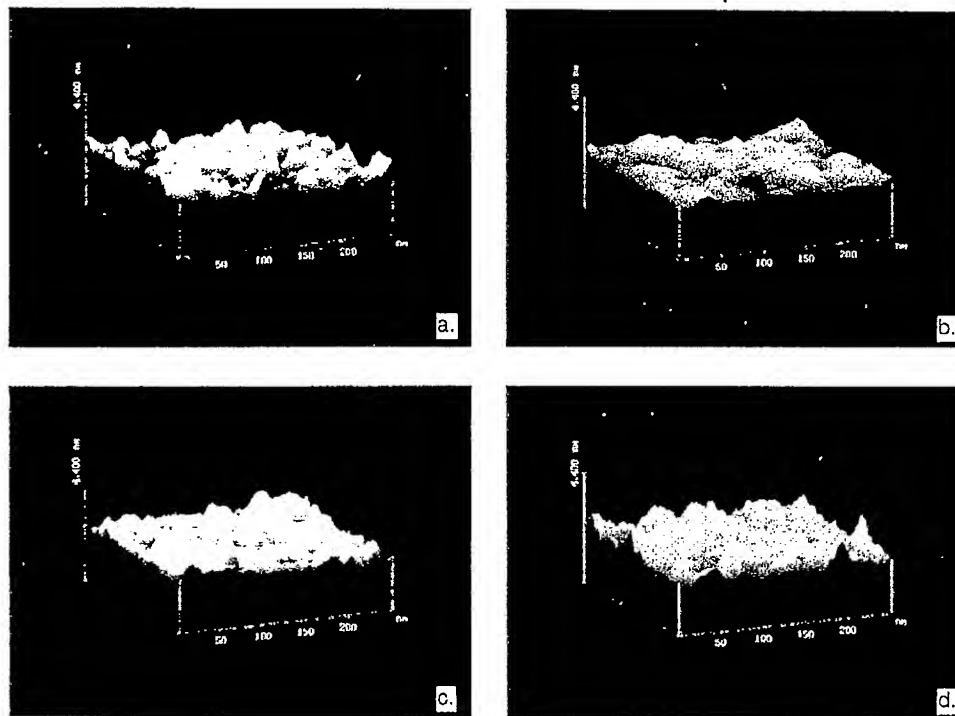
Fig. 9. Atomic force microscope (AFM) images of: (a) the Si(100) surface after the HF etch and H$_2$O plasma treatment; and deposited Al$_2$O$_3$ film on Si(100) after (b) 20 AB cycles, (c) 100 AB cycles and (d) 500 AB cycles with 0.5 s exposure times at 450 K. Each division in the z scale represents 22 Å.
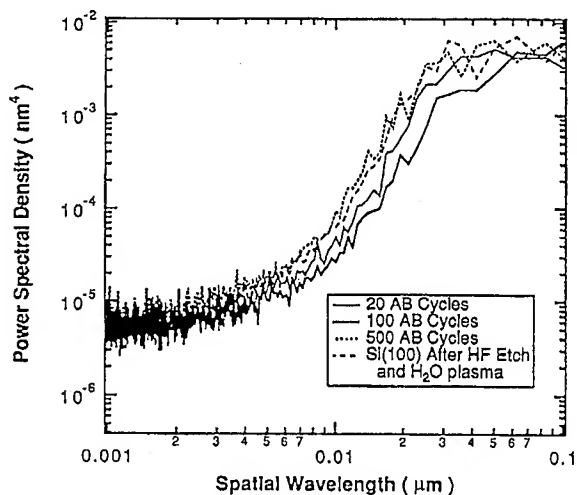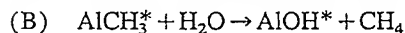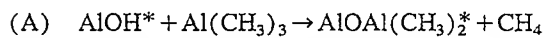

Fig. 10. Power spectral density versus spatial wavelength of the atomic force microscope images shown in Fig. 9.

(A) $AlOH^* + Al(CH_3)_3 \rightarrow AlOAl(CH_3)_2^* + CH_4$

(B) $AlCH_3^* + H_2O \rightarrow AlOH^* + CH_4$

These earlier FTIR studies on porous alumina membranes determined that temperatures of 500 K and pressures of 40 Pa for 1 min were required for the half-reactions to reach completion [12]. Similar investigations were conducted in the new deposition chamber to establish the reproducibility of these reaction conditions. Fig. 5(a) shows the absorbance loss in the O–H stretching region and absorbance gain in the

C–H stretching region that are concurrent in the FTIR difference spectrum after an H$_2$O exposure of 66 Pa for 1 min at 500 K. This behavior is consistent with the previous results and is expected for the self-limiting surface chemistry implied by the (A) half-reaction.

Fig. 5(b) shows the corresponding FTIR difference spectra for the O–H and C–H stretching regions after a TMA exposure of 66 Pa for 1 min at 500 K. The absorbance gain for the O–H stretching vibration and the absorbance loss for
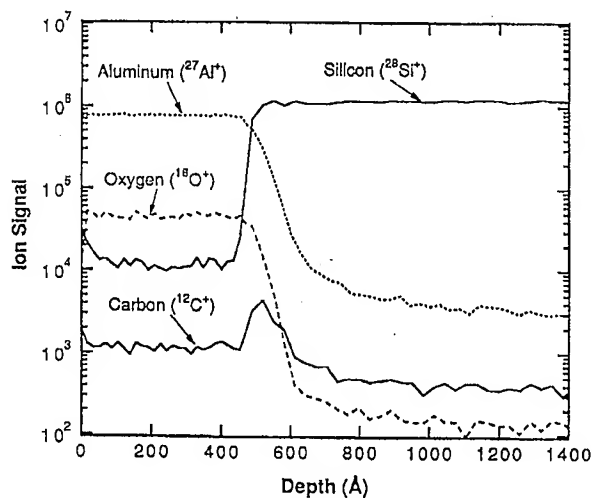

Fig. 11. Sputtered neutral mass spectrometry (SNMS) depth profile of an Al$_2$O$_3$ film on Si(100) after 500 AB cycles at 450 K that was measured to be 560 Å thick by ellipsometry.

the C–H stretching vibration are concurrent for the TMA reaction. This behavior is in agreement with the previous results and is predicted by the self-limiting surface chemistry implied by the (B) half-reaction. These FTIR results demonstrate that our new apparatus has successfully duplicated the original conditions of the earlier experiments [12].

To prove that self-limiting surface chemistry is controlling thin film growth, the growth rate must be measured versus reactant exposure. The signature of self-limiting surface chemistry is a growth rate that saturates after a certain exposure. Fig. 6 shows that the Al_2O_3 growth rate saturates for exposure times ≥ 0.33 s. This behavior argues that the two surface half-reactions reach completion for exposure times ≥ 0.33 s under these reaction conditions. The definition of completion is that all the $AlOH^*$ or $AlCH_3^*$ functional groups are exchanged to $AlCH_3^*$ or $AlOH^*$, respectively, during the (A) or (B) half-reactions.

Fig. 6 also reveals that the experiments employing only 500 TMA cycles observed no Al_2O_3 growth. These results indicate that the reaction of TMA with residual H_2O vapor is negligible when the H_2O background pressure is low. Other experiments were conducted where the evacuation time after the H_2O exposure was shorter and residual H_2O pressure was present during the TMA exposure. Slightly higher Al_2O_3 growth rates were observed during these AB reaction cycles. These higher growth rates were attributed to Al_2O_3 deposition from both the atomic layer controlled growth and conventional CVD. Additional growth experiments revealed that self-limiting behavior is observed and Al_2O_3 growth rates are constant provided that the H_2O partial pressure in the deposition chamber is ≤ 0.5 mPa between the H_2O and TMA exposures.

Fig. 7 shows that the Al_2O_3 growth rate increases slightly versus temperature for $T \leq 450$ K. This behavior is consistent with previous FTIR experiments that showed that the TMA reaction is thermally activated and does not go to completion at lower temperatures [12]. The maximum Al_2O_3 growth rate of 1.1 Å per AB cycle is obtained at 450 K. The growth rate then decreases approximately linearly with temperature from 450 to 650 K. This decrease is coincident with a decrease in the number of $AlOH^*$ and $AlCH_3^*$ functional groups on the surface. The integrated infrared absorbance of these functional groups versus temperature on the porous alumina membranes is included in Fig. 7. This correspondence between Al_2O_3 growth rate and the $AlOH^*$ and $AlCH_3^*$ surface species provides additional evidence for self-limiting surface chemistry and deposition that is controlled by the number of reactive surface species.

The dehydroxylation of the Al_2O_3 surface versus temperature has been well documented by earlier investigations [12,42,43]. Hydroxyl groups can be lost from the Al_2O_3 surface by the recombinative desorption of two $AlOH^*$ species to produce H_2O:

$$2AlOH^* \rightarrow Al-O-Al^* + H_2O(g)$$
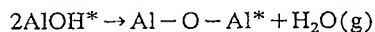
The mechanism for methyl lost versus temperature is not known at this time. One possibility is methyl radical desorption:

$$AlCH_3^* \rightarrow Al^* + CH_3(g)$$
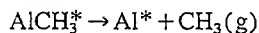
This behavior is suggested by previous studies on GaAs surfaces [44,45]. Al and Ga are both Group III elements that bind –CH_3. Methyl radicals have been observed to desorb from GaAs surfaces over a wide variety of temperatures [46].

The reactions of $Al(CH_3)_3$ and H_2O are possible with the oxygen bridge-bonded sites [12]:

$$Al-O-Al^* + Al(CH_3)_3$$
$$\rightarrow Al-O-Al(CH_3)_2^* + Al-CH_3^*$$

$$Al-O-Al^* + H_2O \rightarrow 2AlOH^*$$
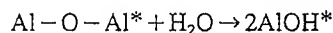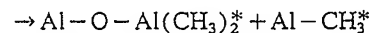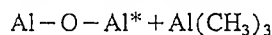
The concurrent decrease in the Al_2O_3 growth rate and the coverage of $AlOH^*$ and $AlCH_3^*$ functional groups argues that the oxygen bridge-bonded sites play a minor role in the chemistry of Al_2O_3 growth rate. The correlation between the Al_2O_3 growth rate and the surface species indicates that Al_2O_3 growth is dictated by reactions with the $AlOH^*$ and $AlCH_3^*$ functional groups.

The Al_2O_3 growth rates were not measured at temperatures higher than 650 K. These higher temperatures were avoided because TMA can pyrolyze at $T > 650$ K and deposit aluminum on the surface [47]. This aluminum layer can then be oxidized by H_2O to produce an Al_2O_3 film. This Al_2O_3 growth will not be atomic layer controlled and will probably result in non-conformal film growth on high aspect ratio structures. In agreement with these expectations, higher growth rates of 10 Å per AB cycle have been observed at $T > 650$ K using TMA and hydrogen peroxide [17].

The real index of refraction of the deposited Al_2O_3 films at $T \geq 450$ K was $n = 1.65 \pm 0.03$ as determined by the ellipsometry measurements. This index is consistent with an Al_2O_3 film with a density of $\rho = 3.5$ g cm^{-3} through the Lorentz–Lorenz relationship [48]. Compared with the density of $\rho = 3.97$ g cm^{-3} for α-Al_2O_3 [49], this refractive index indicates a more open Al_2O_3 structure similar to the densities of $\rho = 3.5–3.7$ g cm^{-3} for γ-Al_2O_3 or amorphous alumina [49,50]. These lower density Al_2O_3 films are also in agreement with our earlier FTIR spectra of Al_2O_3 films deposited on Si(100) [12]. These spectra were consistent with amorphous Al_2O_3.

The film density of $\rho = 3.5$ g cm^{-3} can be used to estimate the film thickness of one Al_2O_3 layer. This density corresponds to a number density of $n = 2.07 \times 10^{22}$ Al_2O_3 units cm^{-3}. The thickness, d, of one monolayer can be estimated using $d \sim n^{-1/3} = 3.64$ Å. The measured growth rates of 1.1 Å per AB reaction cycle at 450 K and < 1.1 Å per AB reaction cycle at $T > 450$ K are all lower than this estimated monolayer thickness.

An Al_2O_3 growth rate of 1.1 Å per AB reaction cycle and film density of $\rho = 3.5$ g cm^{-3} yield a deposition rate per AB reaction cycle at 450 K of 4.5×10^{14} aluminum atoms cm^{-2}

and 6.8×10^{14} oxygen atoms cm^{-2}. These deposition rates can be compared with the coverage of the AlOH* and AlCH$_3^*$ surface species. The monolayer coverage of hydroxyl groups on γ-Al$_2$O$_3$ is $\Theta_{OH} = 1.25 \times 10^{15}$ cm^{-2} [51,52]. At 450 K, the hydroxyl coverage on γ-Al$_2$O$_3$ [42,51] or amorphous Al$_2$O$_3$ [12] is reduced by dehydroxylation and is ~ 70–80% of the fully hydroxylated monolayer coverage or $\Theta_{OH} \sim 9.4 \times 10^{14}$ cm^{-2}.

The absolute AlCH$_3^*$ coverage has not been quantified on Al$_2$O$_3$. However, the relative thermal stability of AlCH$_3^*$ has been measured on alumina membranes [12]. The methyl coverage at 450 K is $\sim 80\%$ of the fully methylated coverage at 300 K [12]. If the methyl coverage does not limit the Al$_2$O$_3$ growth rate, the oxygen deposition rate should be comparable to or greater than the hydroxyl coverage [11]. In contrast, the oxygen deposition rate at 450 K is lower than the maximum possible hydroxyl coverage. This behavior suggests that the oxygen deposition rate is affected by the thermal stability of both methyl and hydroxyl surface species.

Fig. 8 reveals that the Al$_2$O$_3$ film thickness is directly proportional to the number of AB cycles. This plot yields an Al$_2$O$_3$ growth rate of 1.1 Å per AB cycle. The constant growth rate versus number of AB cycles indicates that the number of reactive sites on the Al$_2$O$_3$ surface is not changing versus film growth. The constant growth rate also argues that the surface area is not increasing during the Al$_2$O$_3$ film growth. In addition, the constant growth rate after only 20–50 AB cycles indicates that the initial Al$_2$O$_3$ deposition is not perturbed by the underlying SiO$_2$/Si substrate. All of these observations are consistent with the growth of a conformal Al$_2$O$_3$ film beginning with the initial AB reaction cycles.

A surface roughness of <3 Å (rms) was obtained from the AFM measurements for all the Al$_2$O$_3$ films grown at 450 K shown in Fig. 8. In comparison, the surface roughness for a cleaned Si(100) substrate was ~ 2 Å (rms). The plots of power spectral density versus spatial wavelength displayed in Fig. 10 also indicate that the film surface topography is not changing during film growth. The nearly identical power spectral density plots are consistent with conformal film growth and surface topography that does not change with number of AB reaction cycles. This behavior is in marked contrast to the large surface roughness that evolves during the growth of crystalline TiO$_2$ films using analogous binary reaction sequence chemistry techniques [53,54].

The composition of the Al$_2$O$_3$ films on Si(100) was also examined by sputtered neutral mass spectrometry (SNMS) depth profiling at AT&T Bell Laboratories. The composition of the Al$_2$O$_3$ films was determined to be almost entirely Al and O. Very small levels of carbon were observed that were similar to the carbon concentrations measured in the Si(100) wafer. Fig. 11 clearly shows that there is an increase in carbon at the Al$_2$O$_3$/Si interface. These higher carbon concentrations may indicate that Al(CH$_3$)$_3$ can decompose and deposit some carbon on the initial oxidized Si(100) substrate.

5. Conclusions

Sequential surface chemical reactions were used to deposit atomic layer controlled and conformal Al$_2$O$_3$ films on Si(100). In this approach, the binary reaction $2Al(CH_3)_3 + 3H_2O \rightarrow Al_2O_3 + 6CH_4$ was separated into two half-reactions:

(A)   AlOH* + Al(CH$_3$)$_3$ → AlOAl(CH$_3$)$_2^*$ + CH$_4$

(B)   AlCH$_3^*$ + H$_2$O → AlOH* + CH$_4$
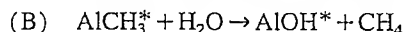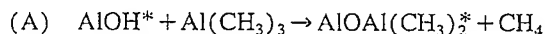
where the asterisks denote the surface species. Al$_2$O$_3$ films were grown using an ABAB... binary reaction sequence. Under the proper reaction conditions, ellipsometry measurements were consistent with self-limiting half-reactions during this Al$_2$O$_3$ deposition on Si(100). These ellipsometric results were also in agreement with previous FTIR spectroscopic studies of the surface chemistry underlying this binary reaction sequence chemistry.

Optimum Al$_2$O$_3$ growth rates of 1.1 Å per AB cycle were observed at 450 K with ≥ 0.33 s exposure times of TMA and H$_2$O at ~ 1.3–4.0 Pa. The ellipsometric measurements also yielded a refractive index of $n = 1.65 \pm 0.02$ that is consistent with a Al$_2$O$_3$ film density of $\rho = 3.5$ g cm^{-3}. For substrate temperatures >450 K, the growth rate progressively decreased in close correspondence with the thermal stability of the AlOH* and AlCH$_3^*$ surface functional groups. This close agreement between growth rate and surface coverage provides additional evidence for self-limiting surface chemistry as expressed by the (A) and (B) half-reactions.

The growth rate was extremely linear as expected for conformal deposition on the Si(100) surface. In agreement with the linear and conformal growth, atomic force microscope images revealed exceptionally flat and conformal Al$_2$O$_3$ films with a surface roughness of only ± 3 Å (rms) after the deposition of a 560 Å film thickness using 500 AB reaction cycles. Comparisons of the power spectral density versus spatial wavelength also showed that the surface topographies were essentially identical for the various Al$_2$O$_3$ films deposited using 20–500 AB cycles and the initial Si(100) substrate.

References

[1] P.K. Chatterjee and G.B. Graydon, *IEEE Trans. Syst., 1* (1993) 7.

[2] A. Masaki, *IEEE Circ. Dev., 8* (1992) 18.

[3] T. Venkatesan, *Thin Solid Films, 216* (1992) 52.

[4] G. Kitsukawa, M. Horiguchi, Y. Kawahara, T. Akiba, Y. Kawase, T. Tachibana, T. Sakai, M. Aoki, S. Shukuri, K. Sagara, R. Nagai, Y. Ohji, N. Hasegawa, T. Yokoyama, T. Kusi, H. Yamashita, T. Kure and T. Nishida, *IEEE J. Solid State Circuits, 28* (1993) 1105.

[5] Y. Nakagome and K. Itoh, *IEICE Trans., E-74* (1991) 799.

[6] C.H.L. Goodman and M.V. Pessa, *J. Appl. Phys., 60* (1986) R65.

[7] T. Suntola, *Thin Solid Films, 216* (1992) 84.

[8] J. Nishizawa, A. Hitoshi and T. Kurabayashi, *J. Electrochem. Soc., 132* (1985) 1197.

[9] J. Nishizawa, T. Kurabayashi and H. Abe, *Surf. Sci., 185* (1987) 249.

[10] M. Ritala and M. Leskela, *Thin Solid Films, 225* (1993) 288.

[11] O. Sneh, M.L. Wise, A.W. Ott, L.A. Okada and S.M. George, *Surf. Sci., 334* (1995) 135.

[12] A.C. Dillon, A.W. Ott, J.D. Way and S.M. George, *Surf. Sci., 322* (1995) 230.

[13] E.-L. Lakomåå, S. Haukka and T. Suntola, *Appl. Surf. Sci., 60* (1992) 742.

[14] T. Asikainen, M. Ritala and M. Leskelo, *J. Electrochem. Soc., 141* (1994) 3210.

[15] S.M. George, O. Sneh, A.C. Dillon, M.L. Wise, A.W. Ott, L.A. Okada and J.D. Way, *Appl. Surf. Sci., 82/83* (1994) 460.

[16] M. Pessa, R. Makela and T. Suntola, *Appl. Phys. Lett., 38* (1981) 131.

[17] H. Kumagai, K. Toyoda, M. Matsumoto and M. Obara, *Jpn. J. Appl. Phys., 32* (1993) 6137.

[18] G.S. Higashi and C.G. Fleming, *Appl. Phys. Lett., 55* (1989) 1963.

[19] B. Lux, C. Colombier and H. Altena, *Thin Solid Films, 138* (1986) 49.

[20] J.D. Way and D.L. Roberts, *Sep. Sci. Tech., 27* (1992) 29.

[21] S.W. Choi, C. Kim, J.G. Kim and J.S. Chun, *J. Mater. Sci., 22* (1987) 1051.

[22] K. Iida and T. Tsujide, *Jpn. J. Appl. Phys., 11* (1972) 840.

[23] C.S. Park, J.G. Kim and J.S. Chun, *J. Electrochem. Soc., 130* (1983) 1607.

[24] J.G. Kim, C.S. Par and J.S. Chun, *Thin Solid Films, 97* (1982) 97.

[25] D. Messier and P. Wong, *J. Electrochem. Soc., 118* (1971) 773.

[26] M. Ishida, I. Katakabe, T. Nakamura and N. Ohtake, *Appl. Phys. Lett., 52* (1988) 1326.

[27] V.A.C. Haanappel, H.D. van Corbach, T. Fransen and P.J. Gellings, *Thin Solid Films, 230* (1993) 138.

[28] S.S. Yom, W.N. Kang, Y.S. Yoon, J.I. Lee, D.J. Choi, T.W. Kim, K.Y. Seo, P.H. Hur and C.Y. Kim, *Thin Solid Films, 213* (1992) 72.

[29] J.S. Kim, H.A. Marzouk, P.J. Reucroft, J.D. Robertson and C.E. Hamrin, *Thin Solid Films, 230* (1993) 156.

[30] T. Maruyama and T. Nakai, *Appl. Phys. Lett., 58* (1991) 2079.

[31] L. Hiltunen, H. Kattelus, M. Leskela, M. Makela, L. Niinisto, E. Nykanen, P. Soininen and M. Tiitta, *Mater. Chem. Phys., 28* (1991) 379.

[32] C. Soto and W.T. Tysoe, *J. Vac. Sci. Technol., A9* (1991) 2686.

[33] G. Oya and Y. Sawada, *J. Cryst. Growth, 99* (1990) 572.

[34] J.F. Fan, K. Sugioka and K. Toyoda, *Jpn. J. Appl. Phys., 30* (1991) L1139.

[35] J.F. Fan and K. Toyoda, *Jpn. J. Appl. Phys., 32* (1993) L1349.

[36] A.W. Ott, K.C. McCarley, J.W. Klaus, J.D. Way and S.M. George, *Appl. Surf. Sci.,* in press.

[37] P. Gupta, V.L. Colvin and S.M. George, *Phys. Rev., 37* (1988) 8234.

[38] O. Sneh and S.M. George, *J. Phys. Chem., 99* (1995) 4639.

[39] M.L. Wise, A.B. Emerson and S.W. Downey, *Anal. Chem., 67* (1995) 4033.

[40] M.L. Wise, N. Moriya and S.W. Downey, *Surf. Interface Anal.,* in press.

[41] M.L. Wise, S.W. Downey and A.B. Emerson, *J. Mater. Res.,* in press.

[42] H. Knozinger and P. Ratnasamy, *Catal. Rev.-Sci. Eng., 17* (1978) 31.

[43] M. Zamora and A. Córdoba, *J. Phys. Chem., 82* (1978) 584.

[44] J.E. Butler, N. Bottka, R.S. Sillmon and D.K. Gaskill, *J. Cryst. Growth, 77* (1986) 163.

[45] J.R. Creighton, K.R. Lykke, V.A. Shamamian and B.D. Kay, *Appl. Phys. Lett., 57* (1990) 279.

[46] J.R. Creighton, *Surf. Sci., 234* (1990) 287.

[47] T.M. Mayer, J.J.W. Rogers and T.A. Michalske, *Chem. Mater., 3* (1991) 641.

[48] M. Born and E. Wolf, *Principles of Optics,* Pergamon Press, Oxford, 1975.

[49] *CRC Handbook of Chemistry and Physics,* CRC Press, Boca Raton, FL, 1984.

[50] *American Institute of Physics Handbook,* Am. Inst. Phys., New York, NY, 1982.

[51] J.B. Peri, *J. Phys. Chem., 69* (1965) 211.

[52] J.B. Peri, *J. Phys. Chem., 69* (1965) 220.

[53] M. Ritala, M. Leskela, L.S. Johansson and L. Niinisto, *Thin Solid Films, 228* (1993) 32.

[54] H. Kumagai, M. Matsumoto, M. Obara and M. Suzuki, *Thin Solid Films, 264* (1995) 47.

EXHIBIT 4

Low-Temperature Al$_2$O$_3$ Atomic Layer Deposition

M. D. Groner,[†] F. H. Fabreguette,[†] J. W. Elam,[†] and S. M. George*[,†,‡]

Department of Chemistry and Biochemistry and Department of Chemical Engineering, University of Colorado, Boulder, Colorado 80309-0215

Al$_2$O$_3$ films were deposited by atomic layer deposition (ALD) at temperatures as low as 33 °C in a viscous-flow reactor using alternating exposures of Al(CH$_3$)$_3$ (trimethylaluminum [TMA]) and H$_2$O. Low-temperature Al$_2$O$_3$ ALD films have the potential to coat thermally fragile substrates such as organic, polymeric, or biological materials. The properties of low-temperature Al$_2$O$_3$ ALD films were investigated versus growth temperature by depositing films on Si(100) substrates and quartz crystal microbalance (QCM) sensors. Al$_2$O$_3$ film thicknesses, growth rates, densities, and optical properties were determined using surface profilometry, atomic force microscopy (AFM), QCM, and spectroscopic ellipsometry. Al$_2$O$_3$ film densities were lower at lower deposition temperatures. Al$_2$O$_3$ ALD film densities were 3.0 g/cm^3 at 177 °C and 2.5 g/cm^3 at 33 °C. AFM images showed that Al$_2$O$_3$ ALD films grown at low temperatures were very smooth with a root-mean-squared (RMS) roughness of only 4 ± 1 Å. Current−voltage and capacitance−voltage measurements showed good electrical properties of the low-temperature Al$_2$O$_3$ ALD films. Elemental analysis of the films using forward recoil spectrometry revealed hydrogen concentrations that increased with decreasing growth temperature. No other elements were observed by Rutherford backscattering spectrometry except the parent aluminum and oxygen concentrations. Low-temperature Al$_2$O$_3$ ALD at 58 °C was demonstrated for the first time on a poly(ethylene terephthalate) (PET) polymeric substrate. Al$_2$O$_3$ ALD coatings on PET bottles resulted in reduced CO$_2$ gas permeabilities.

1. Introduction

The coating of thermally fragile substrates by atomic layer deposition (ALD) may provide exciting new applications of ALD in diverse areas ranging from food packaging to microelectronics to biomaterials. For example, thin ALD films may serve as gas diffusion barriers in food packaging and extend shelf life by decreasing oxygen diffusion through potato chip bags or slowing the escape of CO$_2$ from pressurized soda containers.[1,2] ALD coatings on polymers may also be important as gas diffusion barriers for flexible electronic devices or organic light emitting diodes (OLEDs).[3,4] However, few ALD processes have been demonstrated at low temperatures of <100 °C. Room-temperature catalytic SiO$_2$ ALD has been demonstrated with SiCl$_4$ and H$_2$O plus pyridine[5] or NH$_3$[6] as the catalyst. ALD of ZnSe and CdS has also been demonstrated at room

temperature.[7] The vast majority of ALD processes occur at temperatures of >100 °C that would degrade organic, polymeric, or biological material.

Al$_2$O$_3$ is one of the most widely studied materials grown by ALD.[8−17] Al$_2$O$_3$ is a well-behaved ALD system that can be accomplished with a variety of precursors and relatively short cycle times. The effect of growth temperature on the properties of Al$_2$O$_3$ ALD films has been studied at temperatures ranging from 125 to 500 °C.[11−16] For microelectronics applications, desired properties such as high dielectric constant and low impurity concentration have been found to be optimized at a growth temperature of ~350 °C.[11] Little is known about Al$_2$O$_3$ ALD at low temperatures (≤100 °C) and the

* To whom correspondence should be addressed. Phone: 303-492-3398. Fax: 303-492-5894. E-mail: steven.george@colorado.edu.
† Department of Chemistry and Biochemistry.
‡ Department of Chemical Engineering.

(1) Benmalek, M.; Dunlop, H. M. *Surf. Coat. Technol.* **1995**, *77*, 821.
(2) Erlat, A. G.; Spontak, R. J.; Clarke, R. P.; Robinson, T. C.; Haaland, P. D.; Tropsha, Y.; Harvey, N. G.; Vogler, E. A. *J. Phys. Chem. B* **1999**, *103*, 6047.
(3) Burrows, P. E.; Bulovic, V.; Forrest, S. R.; Sapochak, L. S.; McCarty, D. M.; Thompson, M. E. *Appl. Phys. Lett.* **1994**, *65*, 2922.
(4) Weaver, M. S.; Michalski, L. A.; Rajan, K.; Rothman, M. A.; Silvernail, J. A.; Brown, J. J.; Burrows, P. E.; Graff, G. L.; Gross, M. E.; Martin, P. M.; Hall, M.; Mast, E.; Bonham, C.; Bennett, W.; Zumhoff, M. *Appl. Phys. Lett.* **2002**, *81*, 2929.
(5) Klaus, J. W.; Sneh, O.; George, S. M. *Science* **1997**, *278*, 1934.
(6) Klaus, J. W.; George, S. M. *Surf. Sci.* **2000**, *447*, 81.
(7) Luo, Y.; Slater, D.; Han, M.; Moryl, J.; Osgood, R. M. *Appl. Phys. Lett.* **1997**, *71*, 3799.
(8) Ritala, M.; Leskela, M. In *Handbook of Thin Film Materials*, Vol. 1; Nawla, H. S., Ed.; Academic Press: San Diego, CA, 2001.
(9) Ott, A. W.; Klaus, J. W.; Johnson, J. M.; George, S. M. *Thin Solid Films* **1997**, *292*, 135.
(10) Dillon, A. C.; Ott, A. W.; Way, J. D.; George, S. M. *Surf. Sci.* **1995**, *322*, 230.
(11) Groner, M. D.; Elam, J. W.; Fabreguette, F. H.; George, S. M. *Thin Solid Films* **2002**, *413*, 186.
(12) Yun, S. J.; Lee, K.; Skarp, J.; Kim, H.; Nam, K. *J. Vac. Sci. Technol. A* **1997**, *15*, 2993.
(13) Matero, R.; Rahtu, A.; Ritala, M.; Leskela, M.; Sajavaara, T. *Thin Solid Films* **2000**, *368*, 1.
(14) Kukli, K.; Ritala, M.; Leskela, M.; Jokinen, J. *J. Vac. Sci. Technol. A* **1997**, *15*, 2214.
(15) Fan, J.; Sugioka, K.; Toyoda, K. *Jpn. J. Appl. Phys.* **1991**, *30*, L1139.
(16) Drozd, V. E.; Baraban, A. P.; Nikiforova, I. O. *Appl. Surf. Sci.* **1994**, *82/83*, 583.
(17) Elam, J. W.; Groner, M. D.; George, S. M. *Rev. Sci. Instrum.* **2002**, *73*, 2981.
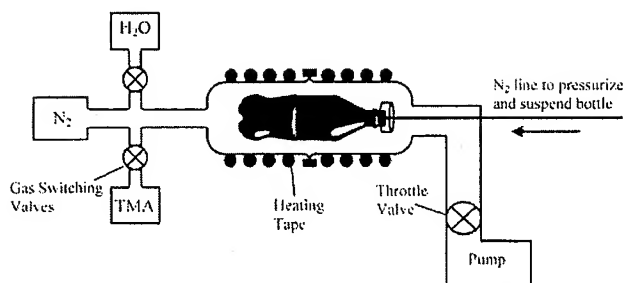
Figure 1. Diagram of the viscous-flow reactor used for low-temperature Al_2O_3 ALD. A special flow tube was employed to accommodate a 510-mL PET bottle. A nitrogen purge line was used to suspend and pressurize the PET bottle during Al_2O_3 ALD.

properties of such films. This study explores the conditions necessary for low-temperature Al_2O_3 ALD and examines the properties of the resulting films. Low-temperature Al_2O_3 ALD was also applied for the first time to a poly(ethylene terephthalate) (PET) polymer substrate. Reduced gas permeabilities were observed for Al_2O_3 ALD-coated PET bottles.
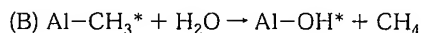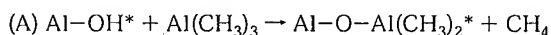
2. Experimental Section

A. Chemicals and Substrates. Al_2O_3 ALD films were grown using H_2O (Fisher, optima grade) and $Al(CH_3)_3$ [trimethylaluminum (TMA)] (Akzo-Nobel, semiconductor grade, 99.9999%). The carrier gas in the viscous flow reactor was N_2 (Airgas, ultrahigh purity). Moderately doped n-type Si(100) wafers from Montco Silicon Technologies, Inc., with a boron doping density of ~2 × 10^{17} cm^{-3} were used as substrates.

A variety of chemicals were used for etching and cleaning of the Si substrates. These chemicals included 5% HF (general chemicals class 10 water/HF (10:1) mix), water (HPLC grade), sulfuric acid, and hydrogen peroxide (30%). Prior to deposition, the silicon wafers were cut into ~2.5 cm × 2.5 cm pieces, cleaned in a ~60 °C Piranha solution for 15 min, and then HF etched for 60 s.

For gas diffusion tests, uncoated poly(ethylene terephthalate) (PET) bottles were supplied by Applied Films Corp. The bottles were 510-mL Coke Contour bottles. These PET bottles had a weight of 28 g and a petalloid shaped base. The PET bottles were cleaned with Micro cleaner/oxide remover (International Products Corp.) prior to deposition.

B. Al_2O_3 ALD Film Growth in Viscous-Flow Reactor. Al_2O_3 films were grown by ALD in a viscous-flow ALD reactor. This reactor has been described in detail in other publications.[11,17] TMA and H_2O were alternately entrained in the N_2 carrier flow using gas switching valves.[17] The N_2 carrier gas pressure was ~1.0 Torr. TMA and H_2O pressure transient increases of ~0.1 Torr were measured by a Baratron when the reactants were introduced into the N_2 carrier flow.

The Al_2O_3 ALD film growth proceeded according to two self-limiting surface reactions. The TMA and H_2O yield Al_2O_3 ALD according to the following two reactions:[9,10]

$$\text{(A)} \quad Al-OH^* + Al(CH_3)_3 \rightarrow Al-O-Al(CH_3)_2^* + CH_4$$

$$\text{(B)} \quad Al-CH_3^* + H_2O \rightarrow Al-OH^* + CH_4$$

where the asterisks denote the surface species. When performed in an ABAB... reaction sequence, these sequential reactions produce linear, atomic-layer controlled Al_2O_3 growth. Many previous studies have confirmed linear and conformal growth using TMA and H_2O.[9,11,15,17]

The standard flow tube was used to deposit Al_2O_3 ALD films on Si substrates or the QCM.[17] Figure 1 shows the reactor with a larger-than-normal flow tube designed to accommodate the PET bottles. Figure 1 also shows a simplified diagram of the

gas switching valves and the gas reservoirs. The gas switching valves allow for a rapid turn-on and shut-off of the reactant gases for short ALD cycle times. This short time is facilitated by pumping the gas reservoirs with separate mechanical pumps after the reactant exposures.[17]

The time for one complete Al_2O_3 ALD cycle ranged from 12 s at 177 °C to 203 s at 33 °C. This cycle time was defined by (t_1, t_2, t_3, t_4) where t_1 is the TMA exposure time, t_2 is the N_2 purge time following the TMA reactant exposure, t_3 is the H_2O exposure time, and t_4 is the N_2 purge time following the H_2O reactant exposure. All times are in units of seconds. Longer purge times were required at lower temperatures to avoid Al_2O_3 chemical vapor deposition (CVD) resulting from insufficient purge times.

Quartz crystal microbalance (QCM) studies of Al_2O_3 ALD were performed in situ using a Maxtek TM400 thin-film deposition monitor. The QCM crystal housing was sealed and purged to prevent deposition on the backside and positioned horizontally in the flow reactor tube. A detailed description of the QCM for monitoring ALD has been presented in a previous publication.[17]

Al_2O_3 ALD films were deposited on PET bottles at 58 °C. To accommodate the 510-mL PET bottles, the standard reactor flow tube was replaced with a larger 10-cm diameter tube as shown in Figure 1. This tube consisted of the bottom halves of two vacuum traps joined by an O-ring and a clamp. The bottles were suspended in this enlarged reactor tube by a custom-made cap and purge line that allowed the bottle to be pressurized with N_2 gas during Al_2O_3 ALD. The pressurization prevented bottle deformation during and after the Al_2O_3 ALD film growth.

C. Al_2O_3 Film Characterization. Al_2O_3 film thicknesses and refractive indices were measured using a J. A. Woollam M44 variable-angle spectroscopic ellipsometer (VASE). Measurements were obtained over the spectral range from 406 to 806 nm using an incidence angle of 75°. Al_2O_3 and SiO_2 have virtually identical optical constants. Consequently, a simple ellipsometric measurement yields only the sum of the Al_2O_3 and SiO_2 film thicknesses. To determine the true Al_2O_3 thickness and the thickness of any interfacial SiO_2 layer on Si(100), a procedure was employed that utilized simultaneous Al_2O_3 ALD growth on both an HF-etched Si wafer and a Si wafer with a native oxide. This procedure was described in detail in another publication.[11] A 13 ± 2 Å thick interfacial SiO_2 layer was determined to be present at the Al_2O_3/Si interface after Al_2O_3 ALD. This SiO_2 thickness was subtracted from the ellipsometric measurements to determine the Al_2O_3 layer thickness.

Atomic force microscope (AFM) images of the Al_2O_3 films and substrates were obtained using an AutoProbe CP Research scanning probe microscope (SPM) instrument from Thermo-Microscopes. RMS surface roughness values were calculated on the basis of 1 μm^2 contact-mode AFM scans. Profilometry was performed using a Dektak 3 surface profile measuring system from Veeco Metrology Group. Al_2O_3 film thicknesses were determined by measuring step heights using profilometry and contact-mode AFM. Well-defined steps needed for AFM imaging were created by masking part of the sample with a small piece of high-temperature aluminum foil tape (3M, Type 433) during Al_2O_3 ALD. Other methods, such as clamping another piece of silicon to the substrate, were found to produce poorly defined steps that were too wide to be imaged by AFM.

Electrical measurements were performed using a MDC 811 mercury probe from the Materials Development Corporation. These electrical measurements have been described in another publication.[11] The mercury probe makes contact to the front surface of the Al_2O_3 films by drawing up a well-defined column of Hg with a surface area of 0.437 mm^2. Current−voltage (IV) measurements were obtained using a Keithley 487 picoammeter/voltage source. Capacitance−voltage (CV) measurements were performed using a Stanford Research Systems SR720 LCR meter. The experiments were computer-controlled using LabView from National Instruments.

Elemental analysis was performed at the Ion Beam Analysis Laboratory in the Institute of Technology Characterization
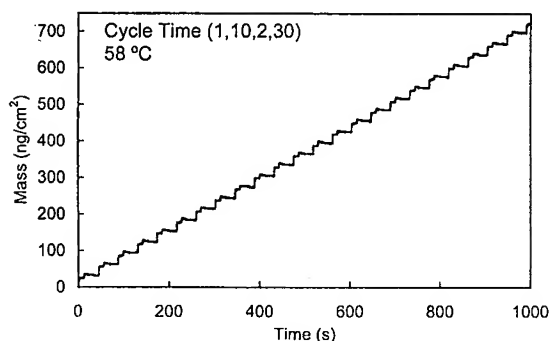
Figure 2. QCM measurements for Al_2O_3 ALD at 58 °C showing the linear growth of the Al_2O_3 ALD film over many reaction cycles. The average Al_2O_3 mass gain per ALD cycle is 30 ng/cm^2.

Facility at the University of Minnesota. Al and O were determined by Rutherford backscattering spectrometry (RBS) using a 3.5 MeV $^4He^{2+}$ and 2.4 MeV $^4He^+$ beam, respectively. H was determined by 1.3 MeV $^4He^+$ forward recoil spectrometry (FReS). The instrument is composed of a NEC 1.7 MV Pelletron accelerator with a Charles Evans RBS 400 endstation. The He beam incident angle was 75°. The RBS detector was located at 165° and the FReS detector was located at 30° from the beam direction. A 5-μm- thick Mylar foil was placed in front of the FReS detector to filter the scattered ^4He particles. The error was estimated at less than 5%.

X-ray reflectivity (XRR) was performed with a Bede Scientific Ltd. D1 System using a channel cut crystal. The X-ray wavelength from the Cu Kα X-ray tube was 1.54 Å. The electron beam current in the X-ray tube was 20 mA at 35 kV. A *0-20* scan was performed with a 10-arcsec step size and a 5-s acquisition time. The Bede Refs software with a genetic algorithm was used to fit the XRR data and calculate the densities of the films.

Gas diffusion tests on the Al_2O_3 ALD-coated PET bottles were performed by Applied Films Corporation using a GMS barrier measurement system (Balzers Process Systems, GmbH). The bottles were pressurized with up to 6 bar of CO_2 gas. The loss of CO_2 was then measured over 3 to 4 days. The CO_2 loss rate of an Al_2O_3 ALD-coated PET coated bottle was compared with the CO_2 loss rate of an uncoated bottle. This ratio of these loss rates determined the CO_2 barrier improvement factor (BIF).

3. Results

A. Quartz Crystal Microbalance. Al_2O_3 ALD was characterized at different growth temperatures from 33 to 177 °C using a QCM. Figure 2 shows Al_2O_3 ALD at 58 °C using a (1, 10, 2, 30) cycle time. The Al_2O_3 ALD film growth is very linear with number of AB reaction cycles. A mass gain per cycle of 30 ng/cm^2 was measured for the Al_2O_3 ALD growth shown in Figure 2. A more detailed view of the QCM data is shown in Figure 3. The QCM data for three ALD cycles shows the mass gain for each TMA and water exposure. The time periods during which the TMA and H_2O dosing valves were open are denoted by the shaded regions. A larger mass gain is observed during the TMA exposure than during the H_2O exposure. This behavior is similar to that previously observed during QCM studies of Al_2O_3 ALD at 177 °C.[17]

The QCM data were used to determine the optimal reactant exposures and nitrogen purge times for Al_2O_3 ALD at low temperatures. At 177 °C, QCM data from this work and a previous study[17] showed that 1-s exposure times and 5-s purge times were sufficient for
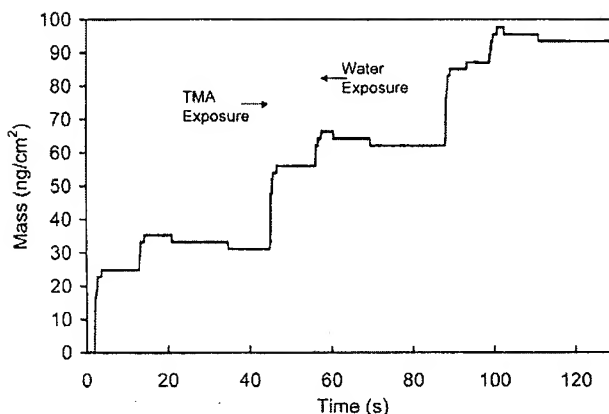

Figure 3. Detailed view of the QCM measurements at 58 °C. The shaded areas show the time periods during which the TMA and water dosing valves were open. The mass increases coincide with the TMA and water exposures.
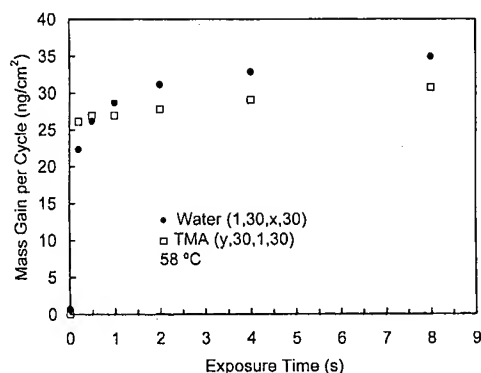

Figure 4. Al_2O_3 mass gain per cycle versus reactant exposure time at 58 °C. Purge times for both TMA and water were 30 s each. The exposure time of the reactant not being investigated was held constant at 1 s.

complete reaction and purging of all of the reactants to prevent CVD. Both the required exposure times and purge times increased with decreasing temperatures.

The dependence of the Al_2O_3 ALD mass gain on reactant exposure time at 58 °C is shown in Figure 4. These curves were obtained by monitoring QCM data while varying the individual reactant exposure times to determine the minimum precursor exposures necessary for the TMA and H_2O reactions to reach completion. Figure 5 shows the effect of purge times on the Al_2O_3 ALD growth rates. Purge times were chosen to be long enough to avoid reactant mixing and subsequent CVD. The CVD growth is indicated by the rise in mass gain per cycle at short purge times. On the basis of these studies, the optimal cycle time for Al_2O_3 ALD growth at 58 °C was (1, 10, 2, 30) where all times are in units of seconds.

QCM experiments confirmed that Al_2O_3 ALD is possible at temperatures as low as 33 °C. This temperature was the lowest temperature that could be achieved without actively cooling the viscous flow reactor. However, the required H_2O purge time was 180 s at 33 °C. Table 1 shows the reactant exposure and purge times used to perform Al_2O_3 ALD at growth temperatures ranging from 33 to 177 °C. The resulting Al_2O_3 ALD mass gains per cycle determined by the QCM are also given in Table 1.
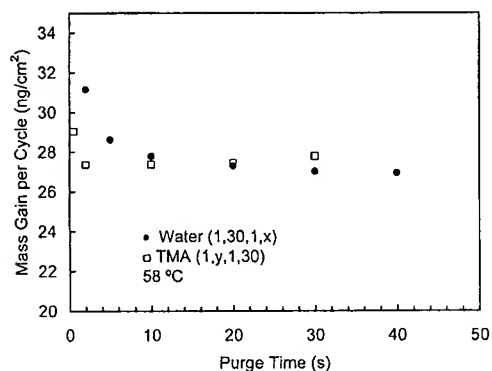
Figure 5. Al_2O_3 mass gain per cycle versus purge time at 58 °C. Exposure times for both TMA and water were 1 s each. The purge time of the reactant not being investigated was held constant at 30 s.

Table 1. Reactant Exposure Times, Purge Times, and Mass Gain Per Cycle Determined by the QCM for Al_2O_3 ALD Films Grown at Temperatures from 33 to 177 °C

	growth temperature (°C)					
	177	125	102	80	58	33
TMA exposure time (s)	1	1	1	1	1	1
purge time (s)	5	5	5	5	10	20
water exposure time (s)	1	2	2	2	2	2
purge time (s)	5	10	20	20	30	180
mass gain/cycle (ng/cm²)	38	39	36	34	30	28

QCM measurements indicated a maximum mass gain per cycle of 39 ng/cm^2 at 125 °C. A slight decrease to 38 ng/cm^2 in the mass gain per cycle was measured at 177 °C. Below 125 °C, the mass gain per cycle decreases with decreasing growth temperature and reaches a value of 30 ng/cm^2 at 33 °C.

B. Spectroscopic Ellipsometry. Al_2O_3 ALD film thicknesses and the refractive index, n, were determined at wavelengths from 406 to 806 nm using spectroscopic ellipsometry. For Al_2O_3 films grown using 300 reaction cycles, the film thickness increased from 332 Å at 33 °C to 401 Å at 125 °C. The film thickness then decreased slightly to 375 Å at 177 °C. These measurements yield Al_2O_3 ALD growth rates of 1.11, 1.34, and 1.25 Å/cycle, respectively. Al_2O_3 ALD growth rates over the entire growth temperature range are given in Figure 6.

The refractive indices decreased slightly with decreasing growth temperature. The results of these measurements are also shown in Figure 6. The refractive indices varied by <1% over the spectral range from 406 to 806 nm. Consequently, the analysis was performed by assuming that the refractive index was constant over the entire wavelength range. The maximum refractive index was $n = 1.60$ at 177 °C. The refractive index decreased to $n = 1.51$ at 33 °C. Figure 6 also shows the density of the Al_2O_3 ALD films calculated on the basis of the QCM mass measurements and the ellipsometric Al_2O_3 film thicknesses.

C. Profilometry, Atomic Force Microscopy, and X-ray Reflectivity. Profilometry and AFM were used as independent measures of Al_2O_3 ALD film thicknesses. Figure 7 shows a 10 × 10 μm^2 AFM image used to determine the thickness of an Al_2O_3 ALD film grown at 58 °C using 300 reaction cycles on a Si(100) substrate. The step was created by covering part of the sample with high-temperature aluminum tape during Al_2O_3
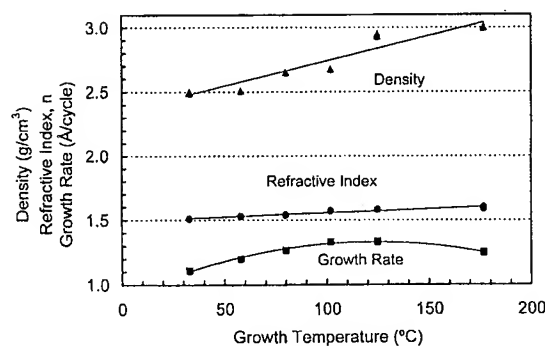

Figure 6. Ellipsometry data for Al_2O_3 ALD films grown using 300 reaction cycles on Si(100) substrates. The refractive index, growth rate, and density (calculated using ellipsometry and QCM data) are plotted versus growth temperatures from 33 to 177 °C.
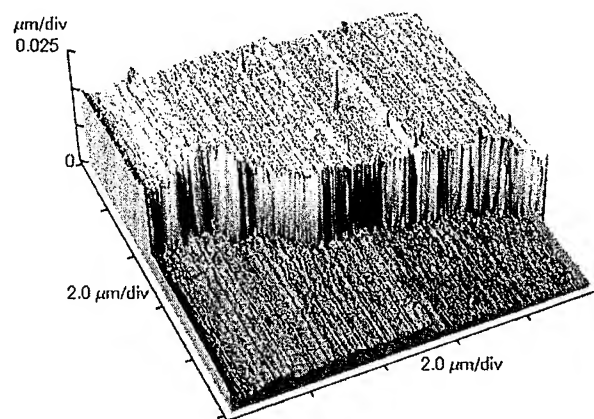

Figure 7. AFM image (10 × 10 μm^2) used to determine the thickness of an Al_2O_3 ALD film grown at 58 °C using 300 ALD cycles on a Si(100) substrate. The step was created by masking part of the sample with aluminum tape during Al_2O_3 ALD. The average step height is 43 nm.

ALD. The average step height in this image is 43 nm. Film thicknesses determined by profilometry and AFM were within ±10% of the thicknesses derived by the ellipsometric measurements.

AFM was also used to determine the surface roughness of the Al_2O_3 ALD films. The low-temperature Al_2O_3 ALD films were all very smooth. The root-mean-squared (RMS) surface roughness for a 1 × 1 μm^2 area averaged 4 ± 1 Å. Growth temperature did not affect this surface roughness. The roughness of these films is also similar to that of Al_2O_3 ALD films grown at higher temperatures.[9,18]

XRR scans for Al_2O_3 ALD films grown on Si(100) using 300 reaction cycles at temperatures from 33 to 177 °C are shown in Figure 8. The XRR scans were fitted to determine densities of the Al_2O_3 ALD films. These fits are also shown in Figure 8. The density of the Al_2O_3 ALD films derived by fitting the XRR measurements decreased from 3.06 g/cm^3 at 177 °C to 2.46 g/cm^3 at 33 °C. The XRR density results and comparison of all the density results are shown in Figure 9.

D. Electrical Characterization. Current–voltage (IV) and capacitance–voltage (CV) measurements were performed on the low-temperature Al_2O_3 ALD films. The
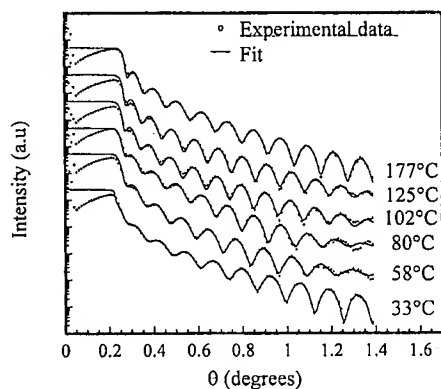
(18) Elam, J. W.; Sechrist, Z. A.; George, S. M. *Thin Solid Films* **2002**, *414*, 43.

Figure 8. XRR scans for Al_2O_3 ALD films grown on Si(100) using 300 reaction cycles versus growth temperature from 33 to 177 °C. The fits to the XRR data used to determine densities are shown by the solid lines.
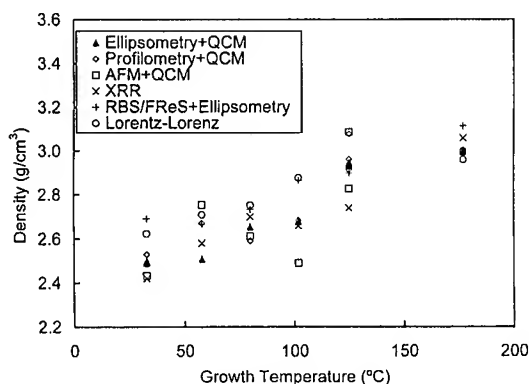

Figure 9. Density of Al_2O_3 ALD films versus growth temperature from 33 to 177 °C for the various methods.
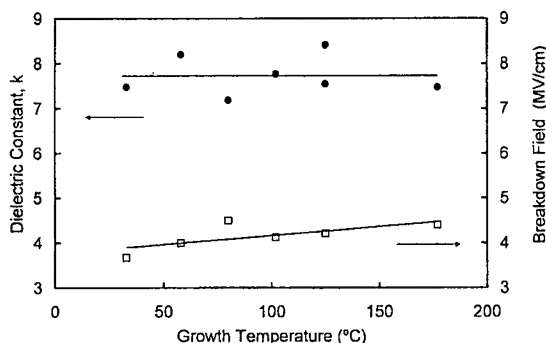

Figure 10. Electrical properties of low-temperature Al_2O_3 ALD films grown using 300 reaction cycles on *n*-Si(100).

IV curve characteristics remained relatively constant versus growth temperature. Low leakage current densities of $<10^{-7}$ nA/cm² at a 5 V bias were measured even for Al_2O_3 ALD films grown at 33 °C. Growth temperature did not appear to affect the leakage currents.

The catastrophic breakdown field decreased slightly with decreasing growth temperature as shown in Figure 10. The breakdown field was 4.4 MV/cm at 177 °C and decreased to 3.7 MV/cm at 33 °C. In addition, there was a decrease in the percentage of spots tested that exhibited good insulating behavior at lower growth temperatures. Capacitance measurements revealed no observable trend versus growth temperature. Figure 10 reveals that the dielectric constants of the Al_2O_3 ALD
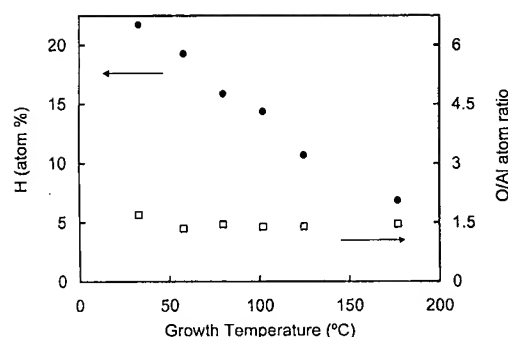

Figure 11. O/Al ratio and H concentrations for Al_2O_3 ALD films as determined by RBS and FReS versus growth temperatures from 33 to 177 °C.

films averaged $k = 7.7\pm0.4$ over the entire temperature range.

E. Elemental Analysis. Rutherford backscattering spectrometry (RBS) analysis measured O/Al ratios close to the expected 1.5 value as shown in Figure 11. The ratios ranged from 1.34 to 1.70. There was no systematic trend with growth temperature. Hydrogen concentrations measured by forward recoil spectrometry (FReS) increased with decreasing growth temperature as displayed in Figure 11. The H atom % in the Al_2O_3 ALD films increased from 6.9% at 177 °C to 21.7% at 33 °C. No other impurities were detected in the Al_2O_3 ALD films within the detection limit of the RBS.

F. Gas Diffusion. Gas diffusion tests with CO_2 were carried out on PET bottles coated with Al_2O_3 ALD films. Bottles were coated with 300 reaction cycles of Al_2O_3 ALD at 58 °C. This coating procedure should deposit a Al_2O_3 ALD film with a thickness of 360 Å. The CO_2 gas diffusion test revealed a CO_2 loss rate of 1.55% per week, or 2.91 cm³/(day bar cm²). This CO_2 loss rate for the Al_2O_3 ALD-coated bottle is a factor of ~1.6 lower than the CO_2 loss rate of an uncoated PET bottle. The ratio of these two CO_2 loss rates yields a barrier improvement factor (BIF) of ~1.6.

Volumetric measurements of the PET bottles showed no change in volume as a result of Al_2O_3 ALD at 58 °C. PET bottles were also coated with 282 and 470 reaction cycles of Al_2O_3 ALD at a growth temperature of 80 °C and without the N_2 gas pressurization. These PET bottles deformed and increased in volume during deposition. The barrier improvements factors for these Al_2O_3 ALD-coated PET bottles were much smaller.

4. Discussion

A. Quartz Crystal Microbalance (QCM) Measurements. QCM studies showed that both the reactant exposure times and the nitrogen purge times required for Al_2O_3 ALD increased with decreasing temperatures. Longer reactant exposures at low temperatures are expected because the reaction is thermally activated.[10] The purging of reactants, especially H_2O, takes longer at low temperatures because of slower desorption of H_2O from the reactor walls at lower temperatures.

The completion of the reactions took longer and became less defined, or "softer", at lower temperatures. This "soft" saturation is revealed by the small slope for the mass gain per cycle versus TMA and H_2O exposure at longer exposure times in Figure 4. These small slopes

644 *Chem. Mater., Vol. 16, No. 4, 2004*

Groner et al.

indicate that either a complete reaction may not have been achieved or that the purge times may have become insufficient. Unfortunately, trying to achieve a complete reaction using reactant exposures of tens of seconds is inefficient in terms of time and reactant usage.

The maximum QCM mass gain per cycle of 39 ng/cm^2 was recorded at 125 °C as shown in Table 1. QCM measurements can be employed to calculate film thicknesses. These thickness calculations rely on known density values. For amorphous materials such as the Al$_2$O$_3$ ALD films grown at low temperatures, the density may change with growth temperature. Consequently, additional independent thickness measurements are required to derive the density from the QCM mass measurements.

B. Thickness Measurements and Al$_2$O$_3$ ALD Growth Rates. The agreement between the different methods of measuring Al$_2$O$_3$ ALD film thicknesses is quite good. Ellipsometric data exhibit less scatter than most of the other methods. The growth rate versus growth temperature obtained by ellipsometry displays a very smooth dependence in Figure 6. However, ellipsometry data depend on fitting several parameters to obtain a film thickness. This modeling can also be complicated by the presence of an interfacial SiO$_2$ layer.[11] Profilometry and AFM step height measurements are more direct determinations of film thickness but tend to be less precise. These measurements depend on the presence of a well-defined, sharp step edge that is not always easy to obtain. However, the film thicknesses obtained by profilometry and AFM agreed fairly well with the film thicknesses obtained by ellipsometry and XRR methods.

The Al$_2$O$_3$ ALD growth rates shown in Figure 6 reach a maximum of 1.33 Å/cycle at 100 and 125 °C. A previous study observed the maximum Al$_2$O$_3$ ALD growth rate of 1.1 Å/cycle at 177 °C.[9] The position of this maximum was explained by the thermal activation required for the reaction at lower temperatures and decreasing Al–OH and Al–CH$_3$ surface coverages at higher temperatures.[9] The growth rate is determined by reaction kinetics and necessary surface species.[9,10] There are higher surface coverages at low temperatures, but slower reaction kinetics because of the thermal activation barrier. The reaction kinetics are more rapid at higher temperatures, but the growth rate is limited by the lower surface coverages.

C. Density. Figure 9 shows the densities of the Al$_2$O$_3$ ALD films as determined by a number of different methods. Densities were calculated on the basis of QCM, AFM, ellipsometry, profilometry, XRR, and RBS/FReS data. The density of the Al$_2$O$_3$ ALD films decreased with decreasing growth temperature based on all the different methods. Furthermore, the density values derived from the different methods agree fairly well with each other. Average densities ranged from 3.0 g/cm^3 at 177 °C to 2.5 g/cm^3 at 33 °C.

The densities of these low-temperature Al$_2$O$_3$ ALD films are significantly lower than the 3.5–3.7 g/cm^3 value typically reported for amorphous Al$_2$O$_3$.[19,20] The
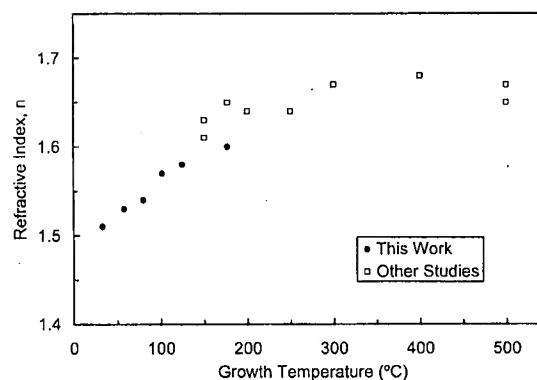

Figure 12. Refractive index, *n*, of the Al$_2$O$_3$ ALD films versus growth temperature from 33 to 177 °C and comparisons to results from other Al$_2$O$_3$ ALD studies at higher temperatures.[9,12–15,21]

density of 3.0 g/cm^3 at 177 °C is also lower than the density of 3.5 g/cm^3 derived in a previous study of Al$_2$O$_3$ ALD films.[9] That earlier study derived the density from the refractive index of the film and the Lorentz–Lorenz relationship assuming the optical constants of crystalline Al$_2$O$_3$. This assumption may not be correct because the Al$_2$O$_3$ ALD film is amorphous. The data in the current study are consistent with an average density of 3.0 g/cm^3 at 177 °C based on many different types of measurements.

The density versus growth temperature has also been calculated using the Lorentz–Lorenz relationship.[9] Starting with the density of 3.0 g/cm^3 at 177 °C, densities for the Al$_2$O$_3$ ALD films grown at lower temperature were determined on the basis of their refractive indices, *n*. Figure 9 shows that the densities derived using the Lorentz–Lorenz relationship yield good agreement with the other Al$_2$O$_3$ ALD film densities.

D. Optical and Electrical Properties. Figure 6 shows that the refractive index of the Al$_2$O$_3$ ALD films decreased slightly with decreasing growth temperatures. This trend has been reported elsewhere and was attributed to decreased density and to increased impurity levels in films grown at lower temperatures.[8,14] Figure 12 shows the refractive index of the low-temperature Al$_2$O$_3$ ALD films compared with the refractive index of Al$_2$O$_3$ ALD films measured in other studies.[9,12–15,21] There is good agreement between the refractive indices in the region of overlap between 150 and 200 °C.

The refractive index increases with increasing growth temperature up to ~300 °C. The refractive index is then constant at *n* ≈ 1.67 for growth temperatures between 300 and 500 °C. For comparison, the crystalline α-Al$_2$O$_3$ sapphire form of alumina has a refractive index of *n* = 1.76.[15] This comparison indicates that the amorphous Al$_2$O$_3$ ALD film with *n* ≈ 1.67 will densify further upon crystallization. This densification could lead to tensile stress and film cracking.

IV and CV measurements revealed good electrical properties for films grown at low temperatures. The decreasing breakdown field with decreasing growth temperature shown in Figure 10 may result from the decreasing density or the increased hydrogen concentra-

(19) Grey, D. E., Coord. Ed. *American Institute of Physics Handbook*; American Institute of Physics: New York, 1982.

(20) Weast, R. C., Ed. *CRC Handbook of Chemistry and Physics*; CRC Press: Boca Raton, FL, 1983–84.

(21) Kattelus, H.; Ylilammi, M.; Saarilahti, J.; Antson, J.; Lindfors, S. *Thin Solid Films* **1993**, *225*, 296.

tion in the Al_2O_3 ALD films grown at lower temperatures. Figure 10 also shows that the dielectric constant did not decrease with decreasing growth temperatures. However, the scatter in the measurements may have masked a small change.

E. Film Composition. The RBS analysis of the Al_2O_3 ALD films obtained O/Al ratios close to the expected ratio of 1.5. In addition, FReS analysis revealed hydrogen concentrations in Figure 11 that increased with decreasing growth temperatures. The increasing hydrogen concentrations continue a trend that was observed in a previous study for Al_2O_3 ALD growth temperatures from 350 to 125 °C.[11] The increasing hydrogen concentration at low temperatures may be directly related to the lower density of the Al_2O_3 ALD films at lower growth temperature.

At lower temperatures, the hydroxyl surface coverage is higher on Al_2O_3 surfaces.[9,10] In addition, the TMA reaction with the Al−OH surface species groups does not go to completion at low temperatures.[9,10] During Al_2O_3 ALD, the hydroxyl species can build up in the growing Al_2O_3 film. At 180 °C, the hydroxyl concentration in the film after 10 AB cycles is equal to approximately the full hydroxyl coverage.[10] Annealing at 1000 K can reduce hydroxyl accumulation in Al_2O_3 ALD films.[10] These previous studies support the idea that the H atoms in the low-temperature Al_2O_3 ALD films are present in the form of Al−OH species.

Despite the high hydrogen concentrations at low temperatures, the Al_2O_3 ALD films still exhibited remarkably good properties. Low-temperature Al_2O_3 ALD films may be used for various applications where the high hydrogen concentration is not crucial. On the basis of the results at 33 °C, growing Al_2O_3 ALD films at room temperature is possible. The major problem is slow H_2O desorption from the reactor walls and very long required H_2O purge times. Shorter cycle times could be achieved using a modified reactor design and alternate oxygen sources such as N_2O,[22] NO_2,[16] or alkoxides.[23]

F. Gas Diffusion Tests. The PET bottles coated with 300 reaction cycles of Al_2O_3 ALD at 58 °C displayed a decrease in CO_2 gas diffusion rates. However, lower CO_2 diffusion rates and higher barrier improvement factors

(BIF) are desired for commercial applications. Light microscopy images of the surface of the PET bottle revealed apparent scratches and/or cracks on the surface of the Al_2O_3 ALD-coated bottles. These scratches and/or cracks may explain the low BIF for these Al_2O_3 ALD films compared with typical BIFs for SiO_2 coatings.[24]

5. Conclusions

Al_2O_3 ALD growth has been demonstrated at temperatures as low as 33 °C. Many of the properties of these low-temperature Al_2O_3 ALD films were comparable with the properties of Al_2O_3 ALD films grown at higher temperatures of ≥177 °C. The low-temperature Al_2O_3 ALD films exhibited very low surface roughness values, low leakage currents, high dielectric constants, and growth rates in excess of 1 Å/cycle. Good thin film properties were observed despite decreasing densities and increasing hydrogen concentrations observed at lower temperatures. Increased ALD cycle times were necessary at lower temperatures because of the slower reaction rates and longer required purge times for the H_2O reactant. Improvements in reactor design and the use of alternate oxygen sources could help overcome this problem. Low-temperature Al_2O_3 ALD may have applications for coating thermally fragile substrates such as organic, polymeric, or biological material. As a demonstration of the possible applications, low-temperature Al_2O_3 ALD films were grown on PET bottles to reduce gas diffusion. The Al_2O_3 ALD-coated PET bottles displayed lower CO_2 gas diffusion rates than uncoated PET bottles.

(22) Kumagai, H.; Toyoda, K.; Matsumoto, M.; Obara, M. *Jpn. J. Appl. Phys.* **1993**, *32*, 6137.
(23) Ritala, M.; Kukli, K.; Rahtu, A.; Raisanen, P. I.; Leskela, M.; Sajavaara, T.; Keinonen, J. *Science* **2000**, *288*, 319.

(24) Chatham, H. *Surf. Coat. Technol.* **1996**, *78*, 1.

EXHIBIT 5

Quartz Crystal Microbalance Studies of Al$_2$O$_3$ Atomic Layer Deposition Using Trimethylaluminum and Water at 125 °C[†]

R. A. Wind[⊥,‡] and S. M. George[*,‡,§]

Department of Chemistry and Biochemistry, Department of Chemical and Biological Engineering, University of Colorado, Boulder, Colorado 80309-0215
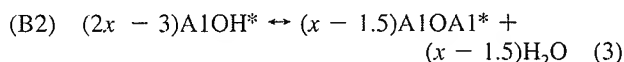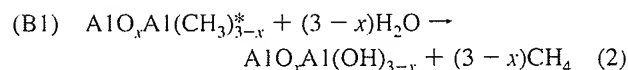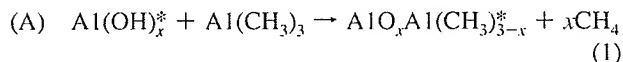
Al$_2$O$_3$ atomic layer deposition (ALD) growth with Al(CH$_3$)$_3$ (trimethylaluminum (TMA)) and H$_2$O as the reactants was examined at the relatively low temperature of 125 °C using quartz crystal microbalance (QCM) measurements. The total Al$_2$O$_3$ ALD mass gain per cycle (MGPC) and MGPCs during the individual TMA and H$_2$O reactions were measured versus TMA and H$_2$O exposures. The Al$_2$O$_3$ MGPC increased with increasing H$_2$O and TMA exposures at fixed TMA and H$_2$O exposures, respectively. However, the TMA and H$_2$O reactions were not completely self-limiting. The slower surface reaction kinetics at lower temperature may require very long exposures for the reactions to reach completion. The Al$_2$O$_3$ MGPCs increased quickly versus H$_2$O exposure and slowly reached limiting values that were only weakly dependent on the TMA doses. Small TMA exposures were also sufficient for the Al$_2$O$_3$ MGPCs to reach different limiting values for different H$_2$O doses. The TMA MGPCs increased for higher TMA exposures at all H$_2$O exposures. In contrast, the H$_2$O MGPCs decreased for higher TMA exposures at all H$_2$O exposures. This decrease may occur from more dehydroxylation at larger hydroxyl coverages after the H$_2$O exposures. The hydroxyl coverage after the H$_2$O exposure was dependent only on the H$_2$O exposure. The Al$_2$O$_3$ MGPC was also linearly dependent on the hydroxyl coverage after the H$_2$O dose. Both the observed hydroxyl coverage versus H$_2$O exposure and the Al$_2$O$_3$ ALD growth versus H$_2$O and TMA exposures were fit using modified Langmuir adsorption isotherm expressions where the pressures are replaced with exposures. These results should be useful for understanding low-temperature Al$_2$O$_3$ ALD, which is important for coating organic, polymeric, and biological substrates.

1. Introduction

Atomic layer deposition (ALD) is a thin film deposition technique that can fabricate ultrathin, continuous, and conformal films on very complex shapes. ALD is based on two sequential, self-limiting surface reactions.[1,2] Al$_2$O$_3$ ALD is one of the most widely investigated ALD systems.[3−12] Al$_2$O$_3$ ALD typically utilizes Al(CH$_3$)$_3$ (trimethylaluminum (TMA)) and H$_2$O as reactants.[13,14] The growth is nearly self-limiting for temperatures of 30−300 °C, no residual carbon is incorporated into the film, and the only reaction byproduct is CH$_4$. Al$_2$O$_3$ ALD displays almost all the requirements for ideal ALD.

The surface chemistry of the binary reaction sequence during Al$_2$O$_3$ ALD can be described as[12,15]

$$\text{(A)} \quad \text{Al(OH)}_x^* + \text{Al(CH}_3)_3 \rightarrow \text{AlO}_x\text{Al(CH}_3)_{3-x}^* + x\text{CH}_4 \quad (1)$$

$$\text{(B1)} \quad \text{AlO}_x\text{Al(CH}_3)_{3-x}^* + (3-x)\text{H}_2\text{O} \rightarrow \text{AlO}_x\text{Al(OH)}_{3-x} + (3-x)\text{CH}_4 \quad (2)$$

$$\text{(B2)} \quad (2x - 3)\text{AlOH}^* \leftrightarrow (x - 1.5)\text{AlOAl}^* + (x - 1.5)\text{H}_2\text{O} \quad (3)$$

where the asterisks indicate the surface species. These equations are written for one Al site for steady-state Al$_2$O$_3$ ALD growth. One Al atom is deposited during each reaction cycle.

The reaction of TMA with surface OH* (hydroxyl) species is given by reaction A in eq 1. x is the number of OH* species per Al site that react with each TMA molecule. The H$_2$O reaction occurs by direct replacement of CH$_3^*$ (methyl) species with OH* species, as indicated by reaction B1 in eq 2. Stoichiometric Al$_2$O$_3$ is produced by only reactions A and B1 when $x = 1.5$. Reaction B2 in eq 3 is required to maintain stoichiometric Al$_2$O$_3$ if $x > 1.5$ or $x < 1.5$. When $x > 1.5$, AlOH* species undergo dehydroxylation to produce H$_2$O. When $x < 1.5$, H$_2$O dissociatively adsorbs on a dehydroxylated AlOAl* site to produce AlOH* species. Reaction B2 in eq 3 runs in reverse when $x < 1.5$.

Confirmation of these surface reactions is provided by Fourier transform infrared (FTIR) spectroscopy.[3−5] quartz crystal microbalance (QCM),[12,16] and quadrupole mass spectrometry (QMS)[8,12] studies. FTIR spectroscopy monitors the OH* and CH$_3^*$ surface species and their interconversion during the TMA and H$_2$O reactions.[3−5] QCM measures the mass change during the TMA and H$_2$O reactions.[12,16] QMS observes the production of CH$_4$ as the primary gas phase reaction products.[8,12] The surface reactions have also been shown to be self-limiting.[3,9] Self-limiting growth allows ALD to produce conformal and atomically flat films on spatially complex substrates.[4,17,18] The
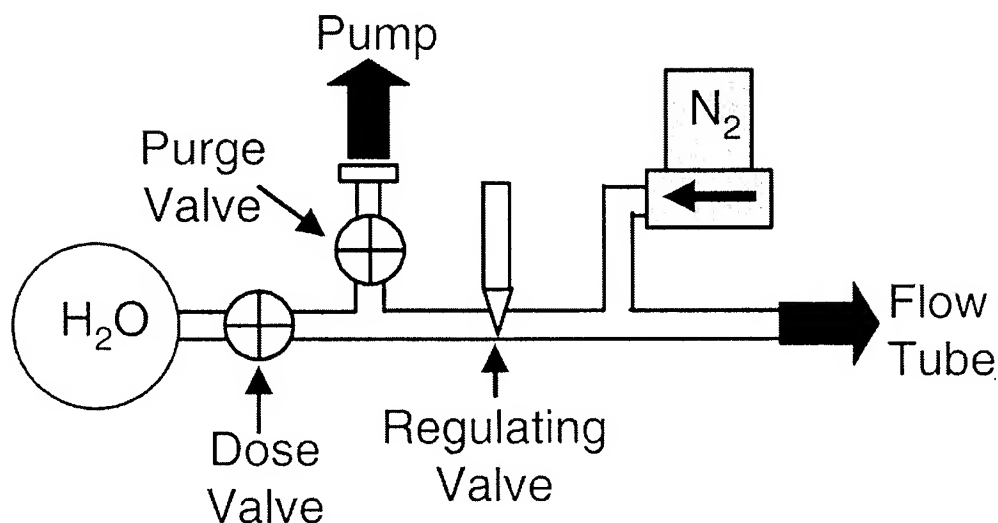
Figure 1. Diagram of the gas switching valves used for H_2O dosing.

Al_2O_3 ALD reaction is also able to initiate Al_2O_3 growth on a wide variety of surfaces, including oxides, nitrides, metals, semiconductors, and polymers.[4-6,19]

The thermochemistry of Al_2O_3 ALD is very favorable. The heat of reaction for $2Al(CH_3)_3 + 3H_2O \rightarrow Al_2O_3 + 6CH_4$ is -376 kcal.[20] This large exothermicity helps enable Al_2O_3 ALD at low temperatures. Al_2O_3 ALD is operative at temperatures as low as 33 °C.[7] Investigations have shown that Al_2O_3 ALD yields very well-defined films from 33 to 177 °C.[7] The low temperatures have allowed Al_2O_3 ALD to deposit on a range of thermally fragile substrates, such as organic, polymeric, and biological substrates.[7,19,21,22] These low-temperature Al_2O_3 ALD films are particularly useful for gas diffusion barriers on polymer substrates.[23-25]

Because of the importance of low-temperature Al_2O_3 ALD, this paper explores the dependence of Al_2O_3 ALD on H_2O and TMA exposures at 125 °C. These investigations are conducted using QCM studies. The total Al_2O_3 ALD mass gain per cycle (MGPC) is examined versus H_2O and TMA exposures. The separate MGPCs after the H_2O and TMA doses are also explored versus the H_2O and TMA exposures. The MGPCs provide information on the coverage of the OH* and CH₃* surface species and the deposited Al coverage per cycle during Al_2O_3 ALD. Modified Langmuir adsorption isotherm expressions are also used to fit the hydroxyl coverage versus H_2O exposures and Al_2O_3 ALD growth versus H_2O and TMA exposures.

2. Experimental Section

The viscous-flow ALD reactor used in this study has been described in detail previously.[15,16] Briefly, TMA and H_2O are alternately entrained in a N_2 flow by operating gas switching valves. Each reactant enters the reaction zone through a separate 1/4″ stainless steel tube. Figure 1 shows a diagram of the gas switching valves for the H_2O line. During the purge step, most of the 40 sccm of N_2 entering the line flows into the reaction zone. The remaining N_2 is diverted through the regulating valve and purges the small reservoir to a separate pump. During the dose step, the purge valve is closed while the dose valve is opened. H_2O rapidly fills the reservoir before entering the N_2 gas stream through the regulating valve. The dose valve is closed while the purge valve is opened after the set dose time. In this manner, the gas switching valves allow for the rapid turn-on and shut-off of the reactant gases.[16] The TMA gas switching valves are configured in an identical fashion.

The reaction zone consists of a 3.5-cm-diameter flow tube divided into two externally heated zones. The temperatures of each zone were monitored with chromel-alumel thermocouples attached to the outside of the flow tube under the heaters. The temperatures were maintained using PID controllers. The first zone consists of a 15-cm-long preheating zone that was operated at 132 ± 0.5 °C. This zone preheated the N_2 and the reactant gases before they entered the reaction zone. This preheating prevented temperature-induced fluctuations in the QCM signal due to cool reactants entering the flow tube.[26]

The second zone was a 30-cm-long reaction zone that was operated at a temperature of 125 ± 0.5 °C. A Baratron pressure manometer was positioned just behind the reaction zone and monitored the reactor pressure. A total N_2 flow of 200 sccm used in these experiments produced a measured pressure of ~1 Torr. A QCM inside a custom holder was placed inside the reaction zone. The back side of the crystal was purged with nitrogen to prevent back-side deposition.[16] This back-side purge added ~0.1 Torr of N_2 pressure to the total nitrogen pressure. An integral thermocouple showed that the QCM temperature during these experiments was 121.9 ± 0.1 °C.

The QCM crystals were AT-cut, 6 MHz quartz crystal with a special low-roughness surface polish. Prior to making any measurements, ~500 Å of Al_2O_3 ALD was deposited on the QCM crystals to create a reproducible starting surface. A Maxtek TM400 deposition monitor was used to control and monitor the QCM crystal. The resolution of the TM400 mass signal is limited to ~2 ng/cm² due to an apparent rounding error. This rounding error does not affect the TM400 digital output of the period of the QCM crystal.

The period of the QCM crystal was recorded at 100 ms intervals by a personal computer running Labview software. Assuming the acoustic impedance of the deposited film is equal to the acoustic impedance of an AT-cut crystal (i.e., 8.83×10^5 g cm⁻² s⁻¹), the mass deposited per unit area, m, equals[27]

$$m = N_q \cdot \rho_q \cdot \Delta\tau \qquad (4)$$

In this equation, $N_q = 1.668 \times 10^5$ Hz-cm is the frequency constant for an AT-cut crystal, $\rho_q = 2.649$ g/cm³ is the density of the AT-cut crystal,[28] and $\Delta\tau$ is the change in the period. Using eq 4 and the output of the TM400, the mass resolution is ~0.137 ng/cm². The assumption that the acoustic impedance of Al_2O_3
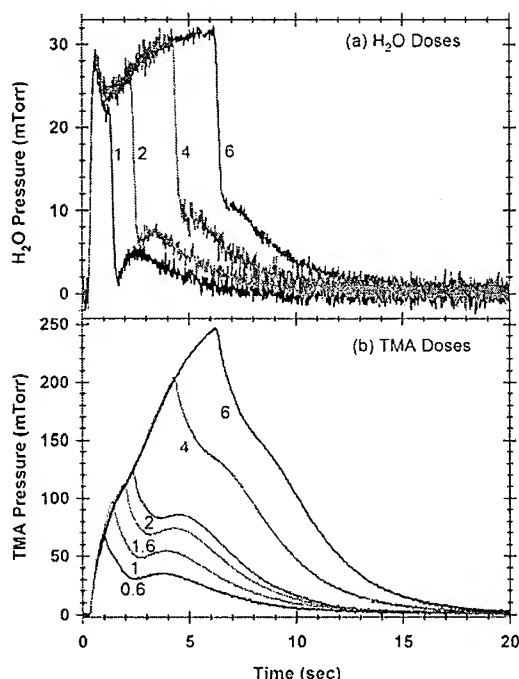
Al$_2$O$_3$ Atomic Layer Deposition

J. Phys. Chem. A, Vol. 114, No. 3, 2010 **1283**

Figure 2. Pressure profiles measured by a capacitance manometer for (a) H$_2$O and (b) TMA dosing during Al$_2$O$_3$ ALD at 125 °C. Pressure profiles are shown for different dosing times in seconds. These pressure profiles were recorded after the surface reactions had reached completion.
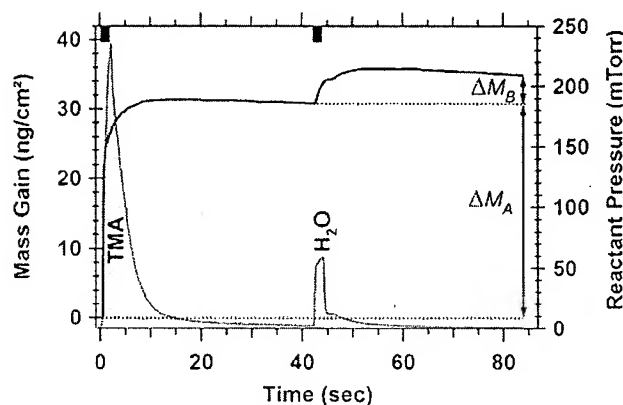

Figure 3. QCM mass gain measured during Al$_2$O$_3$ ALD at 125 °C with TMA and H$_2$O dose times of 2 s indicated by the black bars at the top of the plot. Mass gains during the TMA and H$_2$O exposures are ΔM_A and ΔM_B, respectively. Solid gray areas show pressure profiles.

ALD equals the acoustic impedance of quartz will lead to an error; however, for a 1% frequency shift, the error in the mass is <2%.[28] The crystal was replaced when the frequency changed by 1% relative to the starting frequency.

Al$_2$O$_3$ ALD films were deposited using alternating exposures of H$_2$O (Fisher, Optima) and TMA (Strem, 98+%). The reactants were maintained at room temperature. These conditions provided vapor pressures of ~20 Torr H$_2$O and ~11 Torr TMA inside the chemical bottles. The dose times for TMA and H$_2$O were varied between 0.2 and 6 s with 40 s purges between reactant gases. However, the purge time was increased to 60 s for the 6 s doses. These purge times are significantly longer than purge times used during typical ALD experiments. Monitoring the reactor pressure during the ALD growth revealed that these were the minimum purge times required to return the reactor pressure back to the baseline pressure. During the Al$_2$O$_3$ ALD, the QCM period and reactor pressure were recorded at 100 ms intervals.

For each combination of TMA and H$_2$O dose times, 30 cycles were grown before switching to a different combination of dose times. Changes in the growth rates were observed to occur over the first 5–10 cycles of Al$_2$O$_3$ ALD growth for every combination of dose times. These changes are attributed to the coverage of surface sites from the previous 30 cycles of growth. The coverage of surface sites is dependent on the particular dose times. Only data recorded for the last 20 cycles of growth were considered to eliminate this complication.

3. Results and Analysis

A. Pressure Profiles. The total reactant exposure during each reactant dose was quantified using the recorded pressure profiles. The pressure profile during Al$_2$O$_3$ ALD consists of three separate components: N$_2$, Al(CH$_3$)$_3$ and H$_2$O reactants and CH$_4$ reaction products. The relative amounts of Al(CH$_3$)$_3$ and H$_2$O reactants

consumed and CH$_4$ reaction products generated are not known. Consequently, the pressure profiles during ALD growth cannot be used to quantify the reactant exposures. Instead, the Al(CH$_3$)$_3$ and H$_2$O reactant exposures were quantified by recording the pressures for Al(CH$_3$)$_3$ and H$_2$O individually after the surface reaction producing CH$_4$ reached completion. The pressure profiles were integrated to determine the total exposure in Torr-s after subtracting the N$_2$ background pressure.

Figure 2 shows the measured pressure profiles in the reactor at 125 °C for the individual Al(CH$_3$)$_3$ and H$_2$O reactants. To ensure that these pressure profiles were obtained after the surface reaction reached completion, these pressure profiles were recorded after dosing one of the reactants into the reactor multiple times, separated by a N$_2$ purge, without dosing the other reactant. Note that the N$_2$ base pressure was subtracted from each pressure profile. Figure 2a shows the pressure profiles during H$_2$O doses of 1, 2, 4, and 6 s separated by 40 s N$_2$ purges. The pressure rises to ~29 mTorr in 300 ms and then begins to fall at ~0.5 s for all the H$_2$O dose times. For the dose times of 2, 4, and 6 s, the H$_2$O pressure begins to rise again about 1 s after opening the valve.

For the dose time of 6 s, the H$_2$O pressure levels off ~5 s after opening the dose valve. For all the dose times, the pressure drops rapidly after the dose valve is closed and the purge valve is reopened. However, after the initial drop, the pressure rises slightly after the purge valve is opened before decaying to the zero level. This additional pressure rise is reduced for longer dose times. The pressure decays following the closing of the dose valves may result from slight changes in the effective pumping speed resulting from the H$_2$O exposures. In addition, some H$_2$O may slowly desorb from the surfaces of the reactor and prevent the pressure from reaching the zero level.

Similarly, Figure 2b shows the pressure profiles during TMA doses of 0.6, 1, 1.6, 2, 4, and 6 s separated by 40 s purges. The pressure rise during the TMA dose follows a curve that appears to be identical regardless of dose time. The TMA pressure rises during the entire TMA dose. The TMA pressure drops after the dose valve is closed. During the purge step, the TMA pressure rises slightly for about 2–3 s after the TMA valve is closed for the TMA doses of 0.6, 1, 1.6, and 2 s. For all the TMA doses, the pressure slowly decays to the zero level. This slow decay following the closing of the dose valves again may result from changes in the effective pumping speed resulting from the TMA exposures.
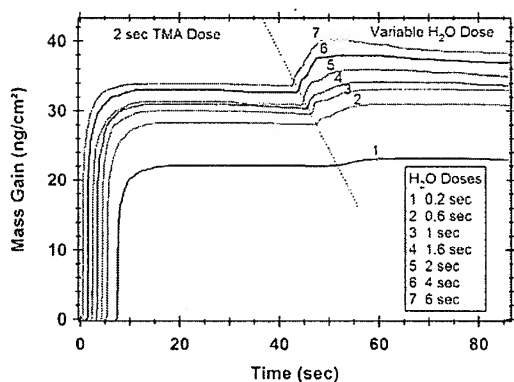
Figure 4. QCM mass gains for Al_2O_3 ALD at 125 °C with a 2 s TMA dose and variable H_2O doses. Each curve is the average of 20 different runs. From left to right the curves are laterally offset in order of decreasing H_2O dose time. The dotted line indicates the start of the H_2O dose.
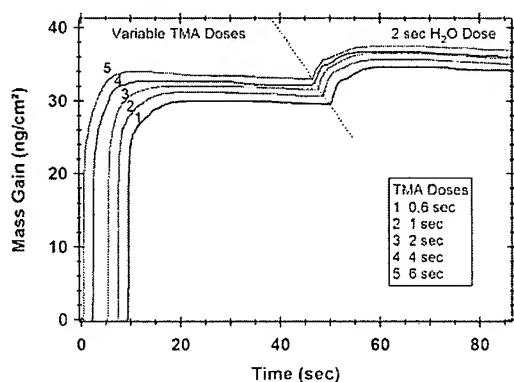

Figure 5. QCM mass gains for Al_2O_3 ALD at 125 °C with a 2 s H_2O dose and variable TMA doses. Each curve is the average of 20 different runs. From left to right, the curves are offset in order of decreasing TMA dose time. The dotted line indicates the start of the H_2O dose.

TMA exists in monomer–dimer equilibrium in the gas phase, and both the monomer and the dimer will be present in the reactor.[29-31] At equilibrium at 120.5 °C, the monomer–dimer equilibrium constant has been measured as $K_d = P_{m\text{-}TMA}^2/P_{d\text{-}TMA} = 1.32 \times 10^{-2}$ mol/L where m-TMA is the monomer and d-TMA is the dimer.[30] This equilibrium constant indicates that a significant fraction of the TMA is present as the dimer. Lower total TMA pressures will increase the relative fraction of monomer. At total TMA pressures of 1, 0.1, and 0.01 Torr at 120.5 °C, the pressure ratios of $P_{m\text{-}TMA}/P_{d\text{-}TMA}$ are approximately 0.11, 0.43, and 1.94, respectively. However, in viscous flow, the mass difference and interconversion between the monomer and dimer should not affect the travel time of TMA through the reactor.

B. Mass Gain versus Time for Variable H_2O and TMA Exposures. Figure 3 shows the mass gain and reactor pressure obtained during a single cycle of Al_2O_3 ALD. The dose times for TMA and H_2O were 2 s, indicated by the solid bars at the top of the graph. The reactant doses were separated by 40 s N_2 purges. The mass gains during the TMA and H_2O doses are indicated by ΔM_A and ΔM_B, respectively. The pressure from the reactants and products obtained after subtracting the N_2 background pressure of ~1 Torr is also shown in Figure 3. Close examination of the pressure profile reveals that the purge time of 40 s is the minimum time required for the pressure to return back to the zero level. Much longer purge times are required for low temperature Al_2O_3 ALD than are typical at higher temperatures.[7]
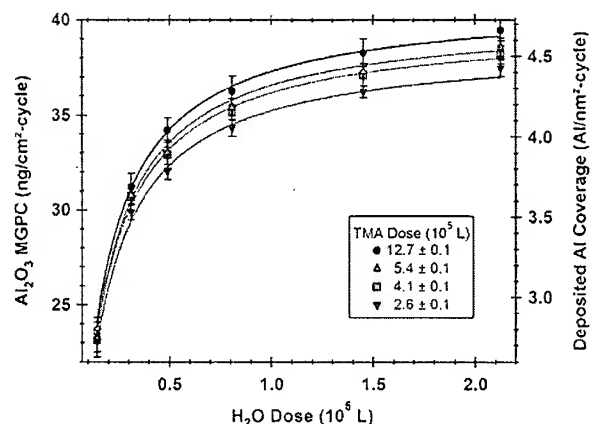

Figure 6. Al_2O_3 MGPC versus H_2O exposure for four different TMA exposures. Solid lines are from a global fit to the data using eq 12.

Typical mass gains obtained for Al_2O_3 ALD with variable H_2O and TMA dose times are shown in Figures 4 and 5, respectively. Each of the curves is the average of 20 ALD cycles. In Figure 4, the H_2O dose time was varied and the TMA dose time was held constant at 2 s. The curves are laterally offset from left to right in order of decreasing H_2O dose. The part of the curves to the left of the dotted line in Figure 4 corresponds to a 2 s TMA dose and a 40 s purge. The start of the H_2O dose is approximately indicated by the dotted line. Most of the H_2O doses are followed by a 40 s purge. However, the H_2O exposure of 6 s is followed by a 60 s purge.

Figure 4 reveals that Al_2O_3 ALD at 125 °C is not completely self-limiting at higher H_2O exposures. The mass gain during the H_2O dose increases for increasing H_2O dose time. In addition, the mass gain increases during the constant TMA doses after the increasing H_2O dose times. Earlier studies have measured Al_2O_3 ALD versus varying H_2O doses at higher temperatures than 125 °C.[32] Slightly larger Al_2O_3 ALD growth rates were observed for larger H_2O doses. This increase was explained in terms of a higher hydroxyl coverage on the Al_2O_3 ALD surface after the larger H_2O doses.[32]

Figure 4 also reveals the importance of sufficiently long purge times. As the H_2O dose times become longer, Figure 4 shows a slight mass loss after the H_2O exposure. This mass loss may result from the desorption of molecularly adsorbed H_2O on the hydroxylated Al_2O_3 surface or from recombinative desorption of hydroxyl species as expressed by the reverse of reaction B2 given by eq 3. The earlier larger growth rates for Al_2O_3 ALD at higher temperatures[32] could have resulted from either higher hydroxyl coverages or molecularly adsorbed H_2O after larger H_2O doses. The purge time after the H_2O dose will play a critical role in defining the time for desorption of molecularly adsorbed H_2O or dehydroxylation of hydroxyl coverage.

The H_2O dose time was constant while the TMA dose time was varied in Figure 5. The curves are again laterally offset from left to right in order of decreasing TMA dose times. The purge time after each reactant was 40 s. The TMA dose begins on the left of the figure; the start of the H_2O dose is indicated by the dotted line. The results show that Al_2O_3 ALD at 125° is not completely self-limiting at higher TMA exposures. For the largest TMA dose of 6 s, the mass gain reaches a maximum at the end of the TMA dose before dropping slightly during the TMA purge step. These results reiterate the importance of sufficiently long purge times. The mass gains were recorded only at the end of purge times to eliminate these transient effects.

The lack of complete self-limiting behavior for both the H_2O and TMA doses suggests that the low temperature of 125 °C
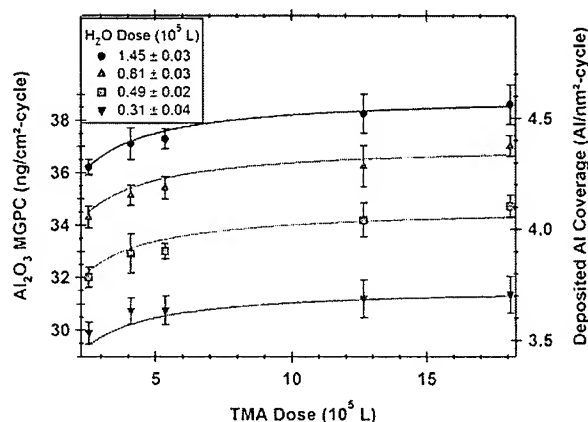
Figure 7. Al$_2$O$_3$ MGPC versus TMA exposure for four different H$_2$O exposures. Solid lines are from a global fit to the data using eq 12.

may be kinetically limiting the reactions. The slower reaction kinetics at lower temperature may require very long exposures for the reactions to reach completion. Consequently, in addition to higher hydroxyl coverages after higher H$_2$O exposures, another explanation for the lack of self-limiting behavior in Figures 4 and 5 is that extremely long H$_2$O and TMA exposure times are needed to reach saturation given the kinetic constraints on the surface reactions at 125 °C.

C. Mass Gains per Cycle versus H$_2$O and TMA Exposure. The MGPC during Al$_2$O$_3$ ALD was determined for each cycle by measuring the mass at the end of the H$_2$O purge and subtracting the mass prior to the TMA dose. Figure 6 displays the MGPC for Al$_2$O$_3$ ALD at four different TMA exposures as a function of the H$_2$O exposure. Similarly, Figure 7 shows the Al$_2$O$_3$ MGPC for four different H$_2$O exposures as a function of the TMA exposure. The H$_2$O and TMA exposures are plotted in Langmuirs (10^6 L = 1 Torr-s). The left-hand axis shows the MGPC. The right-hand axis indicates the number of aluminum atoms deposited per square nanometer per cycle (Al/nm^2-cycle). The deposited aluminum coverage was determined from the well-established stoichiometry of Al$_2$O$_3$ ALD.

Figure 6 displays that the Al$_2$O$_3$ MGPCs increase quickly with small H$_2$O doses. The Al$_2$O$_3$ MGPCs then increase more slowly versus H$_2$O dose before nearly reaching a limit at higher H$_2$O doses. The limiting Al$_2$O$_3$ MGPCs are only weakly dependent on the TMA doses. Figure 7 indicates that the Al$_2$O$_3$ MGPCs also increase very rapidly with small TMA doses. The Al$_2$O$_3$ MGPCs then reach limiting values that are dependent on the H$_2$O dose. The solid lines in Figures 6 and 7 are fits to the data using a single multivariate fitting function incorporating both the TMA and H$_2$O exposures. This fitting is described later in Section 4.

Rutherford backscattering has been used previously to determine that Al$_2$O$_3$ ALD films grown at 125 °C are stoichiometric Al$_2$O$_3$ with no carbon incorporation in the film.[7] However, forward recoil spectrometry revealed a hydrogen concentration of 11% for Al$_2$O$_3$ ALD films grown at 125 °C.[7] An FTIR spectroscopy study has also shown earlier that hydroxyl groups remain in the Al$_2$O$_3$ ALD film after a saturating TMA exposure.[3] The number of hydroxyl species increases with Al$_2$O$_3$ ALD film thickness. In addition, the hydroxyl groups do not undergo isotopic exchange with D$_2$O and can be eliminated from the film only after annealing above 1000 K.[3] These results indicate that hydroxyls are incorporated in the bulk of the Al$_2$O$_3$ ALD film.

Since no carbon is incorporated during Al$_2$O$_3$ ALD, the Al$_2$O$_3$ MGPCs shown in Figures 6 and 7 can result from only three
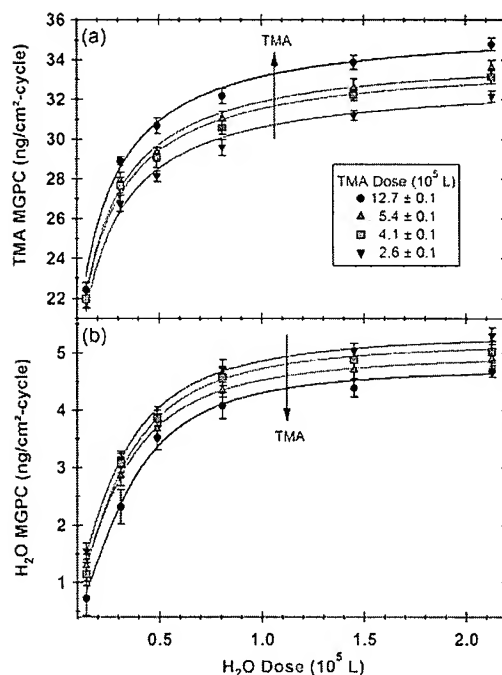

Figure 8. (a) TMA MGPC and (b) H$_2$O MGPC versus H$_2$O dose for four different TMA doses. Solid lines are only intended to guide the eye.
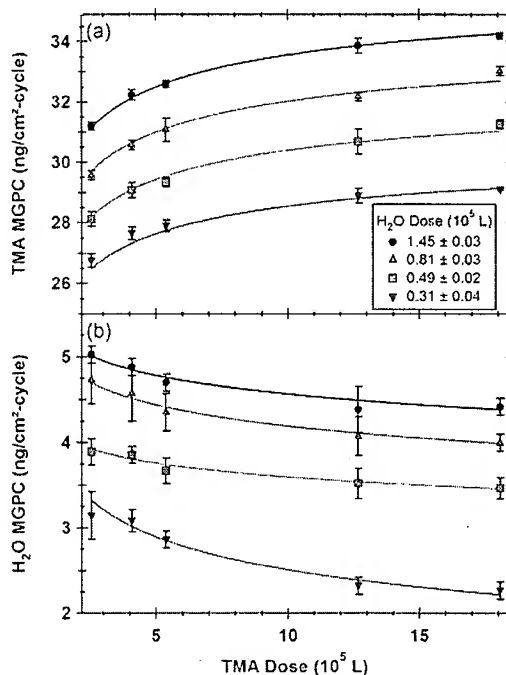

Figure 9. (a) TMA MGPC and (b) H$_2$O MGPC versus TMA dose for four different H$_2$O doses. Solid lines are only intended to guide the eye.

atomic species: aluminum, oxygen, and hydrogen. The aluminum coverage deposited per cycle, N_{Al}, can be determined from the measured Al$_2$O$_3$ MGPC using

$$N_{Al} = \frac{\Delta M_{Total} \cdot N_A}{\left(m_{Al} + \frac{3}{2} m_O + h \cdot m_H \right)} \quad (5)$$
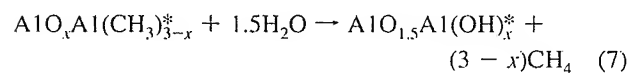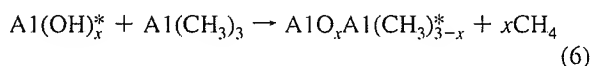
ΔM_{Total} is the measured MGPC, N_A is Avogadro's number, and m_{Al}, m_O, and m_H are the aluminum, oxygen, and hydrogen molar masses, respectively. h is the fraction of hydrogen included as hydroxyl species in the growing film. The calculated value of N_{Al} is very insensitive to hydrogen incorporation into the film. Assuming the film contained 11% hydrogen decreases the calculated value of N_{Al} by only 0.22%. Because of this insensitivity, all calculations of N_{Al} were made assuming $h = 0$. As shown in Figure 6, N_{Al} ranged from 2.7 to 4.7 Al/nm²-cycle versus H_2O dose. These N_{Al} values are in good agreement with other experiments that have measured deposited aluminum coverage per cycle of ~4−5 Al/nm²-cycle at higher temperatures after saturation H_2O doses.[11]

The effects of the H_2O and TMA exposures on the mass gains during each surface reaction were also determined by examining ΔM_A and ΔM_B. Figures 8 and 9 display the MGPCs during the TMA and H_2O doses, respectively, during one Al_2O_3 ALD cycle. The lines in these figures are meant only to guide the eye. Figure 8a and b reveal that the TMA and H_2O MGPCs increase as the H_2O dose increases. Figure 9a shows that the TMA MGPC also increases with increasing TMA exposure. In contrast, Figure 9b shows that the H_2O MGPC decreases with increasing TMA exposure. This complex behavior is caused by the interactions between the TMA and H_2O reactions.

The decrease of H_2O MGPC versus TMA dose in Figure 9b may be caused by more dehydroxylation from the surface at higher hydroxyl coverages. The methyl coverages increase versus TMA dose. These higher methyl coverages would then lead to high initial hydroxyl coverages according to reaction B1 given by eq 2. However, these higher initial hydroxyl coverages may not be stable at 125 °C and may recombine to desorb H_2O via $AlOH^* + AlOH^* \rightarrow Al-O-Al^* + H_2O$. This H_2O loss is also expressed by reaction B2 in eq 3 when $x > 1.5$. Because higher TMA doses produce higher methyl coverages that lead to higher hydroxyl coverages, the H_2O MGPC could decrease after higher TMA doses.

D. Hydroxyl and Methyl Coverages versus H_2O and TMA Exposures. The Al_2O_3 ALD surface chemistry is described by reactions A, B1, and B2 in eqs 1−3. However, these reactions can be simplified to just two reaction equations using the known characteristics for Al_2O_3 ALD. First, because the Al/O ratio of the bulk alumina film equals 2:3, 1.5 oxygen atoms must be incorporated per Al surface site. Since water is the only oxygen source in the reactor, 1.5 H_2O molecules must react with each aluminum site. Second, mass spectrometry experiments have shown that CH_4 is the only reaction product.[8] Likewise, Rutherford backscattering experiments have shown there is no carbon incorporation in the Al_2O_3 ALD film.[7] Consequently, all methyl groups remaining on the surface after the TMA dose must react to form CH_4 during the water dose.

Using these characteristics for Al_2O_3 ALD, the mechanism shown in reactions A, B1, and B2 in eqs 1−3 can be simplified to the following two reactions:[12,15]

$$Al(OH)_x^* + Al(CH_3)_3 \rightarrow AlO_xAl(CH_3)_{3-x}^* + xCH_4 \tag{6}$$

$$AlO_xAl(CH_3)_{3-x}^* + 1.5H_2O \rightarrow AlO_{1.5}Al(OH)_x^* + (3 - x)CH_4 \tag{7}$$

In these reactions, hydrogen atoms from H_2O remove the methyl groups from $Al(CH_3)_{3-x}^*$ as CH_4. The remaining hydrogen atoms from H_2O produce $Al(OH)_x^*$ species. Equations 6 and 7 cannot

Figure 10. (a) CH_3^* coverage after TMA dose and (b) OH* coverage after H_2O dose versus H_2O dose for four different TMA doses. The lines fit to the CH_3^* coverages in panel a are from eq 10. The line fit to the OH* coverage in panel b is from eq 11.
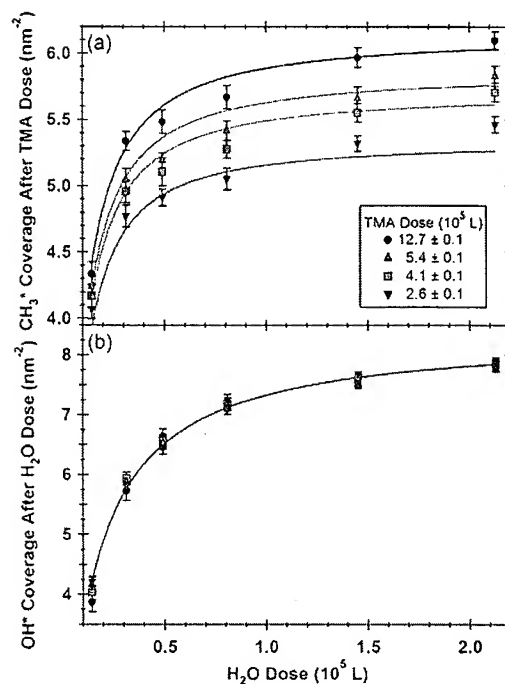

Figure 11. (a) CH_3^* coverage after TMA dose and (b) OH* coverage after H_2O dose versus TMA dose for four different H_2O doses. The lines fit to the CH_3^* coverages in panel a are from eq 10. The line fit to the OH* coverage in panel b is from eq 11.
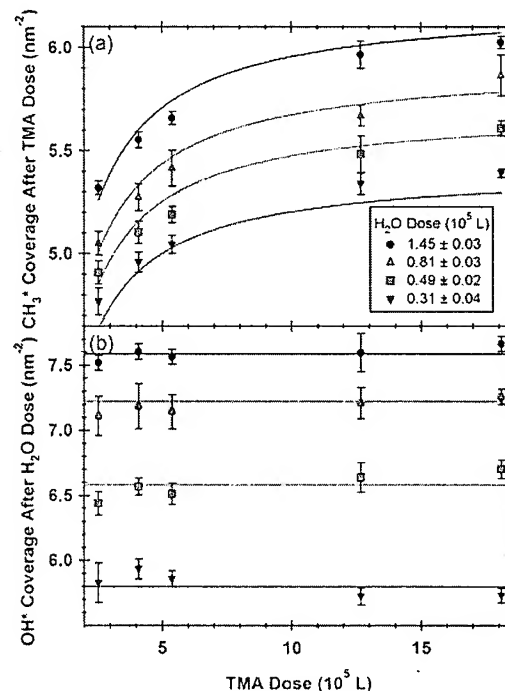
describe hydrogen incorporation in the Al_2O_3 ALD film. However, neglecting the hydrogen incorporation is only a minor error for the mass changes during Al_2O_3 ALD.

The MGPC for the TMA reaction, ΔM_A, described by eq 6 is

$$\Delta M_A = N_{Al}(m_{TMA} - x \cdot m_{CH_4}) \qquad (8)$$

where N_{Al} is the deposited aluminum coverage per cycle and m_{TMA} and m_{CH_4} are the molar masses of TMA and CH$_4$, respectively. x is the number of hydroxyls that react per Al atom deposited on the surface. By combining eqs 5 and 8 with $h = 0$, the coverage of hydroxyl species, N_{OH}, after the H$_2$O reaction is given by

$$N_{OH} = N_{Al} \cdot x = \frac{N_{Al} \cdot m_{TMA}}{m_{CH_4}} - \frac{\Delta M_A}{m_{CH_4}} \qquad (9)$$

Similarly, the coverage of methyl species, N_{CH_3}, after the TMA reaction described by eq 6 is given by

$$N_{CH_3} = 3N_{Al} - N_{OH} \qquad (10)$$

Figure 10 displays the CH$_3^*$ and OH* coverages after the TMA and H$_2$O reactions, respectively, as a function of the H$_2$O exposure for various TMA doses. Figure 11 shows the CH$_3^*$ and OH* coverages after the TMA and H$_2$O reactions, respectively, as a function of the TMA exposure for various H$_2$O doses. The CH$_3^*$ coverage after the TMA dose shown in Figures 10a and 11a is clearly dependent on both the TMA and H$_2$O exposures. The lines are fits to the methyl coverage. The OH* coverages after the H$_2$O dose for the four different TMA exposures shown in Figure 10b are all nearly identical. The OH* coverage after the H$_2$O dose increases with increasing H$_2$O exposure. Figure 11b shows that the OH* coverage after the H$_2$O dose is constant with respect to the TMA dose. The straight lines indicate the average hydroxyl coverage for each of the four different H$_2$O exposures.

4. Fitting Using Modified Langmuir Adsorption Isotherm Expressions

A. Hydroxyl Coverage. The dependence of the Al$_2$O$_3$ ALD growth rate on the hydroxyl coverage at temperatures higher than 125 °C was discussed in a recent review paper.[11] At growth temperatures of 150−250 °C, the deposited aluminum per cycle was found to depend linearly on the surface hydroxyl coverage. Similarly, the methyl coverage after the TMA reaction was also found to depend linearly on the hydroxyl coverage. Because of the importance of the hydroxyl coverage, analysis of Al$_2$O$_3$ ALD at 125 °C will first discuss the dependence of the hydroxyl coverage on the reactant exposures. The hydroxyl coverage on the surface was determined assuming that eqs 6 and 7 accurately describe the Al$_2$O$_3$ ALD process.

Figure 10b indicates that the hydroxyl coverage on the surface after the H$_2$O dose depends only on the H$_2$O exposure. Figure 11b shows that the hydroxyl coverage is constant with respect to the TMA dose. However, Figure 7 reveals that the deposited aluminum coverage per cycle does depend slightly on the TMA dose. Therefore, the hydroxyl coverage after the H$_2$O dose apparently does not depend on the deposited aluminum coverage per cycle. Figure 11a and b reveals that the OH* coverage does not depend on the CH$_3^*$ coverage. Since the hydroxyl coverage after the H$_2$O dose is independent of the surface produced by the TMA dose, the hydroxyl coverage can be calculated using only the H$_2$O exposure.

The data in Figure 10b for the OH* coverage after the H$_2$O dose were fit using a modified Langmuir adsorption isotherm
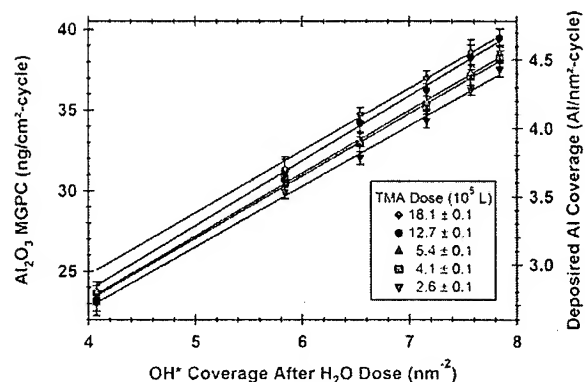

Figure 12. Al$_2$O$_3$ MGPC versus OH* coverage after H$_2$O dose for five different TMA doses. OH* coverages are calculated from eq 9. The solid lines are linear fits using a single y-intercept and different slopes.

expression. The Langmuir adsorption isotherm is applied to the equilibrium of surface coverage and adsorbate pressure assuming that each adsorbate occupies a single surface site.[33] In these ALD experiments, the adsorbate reacts with the surface, the pressure was not constant, and there is no equilibrium. However, the form of the Langmuir adsorption isotherm expression can still be used to fit the hydroxyl coverage versus H$_2$O exposure. Exposure replaces pressure in this modified Langmuir adsorption isotherm expression:[33]

$$S = \frac{S_0}{\left(1 + \dfrac{L^*}{L_{H_2O}}\right)} \qquad (11)$$

In this equation, S is the measured hydroxyl coverage, L_{H_2O} is the H$_2$O exposure in Langmuirs, and S_0 is the hydroxyl surface coverage corresponding to the saturation coverage.

In the standard Langmuir adsorption isotherm equation, $L^* = 1/K_{eq}$ where K_{eq} is the equilibrium constant $K_{eq} = k_a/k_d$ where k_a and k_d are the adsorption and desorption rate constants. In the modified Langmuir adsorption isotherm expression, L^* can be viewed as the H$_2$O exposure that yields $S = S_0/2$; that is, one-half of the complete hydroxyl coverage, S_0. The hydroxyl coverage grows progressively with H$_2$O exposures before reaching a saturation coverage after long H$_2$O exposures. The fit using eq 11 is shown by the solid line in Figure 10b.

This excellent fit suggests that H$_2$O reactive adsorption occurs with a probability that is dependent on the availability of unreacted AlCH$_3^*$ surface sites. For Langmuir adsorption, the adsorption probability is expressed as $(1 - \Theta)$, where Θ is the coverage of reacted AlOH* surface sites. Θ is a normalized coverage, and complete coverage is $\Theta = 1$. The H$_2$O reactive adsorption versus H$_2$O exposure mirrors the adsorption/desorption equilibrium during Langmuir adsorption versus adsorbate pressure.

From the fit, the maximum absolute hydroxyl surface coverage at 125 °C is $S_0 = 8.37 \pm 0.09$ nm^{-2}, and the H$_2$O exposure required to achieve 50% hydroxyl coverage half-exposure is $L^* = 1.41 \pm 0.04 \times 10^4$ L. In comparison, the full monolayer hydroxyl coverage on alumina powders at 100 °C is ~12.5 nm^{-2}.[34−36] The hydroxyl coverage on alumina powders after annealing at 200 °C is ~9 nm^{-2}.[34] The maximum hydroxyl coverage of $S_0 = 8.37 \pm 0.09$ nm^{-2} at 125 °C is in reasonable agreement with the previously measured hydroxyl coverages on alumina powders. The slightly larger hydroxyl coverages

on the alumina powders may be attributed to the differences between the planar and powder samples.

B. Al$_2$O$_3$ Mass Gain Per Cycle. Previous investigations at temperatures higher than 125 °C have shown that the number of aluminum atoms deposited during the TMA dose increases linearly with the hydroxyl coverage.[11,37] For Al$_2$O$_3$ ALD at 125 °C, a plot of the Al$_2$O$_3$ MGPC versus the hydroxyl coverage after the H$_2$O dose is shown in Figure 12. The deposited Al coverage per cycle is shown on the right axis. The symbols are the measured data using five different TMA doses. The Al$_2$O$_3$ MGPC increases very linearly with the OH* coverage. The solid lines are linear fits to data using a constant y-intercept and variable slopes.

The y-intercept defines the deposited aluminum coverage per cycle on a completely dehydroxylated Al$_2$O$_3$ surface. From the fits in Figure 12, the deposited aluminum coverage per cycle for the dehydroxylated surface equals 0.91 ± 0.07 nm^{-2}. The slope increases slightly with increasing TMA exposure. The slope (Al$_2$O$_3$ MGPC)/(OH* coverage) increases from 0.44 ± 0.01 at a TMA dose of 2.6×10^5 L to 0.48 ± 0.01 at a TMA dose of 12.7×10^5 L.

Previous measurements of complete TMA adsorption have been performed on powdered alumina and silica with different initial hydroxyl densities.[11,37] The deposited Al coverage per cycle versus OH* coverage was linear with a y-intercept of 1.68 ± 0.09 nm^{-2} and a slope of 0.37 ± 0.02.[11,37] These previous reports for the slope are in good agreement with our measured slopes of $0.44-0.48$. The different y-intercepts may reflect the difference between the planar substrates used in the current experiments and the porous substrates utilized in the earlier measurements.

The Al$_2$O$_3$ MGPC is a linear function of the hydroxyl coverage. The hydroxyl coverage depends on the H$_2$O exposure according to the modified Langmuir adsorption isotherm expression given in eq 11. A similar form for ΔM_{Total} can be constructed on the basis of contributions from H$_2$O and TMA exposures. A trial function for ΔM_{Total} versus H$_2$O and TMA exposures is

$$\Delta M_{Total} = \frac{M_{max}}{\left(1 + \dfrac{L^*_{H_2O}}{L_{H_2O}}\right) \cdot \left(1 + \dfrac{L^*_{TMA}}{L_{TMA}}\right)} \quad (12)$$

where L_{H_2O} and L_{TMA} are the H$_2$O and TMA exposures in Langmuirs, respectively. M_{Max} is the maximum mass gain. Similar to L^* in eq 11, $L^*_{H_2O}$ and L^*_{TMA} can be viewed as the H$_2$O and TMA "half exposures". When the H$_2$O and TMA exposures are equal to their respective "half-exposures", the total mass gain corresponds to 25% of the maximum mass gain.

All the data shown in Figures 6 and 7 were fit using eq 12 to determine the values of the M_{Max}, $L^*_{H_2O}$ and L^*_{TMA}. The fit using eq 12 to the data in Figures 6 and 7 is quite good. The average difference between the measured and calculated values is ~1%. From this fit, $M_{Max} = 41.6 \pm 0.3$ ng/cm^2-cycle. The maximum mass gain corresponds to a deposited Al coverage per cycle of 4.91 ± 0.03 nm^{-2} cycle^{-1}. Previous experiments measured a maximum Al$_2$O$_3$ growth rate at 125 °C equal to 39 ng/cm^2-cycle.[7] This previous measurement is in good agreement with $M_{Max} = 41.6 \pm 0.3$ ng/cm^2-cycle. The half-exposures for H$_2$O and TMA are $L^*_{H_2O} = 9.8 \pm 0.3 \times 10^3$ L and $L^*_{TMA} = 1.9 \pm 0.2 \times 10^4$ L, respectively.

This fit of the modified Langmuir adsorption isotherm expression to the data in Figures 6 and 7 suggests that H$_2$O and TMA reactive adsorption occurs with probabilities that are dependent on the availability of unreacted AlCH$_3^*$ and AlOH* sites, respectively. The fits again argue that the reactive adsorption probabilities are proportional to $(1 - \Theta)$, where Θ is the coverage of either reacted AlCH$_3^*$ sites during H$_2$O adsorption or reacted AlOH* sites during TMA adsorption.

5. Conclusions

QCM measurements were used to examine Al$_2$O$_3$ ALD growth using TMA and H$_2$O at 125 °C. The Al$_2$O$_3$ ALD MGPCs were measured versus TMA and H$_2$O exposures. The MGPCs for the individual TMA and H$_2$O reactions were also measured versus TMA and H$_2$O exposures. The Al$_2$O$_3$ MGPC increased with increasing H$_2$O exposures at a fixed TMA exposure. The Al$_2$O$_3$ MGPC also increased with increasing TMA exposure at a fixed H$_2$O exposure. The QCM studies revealed that neither the TMA nor the H$_2$O reactions were completely self-limiting. This behavior may be attributed to the slower reaction kinetics for the TMA and H$_2$O surface at lower temperature.

The Al$_2$O$_3$ MGPCs increased rapidly after small H$_2$O doses and slowly reached a limiting value that was not very dependent on the TMA dose. The Al$_2$O$_3$ MGPCs also increased rapidly after small TMA doses and different limiting values were obtained for different H$_2$O doses. The TMA MGPCs increased for higher TMA exposures for all H$_2$O exposures. On the other hand, the H$_2$O MGPC decreased for higher TMA exposures at all H$_2$O exposures. More dehydroxylation at higher hydroxyl coverages may explain this decrease. The higher hydroxyl coverages after H$_2$O exposures result from higher methyl coverages after higher TMA exposures. The hydroxyl coverage after the H$_2$O exposure was dependent only on the H$_2$O exposure. The Al$_2$O$_3$ MGPC was linearly dependent on the hydroxyl coverage after the H$_2$O dose.

The hydroxyl coverage versus the H$_2$O exposures and the Al$_2$O$_3$ MGPC versus the H$_2$O and TMA exposures were fit using modified Langmuir adsorption isotherm expressions. These fits suggest that reactant adsorption during the H$_2$O and TMA exposures occurs with a probability that is dependent on $(1 - \Theta)$, where Θ is the coverage of reacted surface sites. These results should be useful for understanding and modeling low temperature Al$_2$O$_3$ ALD. Many applications result from low temperature Al$_2$O$_3$ ALD on organic, polymeric, and biological substrates.

References and Notes

(1) George, S. M.; Ott, A. W.; Klaus, J. W. *J. Phys. Chem.* **1996**, *100*, 13121.
(2) Suntola, T. *Thin Solid Films* **1992**, *216*, 84.
(3) Dillon, A. C.; Ott, A. W.; Way, J. D.; George, S. M. *Surf. Sci.* **1995**, *322*, 230.
(4) Ferguson, J. D.; Weimer, A. W.; George, S. M. *Thin Solid Films* **2000**, *371*, 95.
(5) Ferguson, J. D.; Weimer, A. W.; George, S. M. *Chem. Mater.* **2004**, *16*, 5602.
(6) Groner, M. D.; Elam, J. W.; Fabreguette, F. H.; George, S. M. *Thin Solid Films* **2002**, *413*, 186.
(7) Groner, M. D.; Fabreguette, F. H.; Elam, J. W.; George, S. M. *Chem. Mater.* **2004**, *16*, 639.

Al$_2$O$_3$ Atomic Layer Deposition

J. Phys. Chem. A, Vol. 114, No. 3, 2010 **1289**

(8) Juppo, M.; Rahtu, A.; Ritala, M.; Leskelä, M. *Langmuir* **2000**, *16*, 4034.

(9) Ott, A. W.; Klaus, J. W.; Johnson, J. M.; George, S. M. *Thin Solid Films* **1997**, *292*, 135.

(10) Ott, A. W.; McCarley, K. C.; Klaus, J. W.; Way, J. D.; George, S. M. *Appl. Surf. Sci.* **1996**, *107*, 128.

(11) Puurunen, R. L. *J. Appl. Phys.* **2005**, *97*.

(12) Rahtu, A.; Alaranta, T.; Ritala, M. *Langmuir* **2001**, *17*, 6506.

(13) Higashi, G. S.; Fleming, C. G. *Appl. Phys. Lett.* **1989**, *55*, 1963.

(14) Soto, C.; Tysoe, W. T. *J. Vac. Sci. Technol., A* **1991**, *9*, 2686.

(15) Wind, R. A.; Fabreguette, F. H.; Sechrist, Z. A.; George, S. M. *J. Appl. Phys.* **2009**, *105*, 074309.

(16) Elam, J. W.; Groner, M. D.; George, S. M. *Rev. Sci. Instrum.* **2002**, *73*, 2981.

(17) Mayer, T. M.; Elam, J. W.; George, S. M.; Kotula, P. G.; Goeke, R. S. *Appl. Phys. Lett.* **2003**, *82*, 2883.

(18) Ritala, M.; Leskela, M.; Dekker, J. P.; Mutsaers, C.; Soininen, P. J.; Skarp, J. *Chem. Vap. Deposition* **1999**, *5*, 7.

(19) Wilson, C. A.; Grubbs, R. K.; George, S. M. *Chem. Mater.* **2005**, *17*, 5625.

(20) *HSC Chemistry 5.1*; Outokumpu Research Oy: Pori, Finland.

(21) Knez, M.; Kadri, A.; Wege, C.; Gosele, U.; Jeske, H.; Nielsch, K. *Nano Lett.* **2006**, *6*, 1172.

(22) Lee, S. M.; Pippel, E.; Gosele, U.; Dresbach, C.; Qin, Y.; Chandran, C. V.; Brauniger, T.; Hause, G.; Knez, M. *Science* **2009**, *324*, 488.

(23) Carcia, P. F.; McLean, R. S.; Reilly, M. H.; Groner, M. D.; George, S. M. *Appl. Phys. Lett.* **2006**, *89*, 031915.

(24) Dameron, A. A.; Davidson, S. D.; Burton, B. B.; Carcia, P. F.; McLean, R. S.; George, S. M. *J. Phys. Chem. C* **2008**, *112*, 4573.

(25) Groner, M. D.; George, S. M.; McLean, R. S.; Carcia, P. F. *Appl. Phys. Lett.* **2006**, *88*, 051907.

(26) Rocklein, M. N.; George, S. M. *Anal. Chem.* **2003**, *75*, 4975.

(27) Theory of Operation. In *Maxtek TM-350/400 Operation and Service Manual for Model TM-350/400 Maxtek Thickness Monitor*, 10th ed.; Maxtek, Inc.: Santa Fe Springs, California, 2004.

(28) Benes. E. *J. Appl. Phys.* **1984**, *56*, 608.

(29) Hay, J. N.; Hooper, P. G.; Robb, J. C. *J. Organomet. Chem.* **1971**, *28*, 193.

(30) Henricks, Ch.; Eyman, D. P. *Inorg. Chem.* **1967**, *6*, 1461.

(31) Laubengayer, L. W.; Gilliam, W. F. *J. Am. Chem. Soc.* **1941**, *63*, 477.

(32) Matero, R.; Rahtu, A.; Ritala, M.; Leskela, M.; Sajavaara, T. *Thin Solid Films* **2000**, *368*, 1.

(33) Masel, R. I. *Principles of Adsorption and Reaction on Solid Surfaces*, 1st ed.; John Wiley & Sons, Inc.: New York, 1996.

(34) Knozinger, H.; Ratnasamy, P. *Catal. Rev. Sci. Eng.* **1978**, *17*, 31.

(35) Peri, J. B. *J. Phys. Chem.* **1965**, *69*, 211.

(36) Peri, J. B. *J. Phys. Chem.* **1965**, *69*, 220.

(37) Puurunen, R. L. *Appl. Surf. Sci.* **2005**, *245*, 6.